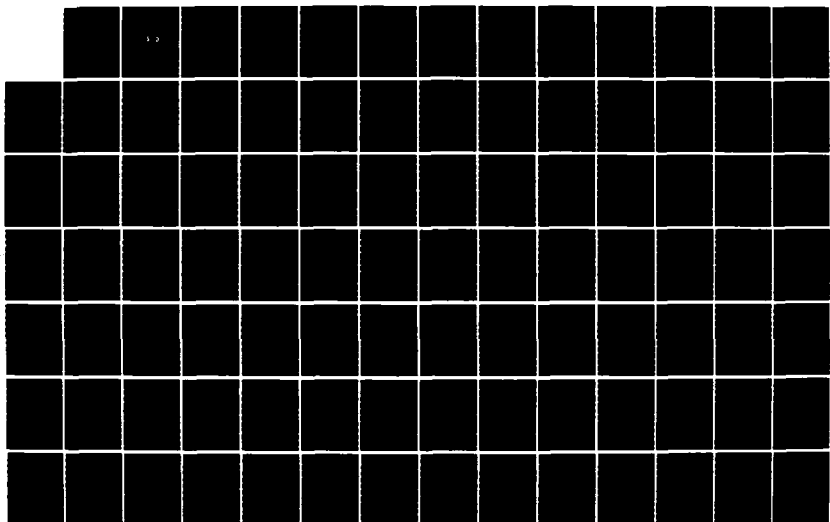


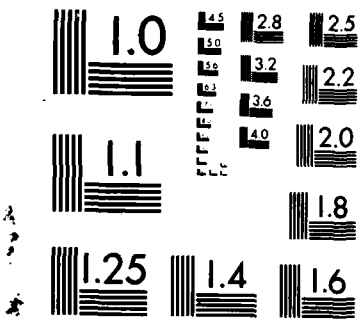
RD-A174 883 INVERSION FOR SOURCE PARAMETERS OF UNDERGROUND NUCLEAR 1/2
EXPLOSIONS WITH IM. (U) WOODWARD-CLYDE CONSULTANTS
PASADENA CA J S BARKER ET AL. 15 MAR 86 WCCP-R-86-81

UNCLASSIFIED AFGL-TR-86-0142 F19628-85-C-0036

F/G 8/11

NL





MICROCOPY RESOLUTION TEST CHART
NATIONAL BUREAU OF STANDARDS-1963-A

AD-A174 003

AFGL-TR-86-0142

(2)

Inversion for Source Parameters of Underground Nuclear Explosions
with Implications for Yield Estimation

by Jeffrey S. Barker, Roy W. Burger, L. J. Burdick and Thorne Lay

Woodward-Clyde Consultants
566 El Dorado St.
Pasadena, CA 91101

DTIC
SELECTED
NOV 06 1986
S D
D

15 March 1986

Scientific Report No. 2

Approved for Public Release; Distribution Unlimited

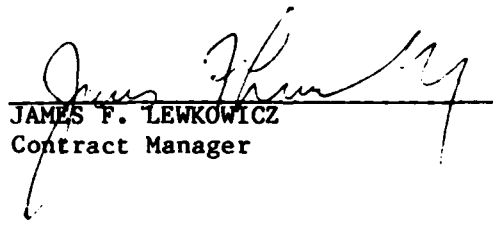
FILE COPY
JMC

Air Force Geophysics Laboratory
Air Force Systems Command
United States Air Force
Hanscom Air Force Base, Massachusetts 01731

86 11 3 050

CONTRACTOR REPORTS

This technical report has been reviewed and is approved for publication.


JAMES F. LEWKOWICZ
Contract Manager


HENRY A. OSSING
Chief, Solid Earth Geophysics Branch

FOR THE COMMANDER


DONALD H. ECKHARDT
Director
Earth Sciences Division

This report has been reviewed by the ESD Public Affairs Office (PA) and is releasable to the National Technical Information Service (NTIS).

Qualified requesters may obtain additional copies from the Defense Technical Information Center. All others should apply to the National Technical Information Service.

If your address has changed, or if you wish to be removed from the mailing list, or if the addressee is no longer employed by your organization, please notify AFGL/DAA, Hanscom AFB, MA 01731-5000. This will assist us in maintaining a current mailing list.

Unclassified

SECURITY CLASSIFICATION OF THIS PAGE

AD-A174 603

REPORT DOCUMENTATION PAGE

1a. REPORT SECURITY CLASSIFICATION <u>Unclassified</u>		1b. RESTRICTIVE MARKINGS			
2a. SECURITY CLASSIFICATION AUTHORITY		3. DISTRIBUTION/AVAILABILITY OF REPORT Approved for public release; distribution unlimited.			
2b. DECLASSIFICATION/DOWNGRADING SCHEDULE					
4. PERFORMING ORGANIZATION REPORT NUMBER(S) WCCP-R-86-01		5. MONITORING ORGANIZATION REPORT NUMBER(S) AFGL-TR-86-0142			
6a. NAME OF PERFORMING ORGANIZATION Woodward-Clyde Consultants	6b. OFFICE SYMBOL (If applicable)	7a. NAME OF MONITORING ORGANIZATION Air Force Geophysics Laboratory			
6c. ADDRESS (City, State and ZIP Code) 566 El Dorado St., Suite 100 Pasadena, CA 91101		7b. ADDRESS (City, State and ZIP Code) Hanscom Air Force Base Massachusetts 01731-5000			
8a. NAME OF FUNDING/SPONSORING ORGANIZATION DARPA	8b. OFFICE SYMBOL (If applicable)	9. PROCUREMENT INSTRUMENT IDENTIFICATION NUMBER F19628-85-C-0036			
8c. ADDRESS (City, State and ZIP Code) 1400 Wilson Blvd. Arlington, VA 22209		10. SOURCE OF FUNDING NOS.			
11. TITLE (Include Security Classification) see block 16 - unclassified		PROGRAM ELEMENT NO. 62714E	PROJECT NO. 5A10	TASK NO. DA	WORK UNIT NO. AV
12. PERSONAL AUTHOR(S) Jeffrey S. Barker, Roy W. Burger, L. J. Burdick and Thorne Lay					
13a. TYPE OF REPORT Scientific Report #2	13b. TIME COVERED FROM 9/5/85 TO 3/5/86	14. DATE OF REPORT (Yr., Mo., Day) 15 March 1986		15. PAGE COUNT 130	
16. SUPPLEMENTARY NOTATION Inversion for Source Parameters of Underground Nuclear Explosions with Implications for Yield Estimation <i>(The first part of this report presents</i>					
17. COSATI CODES		18. SUBJECT TERMS (Continue on reverse if necessary and identify by block number) Inversion of explosion seismic waveforms, near-field observations, effective source functions, velocity gradients, teleseismic attenuation, frequency-dependent Q			
19. ABSTRACT (Continue on reverse if necessary and identify by block number) This report consists of two parts. In the first part, we present a method for the simultaneous inversion of near-field explosion waveforms for parameters of the source and structure. The inversion automatically provides information on the tradeoffs between parameters and error analyses of the resultant models. The source may be parameterized by any of several effective source functions. The structure is parameterized as a layered stack of gradients defined by the velocity at the top of the layer, the velocity gradient within the layer and the depth to the top of the layer. The gradient model is then discretized into homogeneous plane layers, with the layer thickness defined as the wavelength of the predominant period in the data, and synthetics are computed using asymptotic generalized ray theory. For each observed waveform, the residuals consist of the normalized cross-correlation coefficient between the data and synthetics (a measure of waveform fit), the difference in normalization factors (a measure of absolute amplitude), and the time lag to the peak of cross-correlation (a measure of absolute travel time).					
20. DISTRIBUTION/AVAILABILITY OF ABSTRACT UNCLASSIFIED/UNLIMITED <input type="checkbox"/> SAME AS RPT <input type="checkbox"/> DTIC USERS <input type="checkbox"/>			21. ABSTRACT SECURITY CLASSIFICATION Unclassified		
22a. NAME OF RESPONSIBLE INDIVIDUAL James Lewkowicz			22b. TELEPHONE NUMBER (Include Area Code) (617) 377-3028	22c. OFFICE SYMBOL AFGL/LWH	

2

Unclassified

SECURITY CLASSIFICATION OF THIS PAGE

Numerical partial derivatives are computed and the problem is solved using an iterative generalized inverse. Four test inversions of synthetic data sets are presented. These illustrate the need to truncate eigenvalues and preferentially weight the parameters and residuals in order to stabilize the inversion. Preliminary results are presented for the Pahute Mesa events BOXCAR, INLET, MAST and SCOTCH, in which the structure model is constrained to two gradients separated by a second-order discontinuity. The source models obtained have higher estimates of Ψ_∞ than those of Barker, et al. (1985), although the adequacy of the structure models is somewhat suspect.

The second part of the report addresses the implications of choosing a particular representation of the RDP on the determination of teleseismic attenuation. This time-domain analysis is based on a near-field to far-field amplitude comparison. The near-field amplitude information is contained in the parameters of the explosion source model assuming either the Mueller-Murphy or Helmberger-Hadley representations. The teleseismic amplitude information is from a large set of WWSSN short-period recordings. Using only these narrow band time-domain data, the various combinations of source models with frequency-independent and frequency-dependent Q models are indistinguishable. However, utilizing spectral shape information in the 0.5 to 4 Hz band as a constraint at higher frequencies, either source representation, when convolved with a frequency-dependent Q model, is consistent with the data. The value of t^* near 1 Hz is about 1.0 sec for the Mueller-Murphy source or 0.8 sec for the Helmberger-Hadley source. Adopting an average attenuation model, predicted amplitudes and yields are shown to be within the uncertainty of the data for all of the events analyzed.

Unclassified

SECURITY CLASSIFICATION OF THIS PAGE

TABLE OF CONTENTS

	<u>Page</u>
PREFACE	v
 <u>PART I - SIMULTANEOUS INVERSION OF NEAR-FIELD DATA FOR EXPLOSION SOURCE AND STRUCTURE PARAMETERS</u>	
ABSTRACT	I-2
INTRODUCTION	I-4
BACKGROUND	I-5
INVERSION METHOD	I-9
TESTS OF THE WAVEFORM INVERSION PROCEDURE	I-18
Test # 1 - Halfspace Velocity	I-18
Test # 2 - A Single Gradient	I-22
Test # 3 - Velocity and Gradient	I-28
Test # 4 - Source and Structure	I-35
INVERSIONS FOR PAHUTE MESA EVENTS	I-45
BOXCAR	I-45
INLET	I-53
MAST	I-59
SCOTCH	I-65
SUMMARY AND CONCLUSIONS	I-71
REFERENCES	I-75

Distribution Statement A is correct for this report. It has been cleared by the Public Affairs Office of AFGL.
Per Ms. Diane Corazzini, AFGL/SULR



Accesion For	
NTIS	CRA&I <input checked="" type="checkbox"/>
DTIC	TAB <input type="checkbox"/>
Unannounced <input type="checkbox"/>	
Justification	
By	
Distribution /	
Availability Codes	
Dist	Avail a.d/or Special
A1	

TABLE OF CONTENTS (cont'd)

	<u>Page</u>
PART II - AVERAGE Q AND YIELD ESTIMATES FROM THE PAHUTE MESA TEST SITE	
ABSTRACT	II-2
INTRODUCTION	II-3
MODELING APPROACH	II-6
Observations	II-7
Attenuation Models	II-9
Source Models	II-10
RESULTS	II-15
Time-Domain Amplitudes	II-15
Spectral Shape Constraints	II-24
YIELD ESTIMATION	II-30
DISCUSSION	II-33
CONCLUSIONS	II-43
REFERENCES	II-44

PREFACE

This report includes the results of two studies with implications for yield estimation of underground nuclear explosions. In the first part, we develop a method for the simultaneous inversion of near-field waveforms for source and structure parameters. This is desirable in order to determine the extent to which assumptions of the velocity structure affect estimates of source parameters. The simultaneous inversion automatically provides quantitative information on parameter trade-offs, as well as error analyses on the resultant models. The inversion also provides a means of determining source parameters at sites where no structure model previously exists, as would be the case in an on-site verification experiment. Test inversions are presented, as well as preliminary results of inversions of vertical velocity waveforms from Pahute Mesa events. The second part of this report addresses the implications of choosing a particular representation of the RDP on the determination of the teleseismic attenuation operator. Using source parameters determined from near-field modeling assuming either the Mueller-Murphy or Helmberger-Hadley effective source functions, time-domain amplitude and period information from a large set of short-period, WWSSN teleseismic recordings were modeled to determine both frequency-independent and frequency-dependent Q models. Including spectral shape data in the 0.5 to 4 Hz band as constraints, either source model, when convolved with a frequency-dependent Q operator, is consistent with both near-field and teleseismic observations.

PART I

SIMULTANEOUS INVERSION OF NEAR-FIELD DATA
FOR EXPLOSION SOURCE AND STRUCTURE PARAMETERS

by

Jeffrey S. Barker and L. J. Burdick

ABSTRACT

The determination of source parameters for underground nuclear explosions through waveform modeling of near-field recordings is dependent upon the velocity structure model assumed between the source and receivers. In order to minimize errors due to inadequacies in the assumed structure model, we have developed a simultaneous inversion of near-field waveforms for source and structure parameters. The inversion automatically provides information on the trade-offs between parameters and error analyses of the resultant models. The source may be parameterized by any of several effective source functions, although for this study we use the representation of Helmberger and Hadley (1981). To minimize free parameters, the structure is parameterized as a layered stack of gradients defined by the velocity at the top of the layer, the velocity gradient within the layer and the depth to the top of the layer. The gradient model is then discretized into homogeneous plane layers, with the layer thickness defined as the wavelength of the predominant period in the data, and synthetics are computed using asymptotic generalized ray theory. For each observed waveform, the residuals consist of the normalized cross-correlation coefficient between the data and synthetics (a measure of waveform fit), the difference in the normalization factors (a measure of absolute amplitude), and the time lag to the peak of cross-correlation (a measure of absolute travel time). Numerical partial derivatives are computed by perturbing the starting model, and the problem is solved using an iterative generalized inverse.

Four test inversions of synthetic data sets are presented which illustrate the need to truncate eigenvalues and preferentially weight the

parameters and residuals in order to stabilize the inversion. Generally in these tests, when the parameters are well resolved, the inversion is quite robust and convergence is rapid. Preliminary results are presented for inversions of the vertical velocity waveforms from the Pahute Mesa events, BOXCAR, INLET, MAST and SCOTCH. For this report, the structure models are constrained to two gradients separated by a second-order discontinuity. The structure model obtained for BOXCAR is not significantly different than the Pahute Mesa model of Hartzell, et al. (1983), but the models obtained for INLET, MAST, and SCOTCH suggest a higher gradient in the upper layer, and poor resolution of the lower layer. The source models obtained in these preliminary inversions give higher estimates of Ψ_∞ than those of Barker, et al. (1985).

INTRODUCTION

The determination of source parameters for underground nuclear explosions through waveform modeling of near-field recordings is dependent upon the velocity structure model assumed between the source and receivers. While independent information may exist for some aspects of the structure, such as the velocity at the surface and the depths to the water table and basement, the detailed models are generally the result of laborious trial-and-error modeling of observed waveforms (e.g., Helmberger and Hadley, 1981; Hartzell, et al., 1983; Burdick, et al., 1984). Discretizations of velocity gradients into plane-layered structure models must be fine enough to avoid introducing high frequency errors into the source function determinations. For signals with frequencies up to 5 Hz and compressional velocities near 3 km/s, layer thickness should be less than about 0.6 km. This is particularly important near the source depth due to the interference of upgoing and diving energy over near-field ranges. Thus an adequate structure model for near-field waveform modeling might consist of more than ten layers in the top 10 km of the crust. There is obviously a premium to be paid before undertaking the modeling of sources at different test sites. Further, the structure model obtained is, to a certain extent, dependent upon the source function used during the modeling procedure. The result is clearly non-unique and the extent of the trade-offs cannot easily be quantified.

One solution to this problem is a simultaneous inversion for source and structure parameters. The complexity of wave interaction in the near-field makes such an inversion an approximate and somewhat costly endeavor. Nevertheless, while the models obtained by such an inversion may not be

intrinsically "better" than their trial-and-error counterparts, a suitable choice of inversion method will automatically provide invaluable information concerning parameter and data resolution. Not only can the source vs. structure trade-offs be quantified in this way, but also the trade-offs within the source and structure parameterizations (such as the B- trade-off in the RDP) may be determined. We also obtain an indication of which aspects of the observed data are most important in constraining the solution.

This section of this report includes discussions of the development of such an inversion, test inversions using synthetic data sets, and applications to near-field data from the Pahute Mesa test site. Following reports will include inversions of data from other test sites, as well as modifications of the assumed parameterizations for the Pahute Mesa events.

BACKGROUND

The vertical displacement due to an explosion source may be written using first order asymptotic generalized ray theory as (see for example, Helmberger and Harkrider, 1978)

$$w(r,t) = \Psi'(t) * \frac{1}{\pi} \sqrt{\frac{2}{r}} \frac{d}{dt} \left(\frac{1}{\sqrt{t}} * \sum_i^{\text{rays}} R_i(p) \right) \quad (1)$$

where * denotes convolution, $\Psi'(t)$ is the time derivative of the reduced displacement potential (RDP), and

$$R_i(p) = \text{Im} \left(\frac{\sqrt{p}}{\eta_\alpha} R_{NZ}(p) \Pi_i(p) \frac{dp}{dt} \right)_c \quad (2)$$

which is evaluated along the Cagniard contour. p is the ray parameter, η_α is the vertical wave slowness ($\eta_\alpha = \sqrt{\alpha^{-2} - p^2}$), $R_{NZ}(p)$ is the receiver function defined by Helberger (1974), and $\Pi_i(p)$ is the product of reflection and transmission coefficients along the path for each ray.

For the inversion, we need to compute the partial derivatives of (1) with respect to the individual parameters of the source and velocity structure. The partial with respect to structure parameters, say the velocity of the j^{th} layer, v_j , reduces to the evaluation of

$$\frac{\partial R_i(p)}{\partial v_j} = \frac{\partial R_i(p)}{\partial p} \frac{\partial p}{\partial v_j} \quad (3)$$

which consists of evaluating the partials of the various terms in (2) as a function of the complex ray parameter along the Cagniard contour, while the contour itself varies with changes in the velocity parameter. This evaluation must be made for each ray, then summed to obtain the partial derivative.

Previous structure inversions based on waveform modeling have invoked a variety of approximations in order to simplify (3). Mellman (1980) utilized a modified first motion approximation, such that rapidly varying terms in (2) are approximated by evaluating them only at the geometric ray parameter. Shaw (1983) and Chapman and Orcutt (1985) used the WKBJ approximation to invert marine reflection/refraction data, and Brown (1982) employed a similar

approach to obtain the ocean sound speed profile. Since the WKBJ approximation becomes invalid where large velocity gradients exist, or where discontinuities are encountered near the turning depth of a ray, Given (1984) developed a hybrid WKBJ-generalized ray approach to obtain upper mantle structure. In inverting long-period, regional P_{nl} waveforms for average crustal structure, Wallace (1983) generated average generalized ray Green's functions, which were "stretched" or "squeezed" to simulate perturbations in the structure model.

In forward modeling of near-field waveforms, Burdick, et al. (1982) and Barker, et al. (1985) have shown that the observed waveforms result from the interference of upgoing and diving rays, as well as surface reflections. This interference is particularly sensitive to the velocity gradient near the source depth. Each synthetic seismogram consists of a superposition of rays from a variety of take-off angles that sample different portions of the structure. An algorithm designed to determine if and when the modified first motion, WKBJ and other approximations are appropriate for a particular ray, to compute the analytic partial derivatives, and sum over rays would be of questionable efficiency and accuracy. Instead, numerical partials may be computed by evaluating the terms in (3) along the complex ray parameter for each ray. This approach is obviously nonlinear, and care must be taken to stabilize the resulting parameter changes. For simpler problems, the computation of numerical partial derivatives would be quite inefficient, but given the complexity of the near-field waveform modeling problem, the accuracy of the method will more than counterbalance the computational cost.

A number of techniques have been used to obtain source parameters by inversion of body waveforms. Burdick and Mellman (1976) inverted teleseismic

body waves to obtain the orientation and time history of the Borrego Mt. earthquake. Several investigators have inverted teleseismic body waves to obtain the seismic moment tensor. A few examples include Stump and Johnson (1977), Langston (1981), Dziewonski, et al. (1981) and Nabelek (1984). To our knowledge, the first inversion of near-field data for explosion source parameters was performed by Stump and Johnson (1984). McEvilly and Johnson (1986) and Wallace (1986) have recently reported on similar applications. In these studies, the six independent elements of the moment tensor are obtained and the relative amplitudes and time histories of the isotropic and deviatoric parts are interpreted in terms of explosion and tectonic release sources, respectively. Because the moment tensor is free to take on any value, and because the velocity structure model is fixed, it is entirely possible that errors in the structure model and noise in the data could map into the non-isotropic moment tensor. In addition, since no constraints are placed on the form of the isotropic time history, it is not easily interpreted in terms of the parameters of common representations of the explosion RDP.

Because of our assertion that errors in the velocity structure adversely affect explosion source parameter estimates, we are interested in approaching these problems before tackling source complexity. Therefore, our preliminary inversions will constrain the explosion source to be isotropic, and we will constrain the source time history to have the form of the time derivative of the RDP. Various forms of the RDP may be considered, and the ramifications of that choice will be investigated in future work. After evaluating these results, the source parameterization could be generalized to allow the source time history to take on an arbitrary shape. At a later stage, a deviatoric moment tensor source representing tectonic release could be added to the

isotropic source, with the latter constrained to the known depth and origin time of the explosion. Inverting for a single, six-component moment tensor, however, constrains the non-isotropic portion of the source to occur at the same location as the explosion. While this may turn out to be the case, near-field observations should allow resolution of spatial separations in the two sources, so such a constraint may be unreasonable.

INVERSION METHOD

The layered structure models required for generalized ray synthetics may be considered discretizations of one or more velocity gradients separated by first- or second-order discontinuities. In order to minimize the number of free parameters in the inversion, we will utilize this fact and solve not for the velocities and thicknesses of individual layers, but for the velocity gradient and the velocity at the top of the gradient. As shown in Figure 1, the discretized model follows this gradient, with layer thicknesses determined by the wavelength of the predominant period in the data. Shear velocity and density may be free parameters, or may be related to the compressional velocity by predefined constants. In general, the free parameters are the gradient within each layer, the velocity at the top of the layer, and the depth to the top of the layer. Thus, for an n-layered structure in which shear velocity and density are not free parameters, the number of structure parameters in the inversion is $3n-1$. The number of gradients to be considered will be fixed for each inversion, so the optimal number will have to be determined by test inversions proceeding from simpler to more complex models.

Structure Parameterization

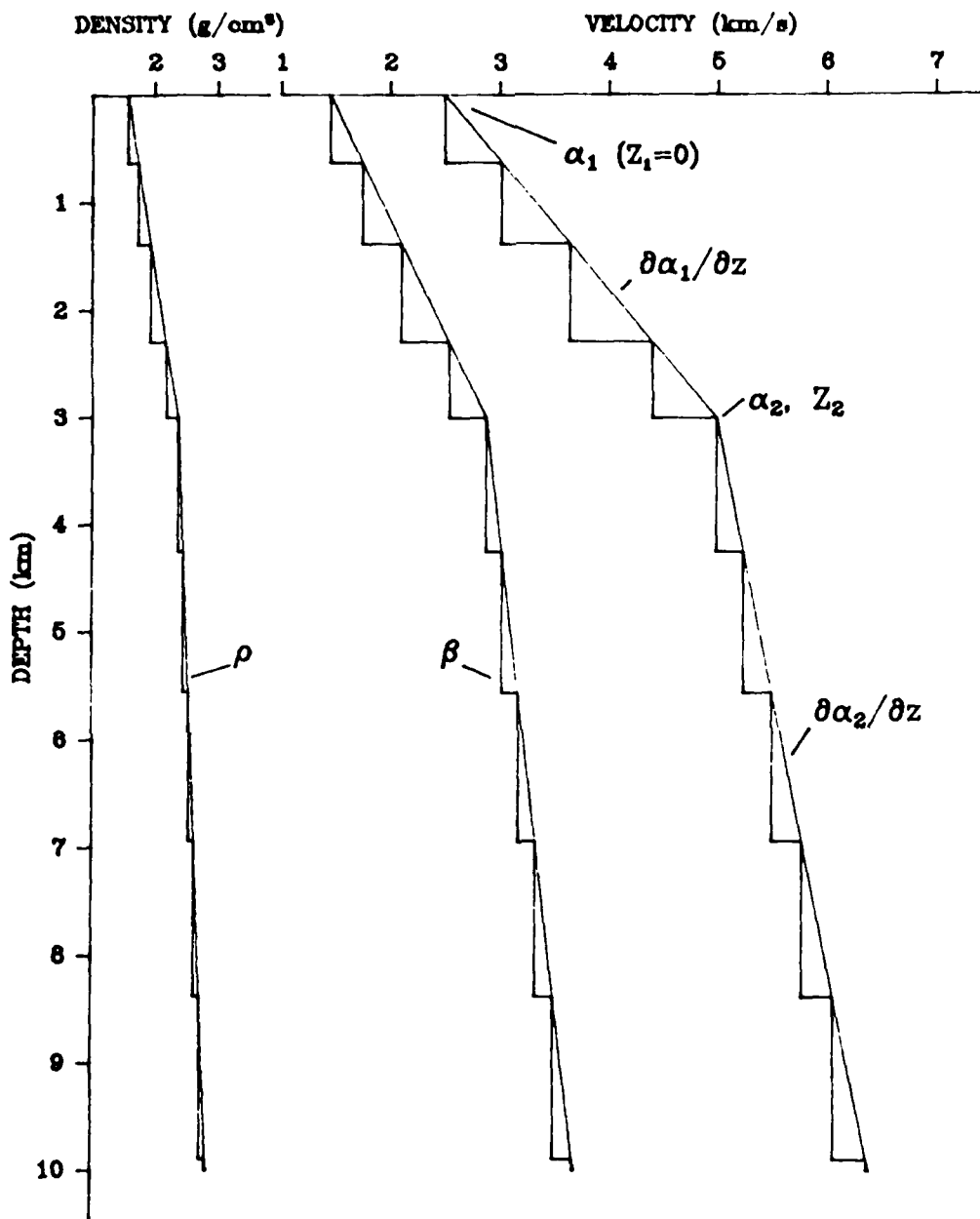


Figure 1. Structure model parameterization. The layered structure model is discretized from one or more velocity gradients defined by the values of the gradient, the velocity at the top of the gradient and the depth to the top of the gradient. The depth increment is defined as the product of the P-wave velocity and the predominant period of the data (typically 0.25 sec). S-wave velocity and density are linearly related to the P-wave velocity. The case shown consists of two gradients separated by a second-order discontinuity.

Constraints such as the depth to the water table, or that a particular interface may have only a second-order discontinuity, reduce the number of free parameters while increasing non-linearity of the inversion.

Since the discretized velocity model will vary from iteration to iteration as well as with the model perturbations required to compute the numerical partials, the ray set from which the synthetics are computed will also vary. Barker, et al. (1985) found that the first one or two cycles of vertical velocity observations at near-field ranges were well modeled by including the upgoing direct ray, a sum of diving rays that constitute turning, reflecting and critically refracting energy, and a sum of rays that depart upward, reflect from the free surface and follow diving ray paths. If radial observations are to be modeled, or if later portions of the waveform are considered, P-to-S conversions at the free surface and at discontinuities should be included. An algorithm to generate this ray set for each new layered structure is simple to implement, and computational time is saved by culling rays which arrive outside the inversion time window, or whose amplitude will be below some predefined cutoff level.

For this report, the source parameterization follows the form of the RDP proposed by Helmberger and Hadley (1981):

$$\Psi(t) = \Psi_{\infty} \left\{ 1 - e^{-Kt} [1 + Kt + \frac{1}{2}(Kt)^2 - B(Kt)^4] \right\} \quad (4)$$

where Ψ_{∞} represents the static value, K represents the rise time, and B represents the overshoot. Haskell (1967) proposed that the polynomial in (4) should be quartic, while Mueller and Murphy (1971) and von Seggern and Blandford (1972) suggest quadratic forms. Barker, et al. (1986) showed that a

cubic RDP convolved with elastic Green's functions explains near-field observations. A quadratic RDP can explain the near-field observations equally well as long as the Green's functions include the effects of depth-dependent crustal attenuation. Although attenuation could be included in the inversion, this would greatly increase the number of free parameters, and attenuation parameters would likely be poorly resolved. Initially therefore, we choose the Helmberger-Hadley RDP and elastic wave propagation as the simpler model. The effective source function may be obtained by taking the first (displacement), second (velocity) or third (acceleration) time derivatives of the RDP. As may be seen from (4), the RDP and its time derivatives are linear in Ψ_∞ and B, but not in K. Burdick, et al. (1982) indicated that Ψ_∞ and B trade off nearly totally in modeling near-field velocity records. While this trade-off may be quantified by allowing both parameters to vary in the inversion, useful source estimates may require that B be constrained.

The linearized least-squares inverse may be obtained by solving

$$\Delta c' = A' \Delta p' \quad (5)$$

in which $\Delta c'$ is the residual vector, containing the differences between observed and synthetic data, A' is the matrix of partial derivatives, and $\Delta p'$ is the desired vector of parameter changes. Perhaps the simplest determination of the residual vector is a point-by-point difference of observed and synthetic seismograms within the time window. This implies, however, that neighboring points in a seismogram represent independent observations, which is generally not the case. On the other hand, since each seismogram reflects a lagged sum of rays which sample different portions of

the structure, the resolution of parameters varies through the time window, and a single observation for each seismogram underestimates the information contained in the waveform.

Burdick and Mellman (1976) utilized an error, or residual, function based on the normalized cross-correlation coefficient between observed and synthetic waveforms. That is,

$$e_i = 1 - \max(\hat{o}_i \underline{cc} \hat{s}_i) \quad (6)$$

where

$$\hat{o}_i(t) = \frac{o_i(t)}{\left(\int o_i^2(t) dt\right)^{1/2}} \quad (7)$$

and

$$\hat{s}_i(t) = \frac{s_i(t)}{\left(\int s_i^2(t) dt\right)^{1/2}} \quad (8)$$

$\hat{o}_i(t)$ is the i^{th} observed seismogram, $\hat{s}_i(t)$ is the i^{th} synthetic seismogram and cc denotes cross-correlation. This error function has become popular because it is sensitive to the shapes of the waveforms, while the normalization makes it insensitive to absolute amplitude, and measuring the maximum of the cross-correlation makes it insensitive to absolute time. In the near-field problem, however, absolute amplitude and time are well calibrated, and should be fit by the resultant model. Therefore, in addition

to (6), our residual will include for each seismogram the relative difference in the normalization factors,

$$a_i = \frac{(\int o_i^2(t) dt)^{1/2} - (\int s_i^2(t) dt)^{1/2}}{(\int o_i^2(t) dt)^{1/2}} \quad (9)$$

which is a measure of absolute amplitude residual, and the time lag to the maximum of the cross-correlation, t_i , which is a measure of absolute time residual. The residual vector is now defined as

$$\Delta c' = [e_1, a_1, t_1, e_2, a_2, t_2, \dots, e_m, a_m, t_m]^T \quad (10)$$

for m seismograms and the objective function to be minimized by the inverse is

$$r = \sum_m (e_i^2 + a_i^2 + t_i^2) . \quad (11)$$

With this choice for the residual function, the numerical partial derivatives become, rather than (3),

$$\frac{\partial e_i}{\partial p_j} = \frac{(e_i(p_j + \Delta p_j) - e_i(p_j - \Delta p_j))}{2 \Delta p_j} \quad (12)$$

where Δp_j is the perturbation to the starting model parameter, p_j . The partials $\partial a_i / \partial p_j$ and $\partial t_i / \partial p_j$ have similar form.

Now that we have defined the form of the residual and parameter change vectors, we may redefine the matrices in (5) as

$$\Delta_c = s^{-1/2} \Delta_c'$$

$$\Delta_p = w^{-1/2} \Delta_p' \quad (13)$$

$$A = s^{-1/2} A' w^{1/2}$$

in which s is the covariance matrix of the residuals and w is a weighting matrix of the parameter changes. For simplicity, we assume that errors are uncorrelated, so s is diagonal. If an estimate of the residual variance is known (e.g., timing errors), that value is used in s . Otherwise, the residual variances are inversely related to the relative confidence in the residuals. The basic purpose of the diagonal matrix w is to counter the dimensionality of the parameterization of source and structure. Obviously velocity gradient (with values on the order of 1 km/s/km) and Ψ_∞ (values of 10^{10} cm³) should not be weighted equally. Due to nonlinearity, the weighting factors are also used to stabilize the parameter changes. For example, if a parameter changes to an unreasonable value or oscillates about some value, the weight of that parameter is decreased and the inversion is repeated. This introduces a certain degree of uncertainty in interpreting the variances of the parameter changes, since these now include the effects of the somewhat arbitrary weights necessary due to nonlinearity. Although convergence criteria may be utilized to determine when to stop an inversion, we have not implemented such an approach, but simply allow additional sets of five iterations until convergence is deemed complete or unattainable. Finally, following Jackson (1979), a priori constraints may be placed on the parameter changes so that,

for example, the velocity cannot be negative, or so that source parameters must fall within a range of reasonable values.

The weighted version of (5) may be solved by a linearized generalized inverse (Wiggins, 1972) such that

$$\Delta p = A^+ \Delta c = V \Lambda^{-1} U^T \Delta c \quad (14)$$

in which Λ is the diagonal matrix of non-zero singular values of A , V is the corresponding matrix of eigenvectors which spans the parameter space, and U is the matrix of eigenvectors that spans the residual space. Since the problem is non-linear, the inversion is iterative and minimizes both the least-squares error, $|A \Delta p - \Delta c|^2$, and the length of the parameter changes, $|\Delta p|^2$. Since small singular values result in large parameter changes, an a priori cut-off is specified, below which the singular value is assumed to be zero, and the dimension of the parameter space is truncated. The variances of the parameter changes are given by

$$\sigma_i^2 = \sum_j^k v_{ij}^2 / \lambda_j^2 \quad (15)$$

and include the effects of the parameter weighting matrix. The parameter trade-offs that result from singular value truncation may be determined by an inspection of the parameter resolution matrix,

$$R = V V^T, \quad (16)$$

which reduces to the identity matrix in the case of perfect resolution. If

during test inversions, the parameter resolution is deemed unacceptable, adjustments may be made in the parameter weights or the singular value cut-off, and the inversion may be repeated. The importance of particular observations or residuals in the inversion may be determined from the information density matrix,

$$S = U U^T \quad (17)$$

or its diagonal, the data importance vector. This may indicate, for example, that the parameter changes are most sensitive to the absolute amplitude residual at nearer receivers, and to the absolute time residual at more distant receivers. The data importance vector from test inversions may suggest modifications to the observation weights.

Shaw and Orcutt (1985) use a different approach to solve the linearized inverse (which they attribute to Parker, unpublished manuscript, 1985). Rather than inverting the equation

$$\Delta c = A \Delta p \quad (18)$$

they add $A p_0$ (where p_0 contains the starting model) to both sides and invert

$$(\Delta c + A p_0) = A (p_0 + \Delta p) = A p_1 \quad (19)$$

to solve directly for the new model parameters, p_1 . The benefit of (19), which they term the "jumping" method, is that rather than minimizing the parameter changes and obtaining a model dependent on the starting model, one

minimizes (by some appropriate norm) the resulting model itself. An additional benefit is that while a priori constraints on the model parameters (after Jackson, 1979) may be desired, it is often difficult to transform these into constraints on the parameter changes. Although we have not yet implemented or tested the "jumping" method, it would seem to be applicable to the near-field inversion.

TESTS OF THE WAVEFORM INVERSION PROCEDURE

Test # 1 - Halfspace Velocity

As a simple initial test of the inversion for velocity structure, we generated a synthetic data set for an explosion source in a halfspace. The compressional velocity in the halfspace was 6.0 km/s, the shear velocity was 3.44 km/s (a Poisson solid) and the density was 3.0 g/cm³. The source was represented by a Helmberger-Hadley (1981) RDP with K=7.0 s⁻¹, B=1.0 and $\Psi_\infty = 1.0 \times 10^{10}$ cm³, and was located at a depth of 1.0 km. Vertical component velocity synthetics were computed for ranges of 2, 4, 6, 8, 10 and 12 km. Since the object of the test inversion is the halfspace velocity, we constrain the structure to be a single layer with a zero velocity gradient.

In such a simple case, it is instructive to investigate the residuals as a function of the parameter values. In Figure 2 are the waveform residuals, e_i , absolute amplitude residuals, a_i , and travel time residuals, t_i , plotted as functions of receiver distance and halfspace velocity. Velocities from 5.0 to 7.0 km/s are considered in increments of 0.25 km/s. Since the body waveforms do not change with variations in the halfspace velocity, the

Halfspace Model Residuals

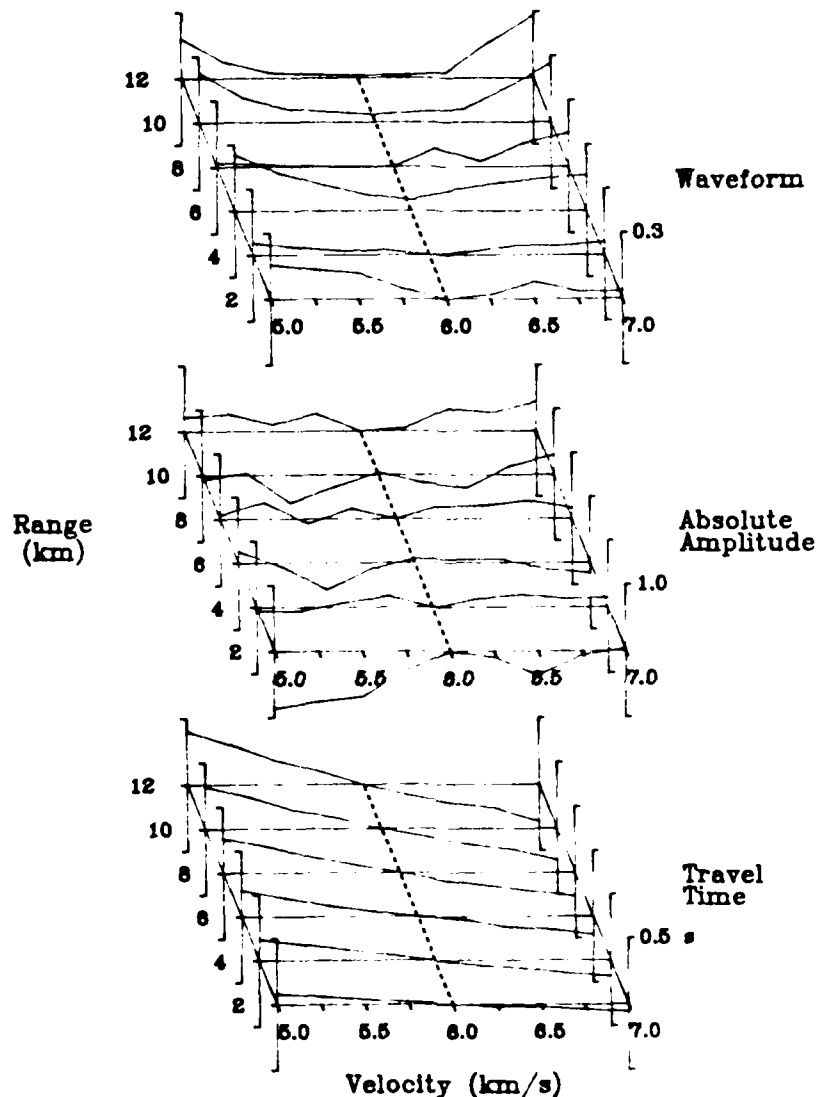


Figure 2. Waveform, amplitude and travel-time residuals for the halfspace model of Test # 1 as functions of receiver distance and velocity. The correct velocity is 6.0 km/s.

variations in waveform residuals are due to the truncation of the synthetic waveform as it is shifted with respect to the time window. The waveform residual is zero only when there is a perfect match: at the correct halfspace velocity of 6.0 km/s. Similarly, the absolute amplitude residual does not represent the difference in peak amplitudes between observed and synthetic waveforms, but rather the difference in the peak values of their autocorrelations. So, systematic amplitude variations due to velocity changes are superposed with truncation effects due to the time shifts relative to the window. Amplitude residuals may take on positive and negative values, and the sign is important in determining the partials. Only at the correct velocity (6.0 km/s) are the amplitude residuals at all of the receivers zero. The most sensitive measure of the correct halfspace velocity appears to be the travel time residual. This residual is linearly decreasing at all receivers for increasing halfspace velocity and, of course, the most distant receivers are most sensitive to variations in the velocity. The travel time residual is zero at all receivers for the correct velocity.

For simple problems with only a couple of free parameters, a grid-searching approach in which the minimum of the residuals is found by stepping through the parameter space would be quite reasonable, particularly in the presence of local minima. This is essentially the procedure used to generate Figure 2. The grid-searching approach, however, becomes quite unwieldy when the number of free parameters exceeds three or four, and does not readily supply information on the relative resolution of the parameters or the variance of the solution. In anticipation of more complex problems, therefore, we have performed the generalized inverse for the test case of determining the halfspace velocity from a starting model with a velocity of

5.0 km/s. If we were to invert only the travel-time residuals, Figure 2 indicates that the inversion would be linear. However, since the partials are computed by a linear difference of the residuals, the curvature in the waveform and amplitude residuals requires an iterative scheme. The partials are computed for perturbations of $\pm 10\%$ about the velocity of the starting model. Accounting for the dimensionality of the residuals, and utilizing the observation that travel time residuals appear to be most sensitive to halfspace velocity, we define the covariance matrix of the observations to be $\text{diag}(1.0, 1.0, 0.1)$ for the waveform, amplitude and time residuals at each receiver, respectively. Since there is only one parameter, the covariance of the velocity is set to 1.0. Five iterations were allowed, with no constraint or damping placed on the parameter changes. The results are listed in Table 1, and the waveforms for each iteration are plotted in Figure 3.

After only two iterations, the velocity determined is within 0.5% of the correct value, and convergence is complete after four iterations. The quality of fit may be determined by inspecting the waveforms in Figure 3, or by two objective measures listed in Table 1. The RMS fit is defined as $\text{RMS} = \sqrt{r / 3^*m}$, where r is the objective function (11) which is the sum of the squared residuals and 3^*m is the total number of residuals. The least-squares error is $\text{LSE} = |A \Delta p - \Delta c|^2$, and is a measure of the linearity of the inversion at each iteration. In initial inversions, the time windows were chosen to include the halfspace Rayleigh wave at each receiver. This, however, causes a strong local minimum to be formed at low velocities when the "synthetic" P wave correlates with the "observed" Rayleigh wave. Although the generalized ray synthetics are exact for the halfspace Rayleigh wave, they are generally inadequate for modeling surface waves for more complicated

Table 1 - Test # 1 Results - Halfspace Velocity

<u>Iteration</u>	<u>α (km/s)</u>	<u>RMS fit</u>	<u>Least-square error</u>
Start	5.000	0.277	
1	5.629	0.137	1.978
2	5.969	0.130	0.280
3	5.987	0.056	0.308
4	5.999	0.001	0.056
5	5.999	0.012	0.0002
Data	6.000		

structures. For both of these reasons, the inversion time windows were shortened to exclude the Rayleigh wave where it is separable from the P wave.

Test # 2 - A Single Gradient

For a somewhat more realistic test, and in order to test the discretization and ray summing procedures, a synthetic data set was generated for a single velocity gradient. The compressional velocity at the surface was set to 3.5 km/s and the velocity gradient was 0.5 km/s/km. The shear velocity was constrained to that of a Poisson solid ($1/\sqrt{3}$ times the compressional velocity) and the density was constrained (for simplicity in coding) to 1/2 the compressional velocity. The gradient was discretized using a predominant period of 0.25 s, which results in 10 layers in the top 15 km with layer thickness increasing with depth. All upgoing and diving P waves and the surface-reflected pP waves were considered, but culling late arriving rays resulted in 18 rays being summed for the final response. Once again,

Halfspace Velocity Inversion Results

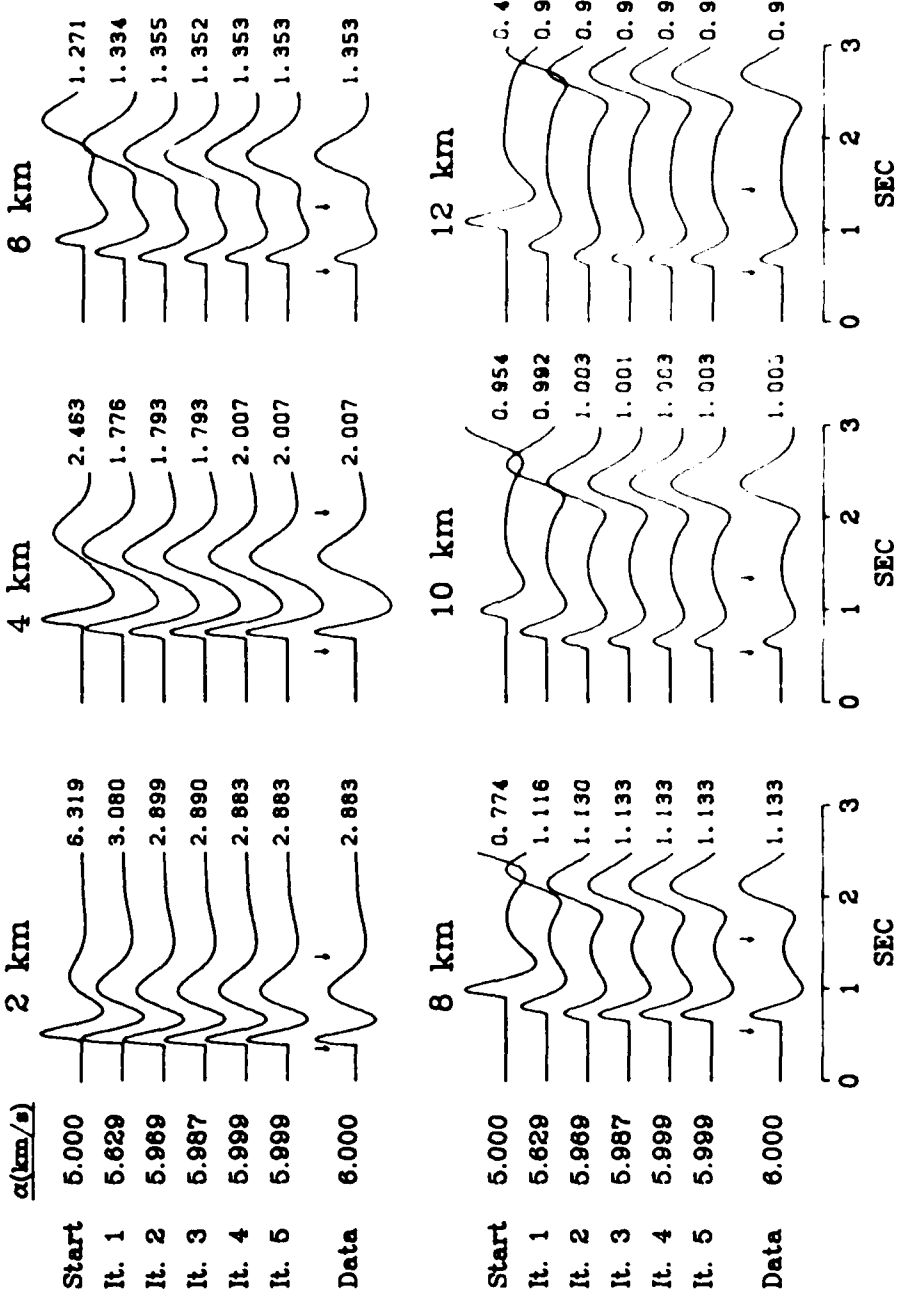


Figure 3. Results of the inversion for halfspace velocity in Test # 1. Synthetic seismograms are shown for the starting model and five iterations at each receiver. The data seismograms (also synthetic) are plotted below. Arrows above the data waveforms indicate the inversion time windows and numbers to the right are the peak trace amplitudes. The values of the parameter (halfspace velocity) for each iteration, and the correct value for the data, are shown to the left.

synthetic velocity seismograms were computed for ranges of 2, 4, 6, 8, 10 and 12 km.

Figures 4 and 5 illustrate the dependence of the waveform, absolute amplitude and travel time residuals at each receiver as functions of the velocity gradient and the velocity at the surface, respectively. As shown in Figure 4, since the waveforms at the nearer receivers are dominated by the upgoing P wave, which is relatively insensitive to the velocity gradient, there is very little variation in their residuals over the ranges of gradient considered (0.3 to 0.7 km/s/km). On the other hand, the waveforms at the farther receivers are dominated by diving turning rays, and their residuals (particularly travel time) resolve changes in the gradient quite well. Overall, it appears that velocity gradient in this simple example will be resolved by travel time residuals at farther receivers and amplitude residuals at all receivers. The residuals due to variations in surface velocity (Figure 5) are very similar to those for the halfspace test (Figure 2). The waveform residuals have a broad minimum, the travel time residuals are a robust measure of the correct surface velocity, and the amplitude residuals include variations due to truncation by the time window. In comparing Figures 4 and 5, it appears that the residuals are more sensitive to variations in surface velocity than velocity gradient. We will have to take this into account in assigning parameter weights in the inversion.

Before performing an inversion for surface velocity and gradient, it is instructive to invert for gradient only, constraining the surface velocity to its correct value. In this case, we define the covariance matrix of the observations according to the dimensionality of the residuals, but in addition, we wish to preferentially minimize the waveform residuals since

Gradient Model Residuals

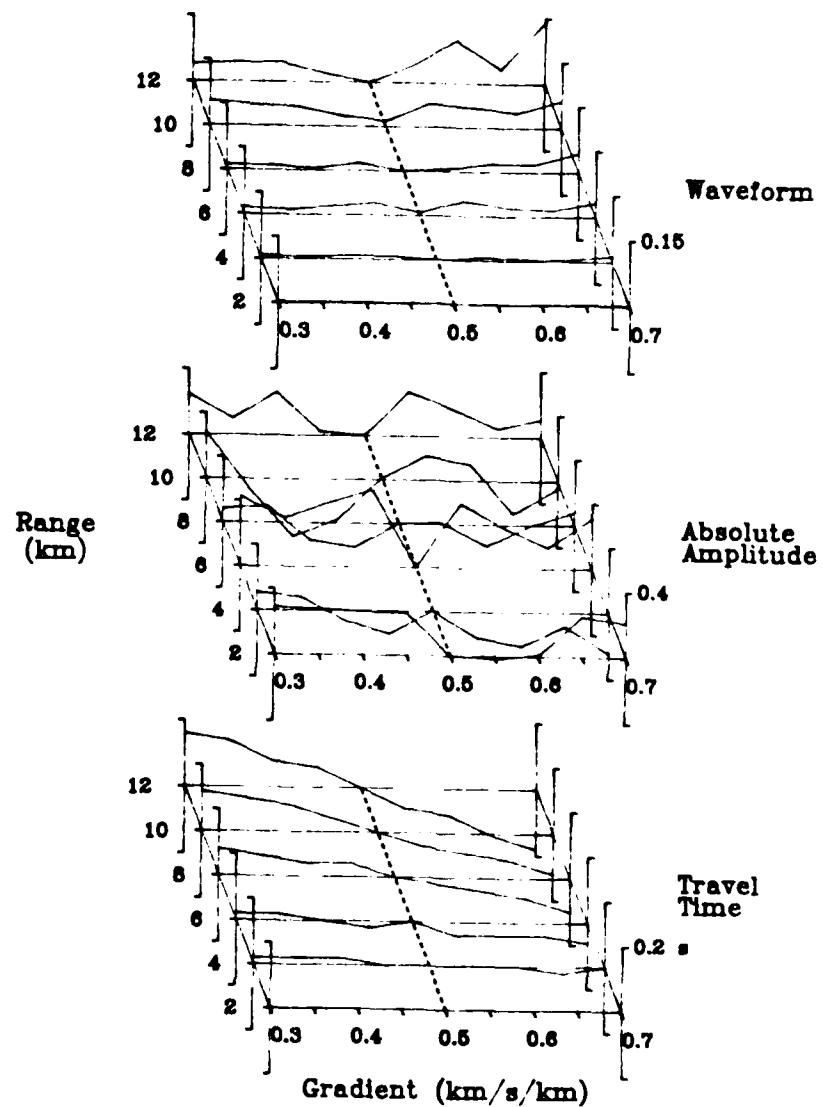


Figure 4. Waveform, amplitude and travel-time residuals for the gradient model of Tests # 2 and 3 as functions of receiver distance and velocity gradient. The correct gradient is 0.5 km/s/km.

Gradient Model Residuals

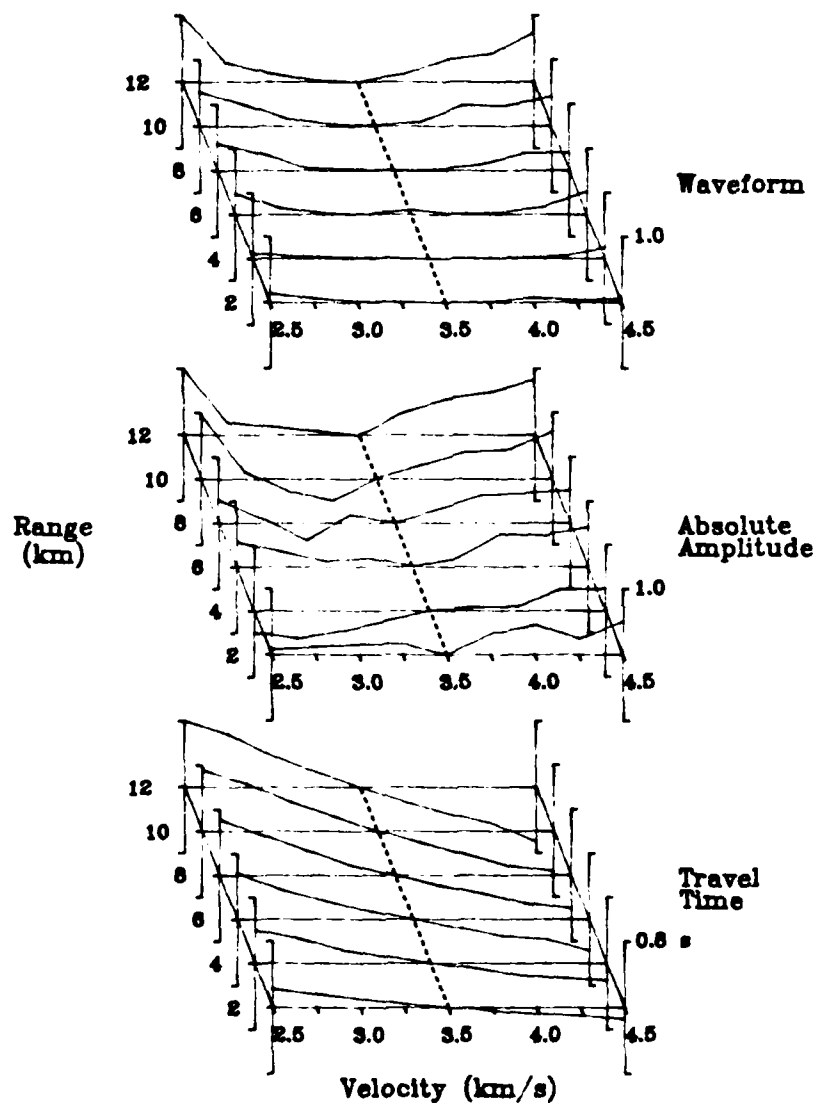


Figure 5. Waveform, amplitude and travel-time residuals for the gradient model of Tests # 2 and 3 as functions of receiver distance and the velocity at the surface. The correct velocity is 3.5 km/s.

changes in gradient appear to have significant effect on the details of the waveform. We define the matrix to be $\text{diag}(0.01, 1.0, 0.1)$ for waveform, amplitude and time residuals at each receiver, respectively. Partial derivatives are computed by perturbations in the gradient of $\pm 10\%$, beginning with a gradient of 0.6 km/s/km . The correct value is 0.5 km/s/km . Five iterations were allowed with no damping of parameter changes. The results of the inversion are listed in Table 2 and the waveforms for each iteration are plotted in Figure 6.

Convergence to the solution is much more difficult in this case. An inspection of the data importance vectors (Figure 7) indicates that the first iteration is primarily controlled by the waveform and travel time residuals at the 12 km receiver, with some influence by the waveform and amplitude residuals at 6 km . After this initial step toward the correct solution, the second and third iterations are controlled by the amplitude residuals at 6 and 10 km . As may be seen in Figure 4, the amplitude residuals at these receivers vary more rapidly for gradients slightly less than 0.5 km/s/km than for those slightly greater than 0.5 km/s/km . In the second iteration, the partial derivatives are computed based on the difference in the residuals at 0.573 and 0.469 km/s/km . Even though the latter is closer to the correct solution (0.5 km/s/km), its amplitude residual is larger in absolute value than the former, so the partial derivative of the amplitude residuals causes the solution to move away from the correct gradient. By the fourth iteration, the solution has moved far enough away that the lower bracket value used in computing the partials is approximately 0.5 km/s/km , and the partial is unaffected by the changes in the residuals for smaller gradients. Second derivative information, available by considering the residuals of the starting model as

Table 2 - Test # 2 Results - A Single Gradient

Iteration	Vα (km/s/km)	RMS fit	Least-square error
Start	0.600	0.102	
1	0.522	0.052	1.015
2	0.529	0.107	0.125
3	0.560	0.083	2.128
4	0.497	0.047	0.080
5	0.471	0.117	0.088
Data	0.500		

well as the bracket values, could minimize this instability. However, in an effort to reduce computational effort in inversions for larger numbers of parameters, partial derivatives will be computed from a one-sided perturbation from the starting model. In addition to nearly halving the required computations, this also decreases the range of parameter space over which the linear approximation for partials is made. The adequacy of the linear approximation is quantified by the least-squares error. Often the least-squares error will actually increase as the correct solution is approached due to the curvature of the residuals about that value.

Test # 3 - Velocity and Gradient

We have performed several test inversions for simultaneously determining velocity gradient and surface velocity. There is an obvious trade-off between these parameters, indicating the need to truncate small singular values. In

Gradient Inversion Results

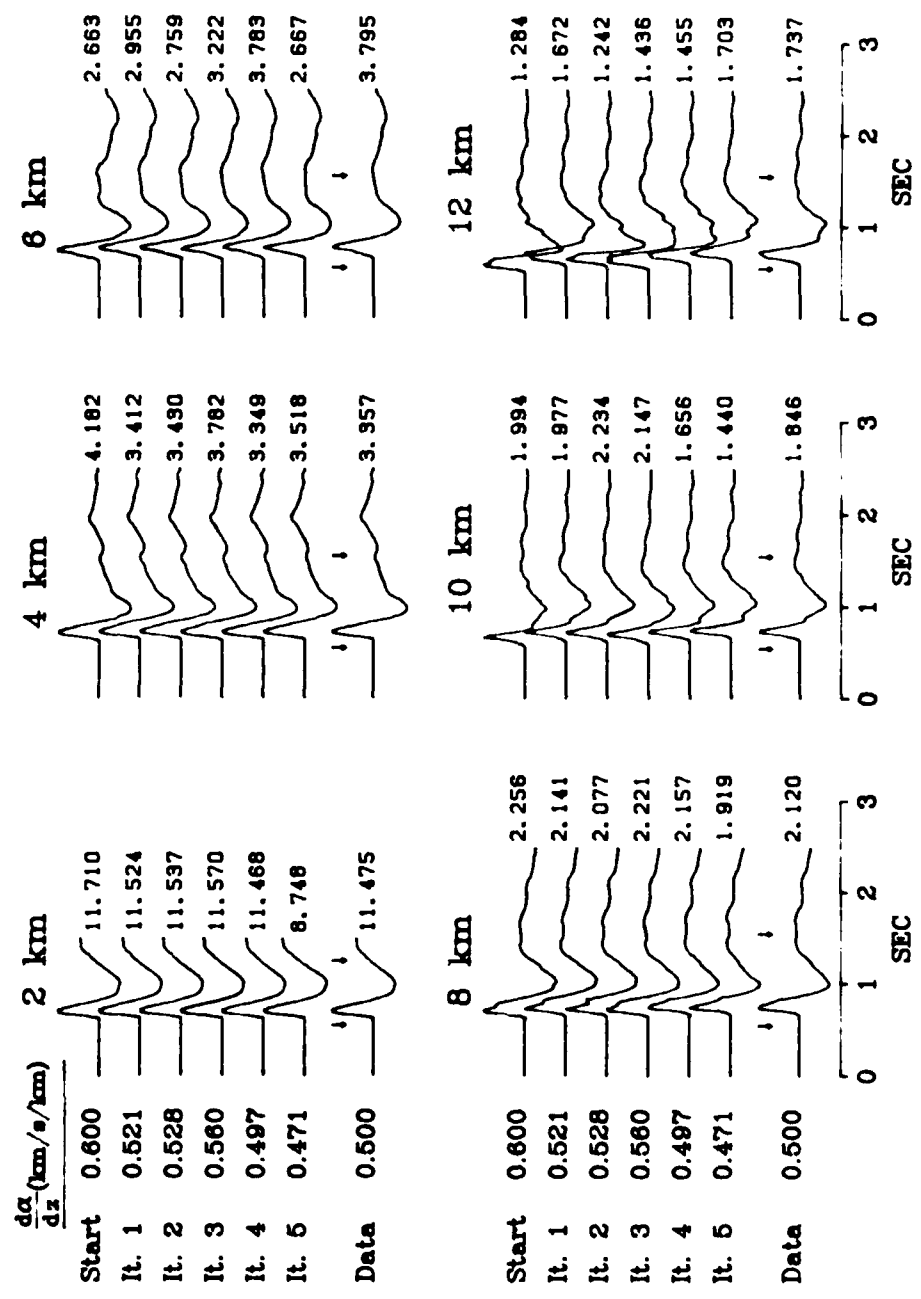


Figure 6. Results of the inversion for velocity gradient in Test # 2. The format is the same as in Figure 3, except that the parameter shown on the left is velocity gradient in km/s/km.

Test # 2 Data Importance Vectors

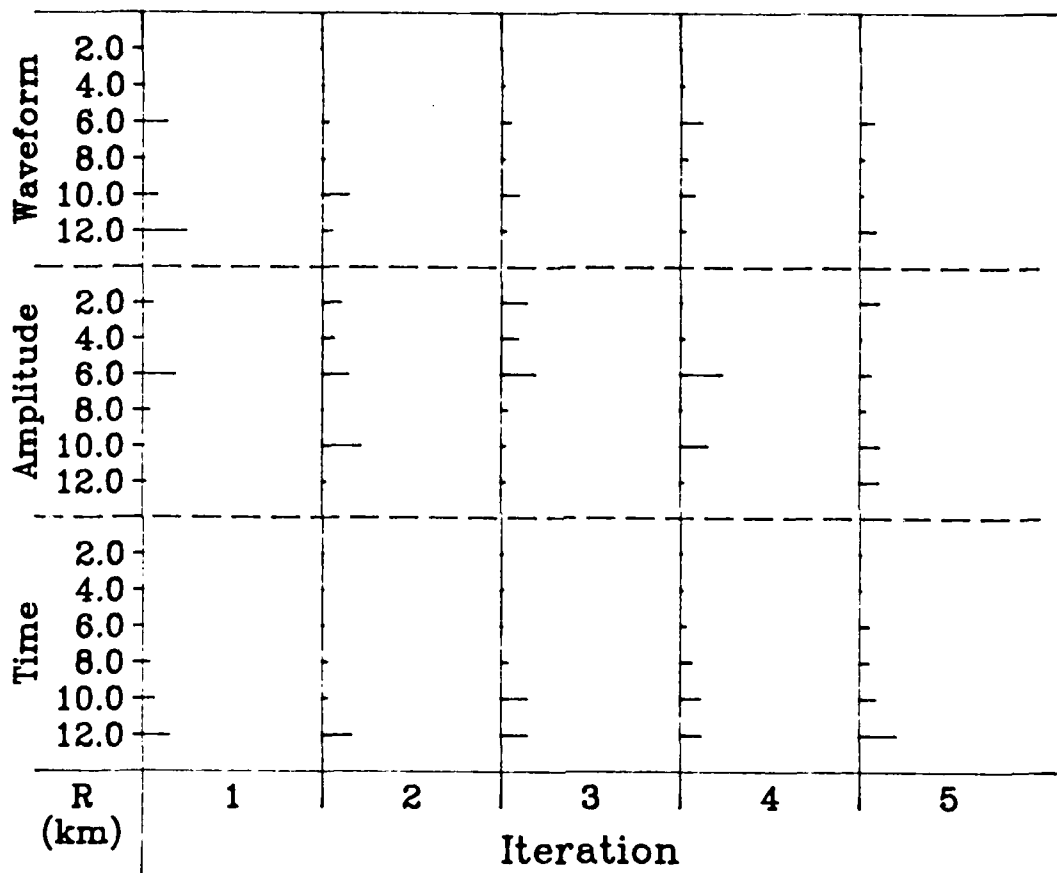


Figure 7. The data importance vectors for the Test # 2 inversion. Shown are the diagonals of the information density matrix for each iteration. The length of the ticks indicate the relative importance of the residuals at each receiver in the determination of the solution.

addition, however, the parameters should be weighted beyond that required by the dimensionality of the parameters. For the synthetic data set of the previous test, Figures 4 and 5 illustrated that the inversion appears to be more sensitive to variations in surface velocity than gradient. This means that a given residual value may be due either to a reasonable variation in surface velocity or a relatively larger variation in gradient. Since the inversion is non-linear, an error in surface velocity will be only partially corrected, while the gradient varies substantially to compensate. Inversions in which the parameters are equally weighted, or in which gradient is preferentially weighted will diverge. For this test, we have therefore defined the covariance matrix of the parameters such that surface velocity is preferentially weighted as $\text{diag}(1.0, 0.1)$ for surface velocity and gradient, respectively. The covariance matrix of the observations is $\text{diag}(0.1, 1.0, 0.1)$ for waveform, amplitude and travel time residuals, respectively. A cut-off was established so that one of the singular values could be truncated to avoid large variations due to poor resolution. Perturbations of $\pm 10\%$ were used to generate the partials. Ten iterations were allowed from a starting model with surface velocity of 2.5 km/s and a gradient of 0.4 km/s/km. The correct solution had a velocity of 3.5 km/s and a gradient of 0.5 km/s/km.

The results of the inversion are listed in Table 3, the waveforms from selected iterations are shown in Figure 8, and the resolution matrix for each iteration is shown in Figure 9. In the first iteration, both parameters are perfectly resolved and the change is toward the correct solution for both. In the second and following iterations, one singular value has been truncated. The weighting scheme has insured that the remaining eigenvector is oriented in the parameter space mostly in the direction of surface velocity, but with a

Table 3 - Test # 3 Results - Velocity and Gradient

Iteration	α (km/s)	R*	V_α (km/s/km)	R*	RMS fit	LSE
Start	2.500		0.400		0.598	
1	2.751	1.000	0.495	1.000	0.311	25.9
2	2.994	0.967	0.509	0.033	0.238	10.1
3	3.331	0.921	0.540	0.079	0.156	1.01
4	3.453	0.936	0.550	0.064	0.139	0.409
5	3.458	0.842	0.551	0.158	0.094	0.369
6	3.437	0.947	0.549	0.053	0.144	0.184
7	3.439	0.947	0.549	0.053	0.151	0.406
8	3.432	0.917	0.549	0.083	0.140	0.470
9	3.456	0.967	0.550	0.033	0.129	0.363
10	3.466	0.881	0.551	0.119	0.078	0.311
Data	3.500		0.500			

* value of the diagonal of the resolution matrix for this parameter.

small component in the gradient. This means that the second and following iterations consist mainly of modifications to the surface velocity, with only small (and perhaps incorrect) modifications to the gradient. After about five iterations, the model is slightly low in surface velocity, which is counterbalanced by a slightly high gradient. The waveforms from this combination are close enough to those of the correct solution, that parameter perturbations are relatively small in later iterations. Figure 8 shows that the primary effect of these later perturbations is to improve the absolute amplitude, since travel time and waveshape are already fairly well fit. This indicates that it may be desirable to allow the covariance matrix of the observations to change for later iterations, to allow the amplitude residual more influence on the solution.

Inversion for Surface Velocity and Gradient

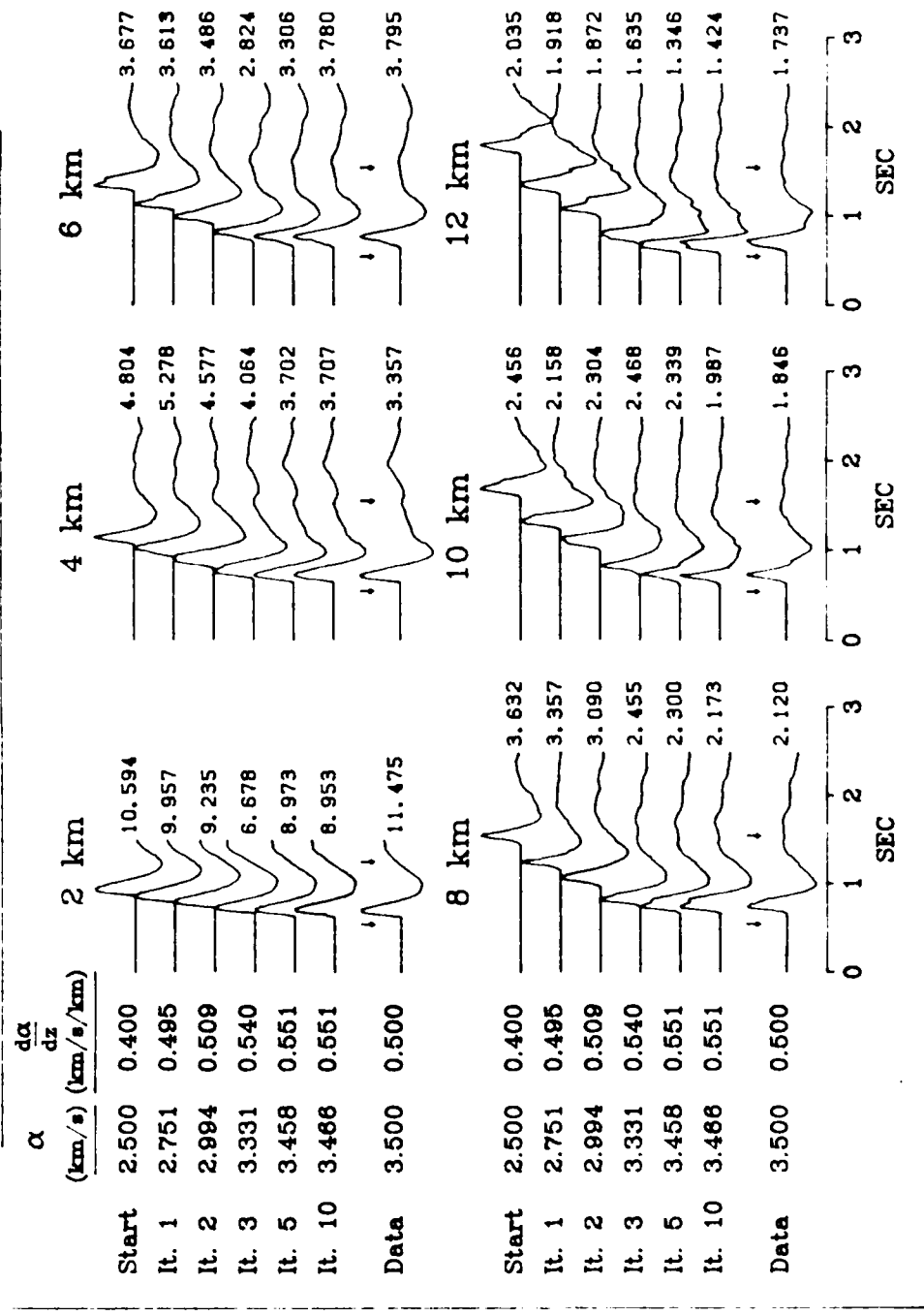


Figure 8. Results of the simultaneous inversion for velocity gradient and velocity at the surface in Test # 3. The format is the same as in Figure 3, except that both inversion parameters are printed on the left.

Test # 3 Resolution Matrices

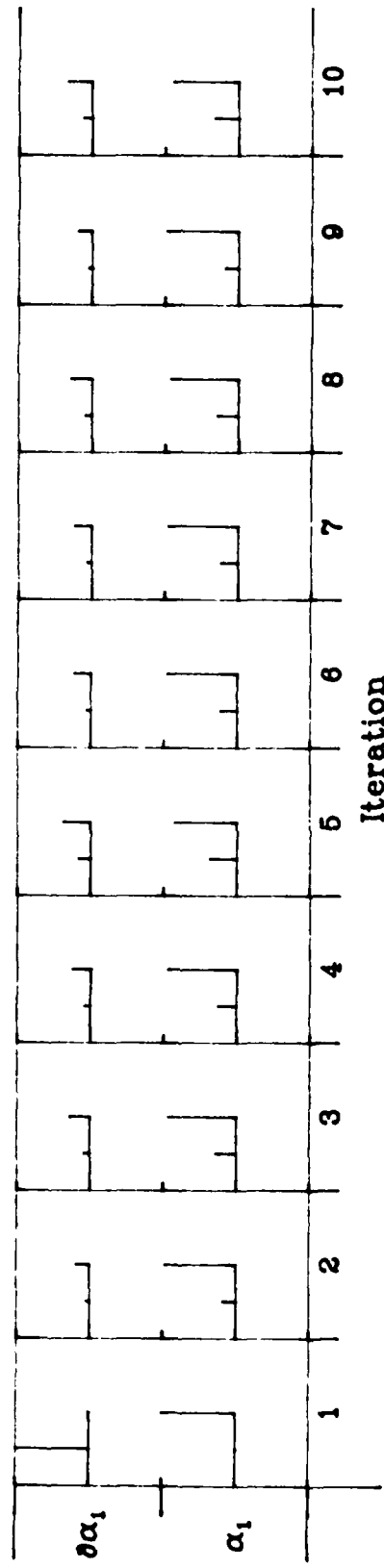


Figure 9. The parameter resolution matrices for each iteration of Test # 3. In the first iteration, the parameters are perfectly resolved and the matrix is the identity matrix (the ticks for both gradient and velocity have unit length). In following iterations, the parameters trade off, with velocity better resolved.

Test # 4 - Source and Structure

Finally, in order to test the simultaneous inversion for source and structure parameters, we generated a synthetic data set using a Helmberger-Hadley (1981) RDP and a two-layer gradient structure. The velocity structure was based on the model Hartzell, et al. (1983) obtained for Pahute Mesa, and consists of a surface velocity of 2.5 km/s and gradient of 0.83 km/s/km in the top layer. The second layer is separated from the first by a second-order discontinuity at a depth of 3.0 km and has a gradient of 0.20 km/s/km below that. For the source function, we set $\Psi_\infty = 1.0 \times 10^{10} \text{ cm}^3$, $k=7.0 \text{ s}^{-1}$ and $B=1$. Vertical component velocity synthetics were computed for a source at 1.0 km depth and for ranges from 2 to 12 km, later extended to 20 km.

Figure 10 shows the residuals for the six free parameters of a two-layer model with a second-order discontinuity for ranges of 2-20 km. In the figure, all of the residuals have been plotted on a scale with a maximum amplitude of 1.0 so that the relative resolution of the parameters may be inferred at a glance. Ψ_∞ affects only the amplitude residual, in a linear fashion and, of course, independent of range. k is also independent of range and affects predominantly the amplitude residual, but values well away from the correct one (7.0 s^{-1}) also affect the waveform and travel time residuals. This is because a change in rise time of the source affects the interference phenomena that determine the waveform and time of maximum correlation. Obviously Ψ_∞ and k will trade off, but k also includes trade-offs with other parameters. By far the most important parameter for the waveform and travel time residuals is the velocity at the top of the first layer. As in the halfspace velocity

Test # 4 Inversion Residuals

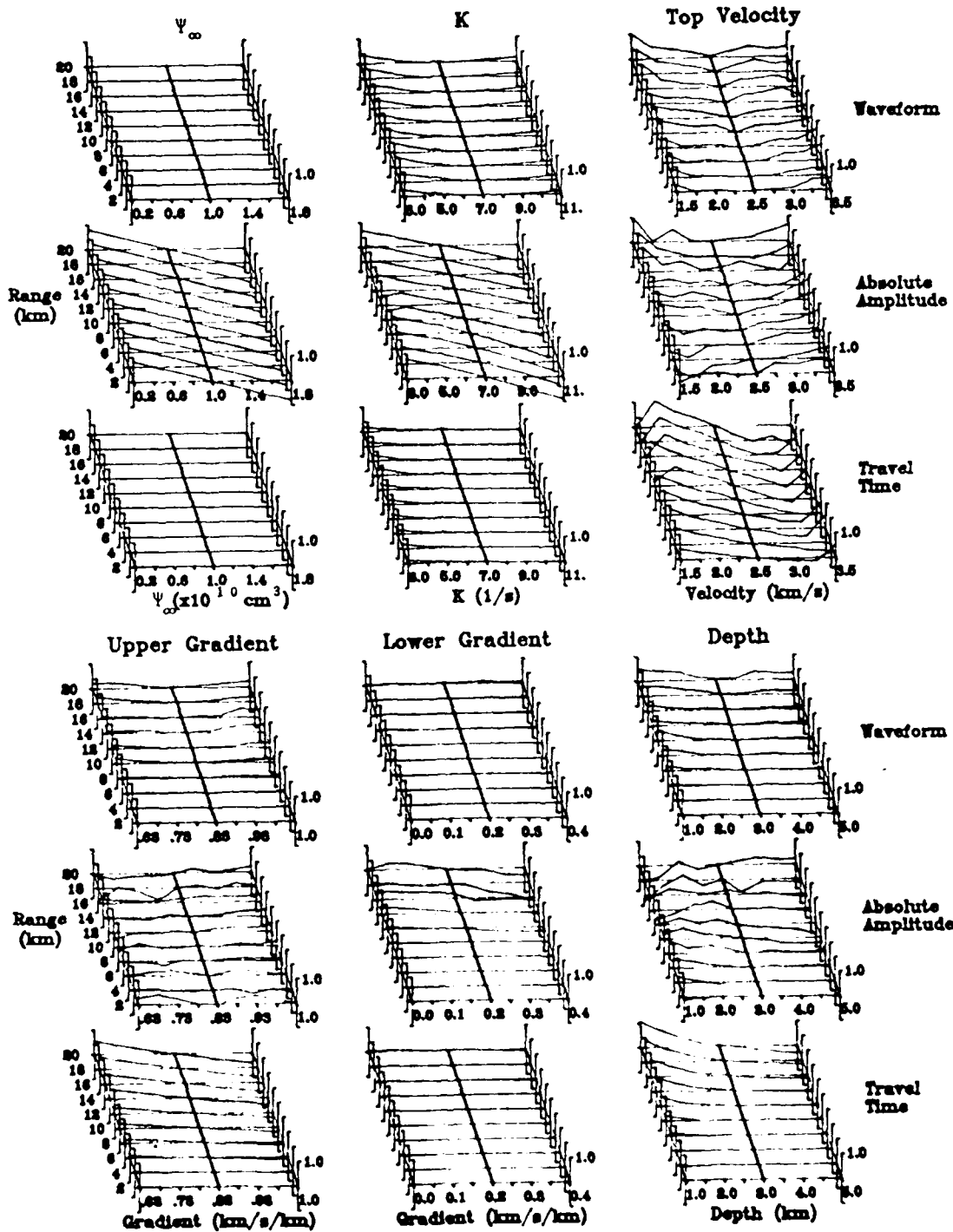


Figure 10. Waveform, amplitude and travel-time residuals for the six inversion parameters of Test # 4 as functions of receiver distance. All the plots have been scaled to a maximum residual value of 1.0, so that the relative sensitivity of the residuals to various parameters may be inferred at a glance. The correct value for each parameter is located at the center of each plot.

test, the travel time residual is linearly related to top velocity and the effect increases with range until portions of the waveform fall outside of the time window. As in Test # 2, the upper gradient is hardly resolved at all at the nearest receivers, and the residual minima are quite broad even at the farthest ranges. Due to the depth of the second layer in our synthetic model, the lower gradient is unresolved out to 10-12 km and the residuals are relatively quite small out to 20 km. Similarly, the interface depth parameter is resolved only when it approaches the source depth (1.0 km). Of course, if the top layer parameters are near their correct values, the residuals will be relatively more sensitive to variations in lower layer parameters.

A reasonable procedure for this and following inversions is to start with a simple parameterization to obtain preliminary estimates, then to increase the complexity of the model and refine the parameter estimates. This is particularly advisable when certain parameters are far better resolved than others. For example, we could solve initially for Ψ_∞ and k (holding B constant) and the parameters of a single gradient. Using these as starting values, we could then assume a second-order discontinuity and attempt to resolve the gradient and depth of the second layer. In addition to source and upper layer parameters, we are then inverting for a total of six parameters. Following this, we could free the second layer to have a first-order discontinuity (include the velocity at the top of the second layer), solving for seven parameters. As the estimates of the better resolved parameters approach their correct values, we could include a third or even a fourth layer, consider anelastic attenuation, or allow B to vary.

Table 4 and Figure 11 include the results of the first two steps of this inversion procedure applied to the synthetic data set. In the first five

Table 4 - Test # 4 Results - Source and Structure

Iteration	Ψ_∞ ($\times 10^{10}$ cm 3)	k (s $^{-1}$)	V_{α_1} (km/s/km)	α_1 (km/s)	V_{α_2} (km/s/km)	α_2 (km)	RMS fit
Start	2.00	9.00	0.50	2.00	-	-	1.098
1	1.33	6.70	0.63	2.50	-	-	0.298
2	1.33	6.71	0.78	2.54	-	-	0.231
3	1.33	6.72	0.83	2.50	-	-	0.253
4	1.33	6.70	0.87	2.47	-	-	0.245
5	1.32	6.68	0.95	2.39	-	-	0.228
[Start]*	[1.27]	[6.37]	[0.89]	[2.45]	[0.89]	[2.00]	[0.299]
6	0.72	6.20	0.89	2.46	0.58	2.29	0.208
7	0.84	6.22	0.89	2.44	0.49	2.56	0.200
8	0.94	6.25	0.89	2.45	0.44	2.57	0.174
9	0.91	6.24	0.89	2.44	0.43	2.57	0.183
10	0.91	6.24	0.89	2.45	0.39	2.68	0.165
Data	1.00	7.00	0.83	2.50	0.20	3.00	

* The starting model for iterations 6-10 was inadvertently changed from the model of iteration 5.

iterations, we solve for the source and upper layer parameters using synthetic data at ranges of 2-12 km. The parameter weighting matrix was defined as diag(0.01, 0.10, 0.01, 1.00) for Ψ_∞ , k, gradient, and top velocity, respectively. The covariance matrix of the residuals was diag(0.10, 0.10, 0.001) for waveform, amplitude and travel time residuals at receivers from 2-6 km, respectively. In order to improve resolution of the gradient, the waveform covariance of receivers from 8-12 km was decreased so that the covariance matrix became diag(0.01, 1.00, 0.001). Figure 12 presents the parameter resolution matrices for each iteration, and shows that the upper layer parameters are perfectly resolved through the first five iterations.

Test # 4 Inversion Results

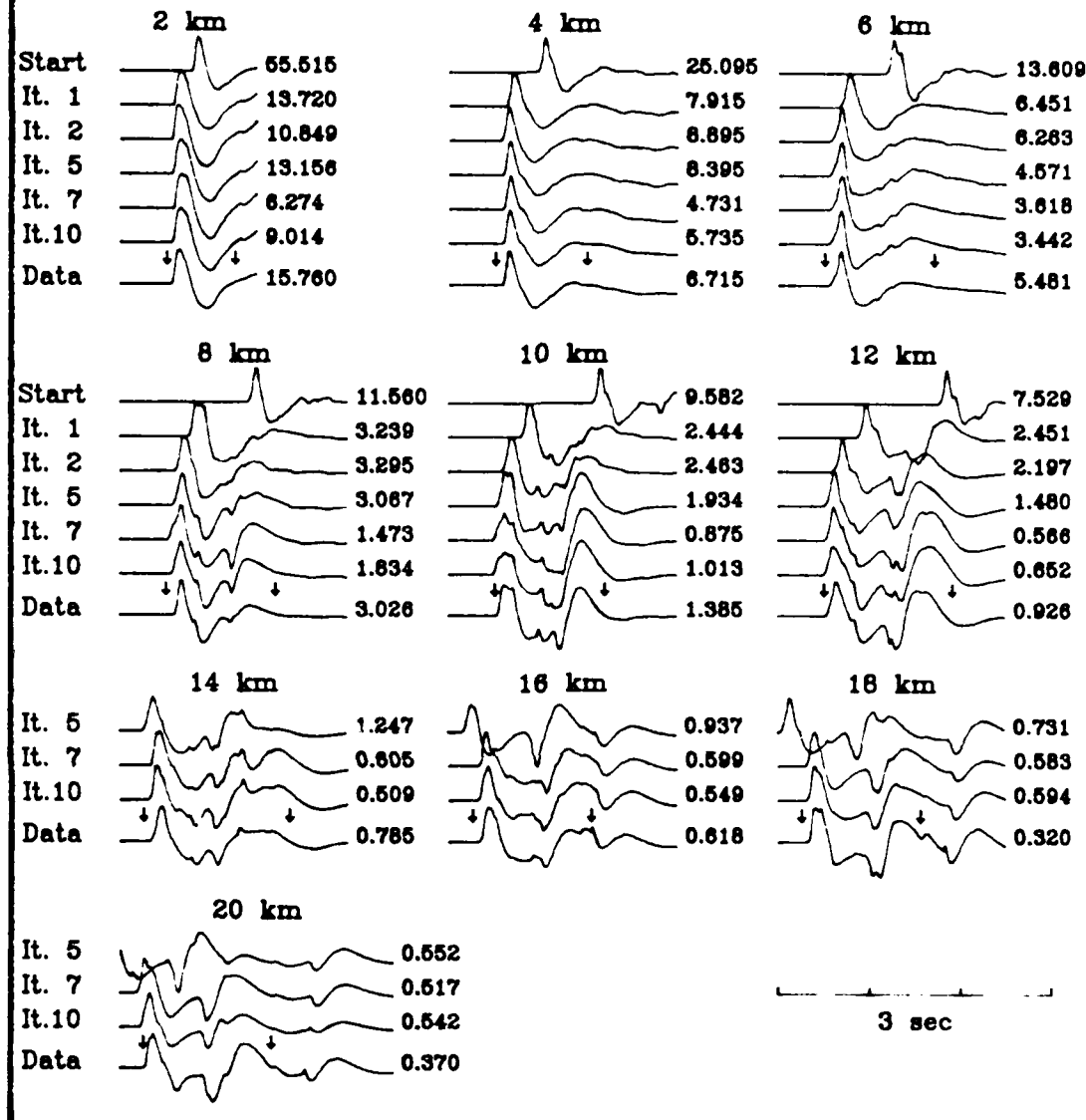


Figure 11. Inversion results for Test # 4. Shown are the waveforms of the starting model and the results of selected iterations (above) and the synthetic "data" (below). For the first five iterations, only waveforms at 2-12 km were inverted. Receivers at 14-20 km were included for iterations 6-10. The peak trace amplitudes are plotted to the right, and the inversion time window is denoted by the arrows. The time scale is shown at the bottom right.

Test #4 Resolution Matrices

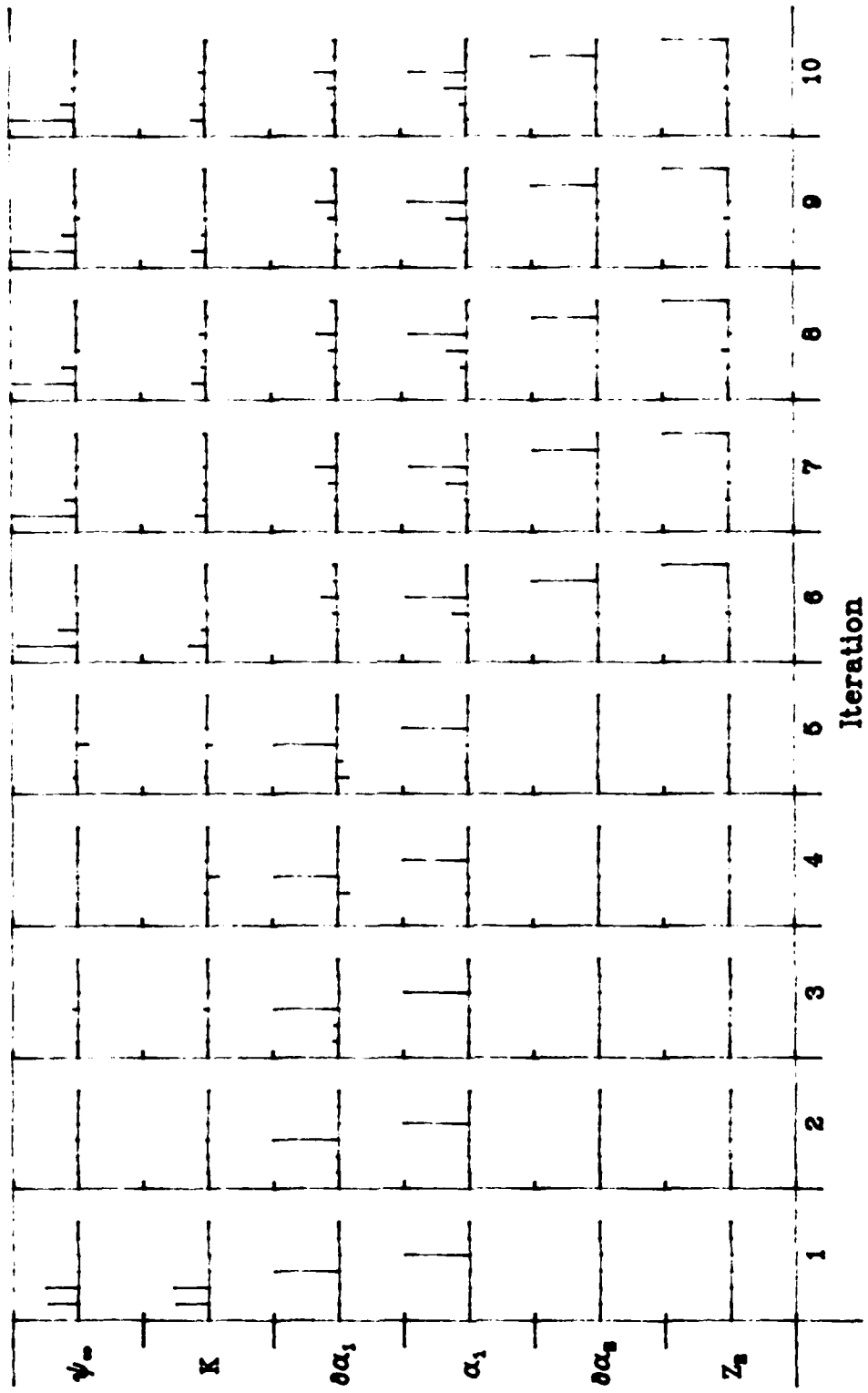


Figure 12. The parameter resolution matrices for each iteration of Test # 4. From top to bottom, the rows correspond to the source parameters, Ψ_∞ and k , and the structure parameters, upper gradient, top velocity, lower gradient and interface depth. In iterations 1-5, the lower structure parameters are not included in the inversion.

and k trade-off equally in the first iteration and are unresolved in later iterations. For the most part, the data importance vectors (Figure 13) reflect the residual covariances. In the first iteration, the solution is controlled by the travel times and amplitudes of the nearest receivers, while in iterations 2-5, waveforms and travel times to the farther receivers becomes important.

Several attempts were made to incorporate the lower layer parameters into the inversion using the results of iteration 5 as a starting model. However using only receivers from 2-12 km, the lower gradient and depth were poorly resolved and the resulting inversions were unstable. At this point, we extended the synthetic data set by computing waveforms for receivers at 14-20 km. The covariance matrix of the residuals at all receivers was set as $\text{diag}(0.10, 0.10, 0.001)$ and the parameter weighting matrix was $\text{diag}(0.10, 0.10, 0.001, 0.01, 1.0, 1.0)$ for Ψ_∞ , k , upper gradient, top velocity, lower gradient and interface depth, respectively. The discontinuity was constrained to second order.

As shown in Table 4, rather than using the results of iteration 5 as the starting model for iterations 6-10, the results of an earlier inversion were inadvertently used. The model parameters are quite similar, but the weighting scheme of the earlier run resulted in poorer convergence (see RMS fit). Ideally, the starting model should be irrelevant to the final solution, but due to nonlinearity and the parameter weighting designed to stabilize the inversion, this is not entirely the case. The parameter resolution matrices (Figure 12) show that while Ψ_∞ and the lower gradient and depth are well resolved, the upper gradient and k are poorly resolved. The top velocity is resolved, but trades off with the upper gradient. The results for iterations

Test #4 Data Importance Vectors

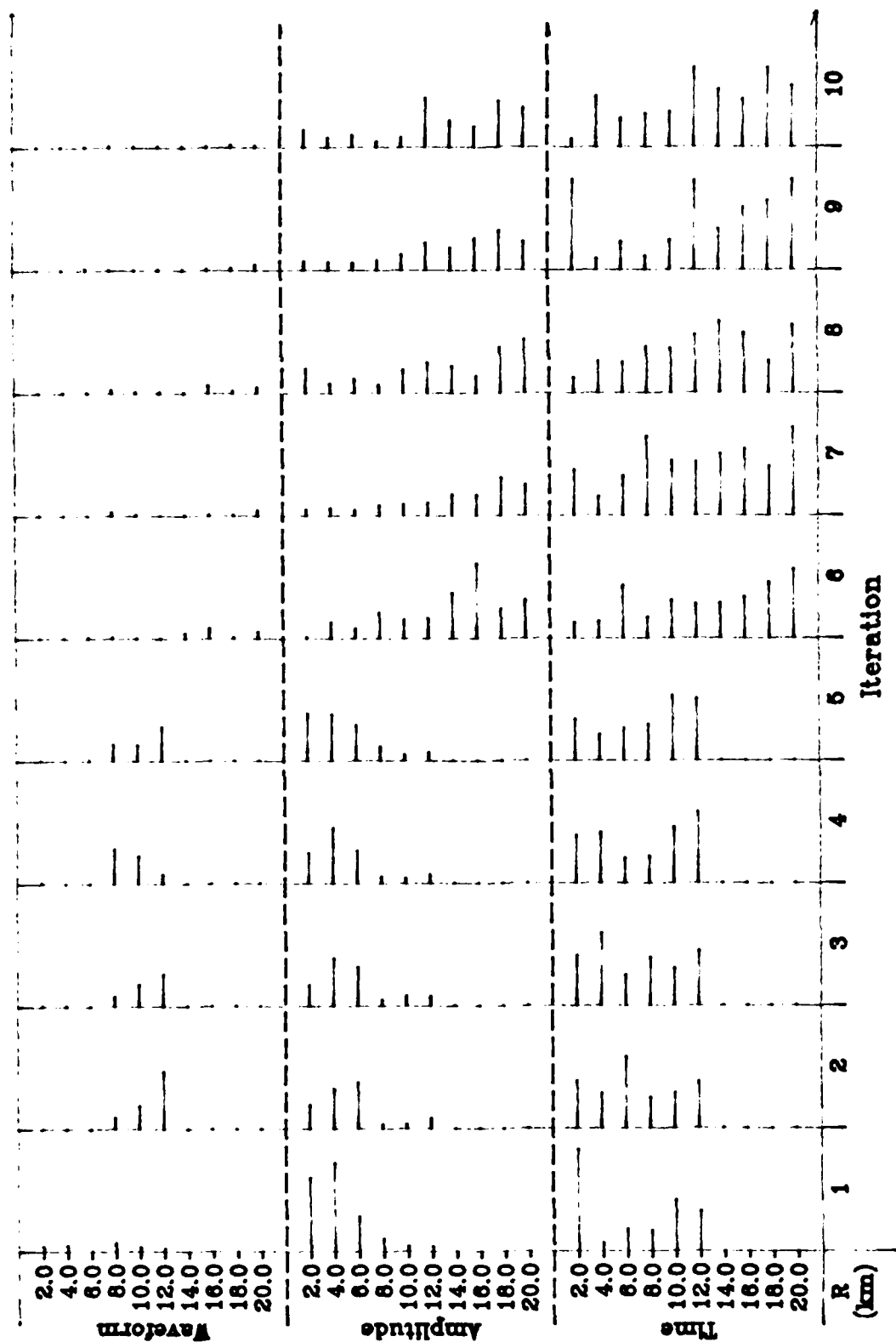


Figure 13. The data importance vectors for each iteration of Test # 4. In the first five iterations, only waveforms from 2-12 km were inverted.

6-10 (Table 4), therefore, indicate that while Ψ_∞ , the lower gradient and the depth approach their correct values (shown at the bottom of the table), the parameters k , upper gradient and top velocity depart slightly, if at all, from the starting model. In the case of the top velocity, this is because the starting model for iteration 6 is quite near the correct value (the correct value was obtained in the first iteration of the inversion). The data importance vectors (Figure 13) show that in iterations 6-10, the travel time and amplitude of the farther receivers are most important in determining the solution, although the travel time at near receivers is important as a constraint. Waveform residuals contribute little to the solution. This may also be seen in the plots of the waveforms (Figure 11), in which the character of the data has been well matched by the fifth iteration, but the travel time and amplitude of farther stations needs refinement.

The results of this test inversion may be summarized by the structure models that are obtained (Figure 14). In this plot of P-wave velocity vs. depth, the model from which the synthetic starting model is shown as the broad dashed line labeled "START". After five iterations, the top velocity and upper gradient have been matched almost exactly (lower structure was not included in these iterations). The RDP parameters reached their best estimates for this parameterization within the first iteration and remained unchanged to iteration five. The starting model for iterations 6-10 was similar to the iteration 5 solution. The lower gradient was assumed to be the same as the upper gradient and the depth to the top of the second layer was assumed as 2 km. The details of the structure between 2 and 3 km could not be resolved with receivers only out to 12 km, so the data set was extended to ranges up to 20 km. In iterations 6-10, the upper layer parameters remained

Test # 4 Inversion Structure Models

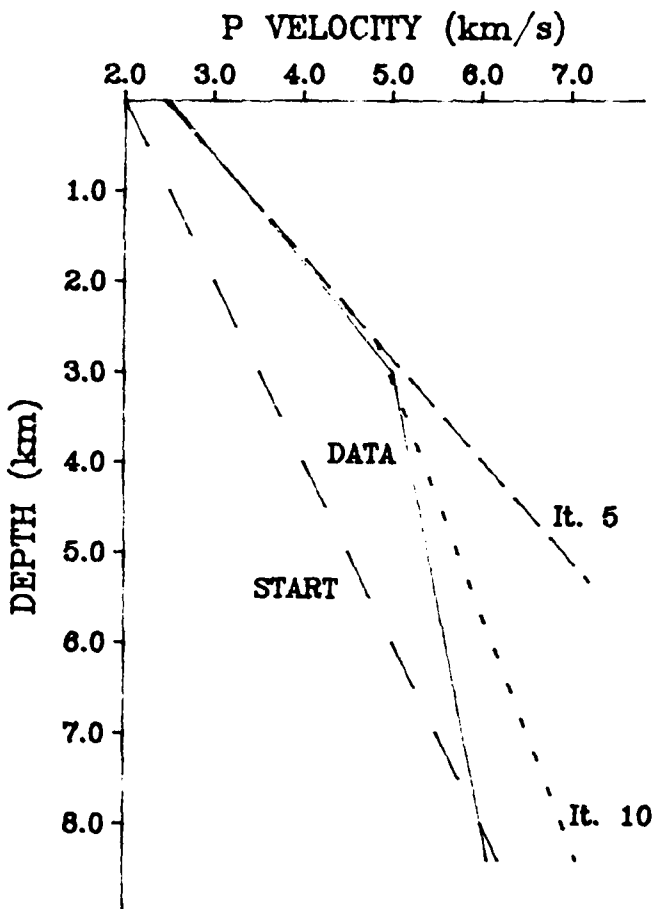


Figure 14. Velocity structure models from Test # 4. The synthetic "data" set was computed for the two-gradient model plotted as a solid line. The starting model consisted of a single gradient shown as the long dashed line. In the first five iterations, a single gradient was considered, and the resulting model is denoted "It. 5". It matches the upper gradient of the "data" model quite well. Finally, a two-gradient model was obtained after iteration 10 (short dashed line) which approaches the lower "data" gradient.

essentially unchanged, the depth increased toward the correct value of 3.0 km and the lower gradient decreased toward the correct value. The source parameters adjusted mostly in the sixth and seventh iterations, then remained stable through the remaining iterations.

INVERSIONS FOR PAHUTE MESA EVENTS

BOXCAR

We begin the inversions of actual data with the Pahute Mesa event, BOXCAR (4/26/68, 1300 kT announced). Hartzell, et al. (1983) developed their Pahute Mesa structure model primarily by modeling the waveforms of receivers S-2⁴ and S-3⁴ from BOXCAR, although travel times from several other events were quite well predicted. We will use an approximation of the Hartzell, et al. (1983) model (the "data" model from test # 4) as our starting model and invert directly for a two-layer model with a second order discontinuity. The stations used in the inversion are listed in Table 5, and include a broad distribution of ranges. The closest receivers (S-12 at 3.81 km and S-16 at 4.87 km) are only marginally outside the spall zone and appear to include arrivals attributable to spall opening or slap-down. Since these effects will not be included in our modeling, we must increase the covariance of the waveform residuals, effectively downweighting the importance of fitting the waveform, at these receivers. The covariance matrix is diag(1.00, 0.01, 0.001) for waveform, amplitude and travel time, respectively. Similarly, the farthest station (S-7⁴ at 22.47 km) is located outside the Silent Canyon Caldera of Pahute Mesa, and we could expect the plane-layered structure

Table 5 - Pahute Mesa Station Parameters

Station	Range (km)	Window Start* (sec)	Window End* (sec)
<u>BOXCAR</u>			
S-12	3.81	1.25	2.05
S-16	4.87	1.55	2.35
S-24	7.27	1.85	3.20
S-34	10.37	2.70	3.95
S-74	22.47	4.50	6.00
<u>INLET</u>			
S-5	1.63	0.40	1.25
S-6	3.27	0.90	1.75
S-7	6.53	1.85	2.70
<u>MAST</u>			
S-5	3.65	1.00	1.90
S-6	5.47	1.40	2.35
S-7	7.30	1.85	2.80
<u>SCOTCH</u>			
S-3A	4.13	1.20	2.00 **
S-4	6.06	1.75	2.30 ***
			2.70

* Time after origin.

** End time for iterations 1-5.

*** End time for iterations 6-15.

approximation to break down for this receiver. We have therefore increased the covariance of the waveform and travel-time residuals at this receiver. The resulting covariance is $\text{diag}(0.10, 0.01, 0.10)$. This leaves two receivers (S-24 at 7.27 km and S-34 at 10.37 km) with reasonable covariance in all three residuals. The covariance for these receivers is $\text{diag}(0.01, 0.01, 0.001)$. After many test inversions, the parameter weighting scheme that allowed a

stable solution was found to be $\text{diag}(0.10, 0.10, 0.001, 0.01, 0.01, 0.10)$ for Ψ_∞ , k , upper gradient, top velocity, lower gradient and interface depth, respectively. Five iterations were allowed, truncating one eigenvalue in each iteration.

The inversion results are listed in Table 6 and the waveforms are displayed in Figure 15. The synthetic waveforms for the nearest receivers are simple and impulsive, while the observed waveforms are broad, and include significant late arrivals. Since the travel-time residual is defined as the peak in cross-correlation with the time window denoted by arrows in Figure 15, the minimum of the residual corresponds to the alignment of peaks and not necessarily the alignment of first breaks. This error due to unmodeled arrivals, combined with delays due to differing receiver structure (considered noise) accounts for the 0.17 sec travel-time error at the 7 km station. We expect, and have allowed, larger travel-time errors at the farthest receiver, although the final synthetic is only 0.31 sec late. Although the numbers to the right of the waveforms in Figure 15 are the maxima of the trace absolute values and not the first peak amplitudes, we see that the final synthetic first peak amplitudes are in reasonable agreement with the observations at all but the nearest receivers. Details of the waveforms of the farther three receivers are quite well modeled, even to a certain extent outside the time window of the inversion. The first peak at the 7 and 10 km stations includes the constructive interference of upgoing and diving rays, while the first trough includes the interaction of the surface reflection phases. The waveform at the farthest station changes significantly through the iterations in an attempt to fit the double first peak and the gradually rising trough. Although time shifted, the synthetic from the fifth iteration provides a

Table 6 - BOXCAR Inversion Results

Iteration	Ψ_∞ ($\times 10^{10} \text{ cm}^3$)	k (s^{-1})	$\nabla \alpha_1$ (km/s/km)	α_1 (km/s)	$\nabla \alpha_2$ (km/s/km)	Z_2 (km)	RMS fit
Start	12.00	6.50	0.83	2.50	0.20	3.00	0.2965
1	12.52 (0.20)	7.96 (0.69)	0.93 (0.30)	2.47 (0.16)	0.11 (0.12)	3.26 (0.28)	0.1919
2	12.46 (0.14)	7.33 (0.49)	0.77 (0.23)	2.76 (0.32)	0.13 (0.04)	3.15 (0.40)	0.1999
3	12.56 (0.15)	7.51 (0.43)	0.85 (0.44)	2.47 (0.21)	0.12 (0.07)	3.18 (0.72)	0.2313
4	12.78 (0.20)	8.06 (0.51)	0.88 (0.11)	2.43 (0.16)	0.15 (0.04)	3.22 (0.27)	0.2615
5	12.63 (0.14)	7.62 (0.42)	0.88 (0.24)	2.47 (0.17)	0.16 (0.05)	3.60 (0.60)	0.1801

-- Numbers in parentheses are the standard deviations of the parameter changes that result in the model parameters for that iteration.

reasonable fit to these features.

Table 6 includes, in parentheses, the standard deviations of the parameter changes for each iteration. As discussed previously, these are not the standard deviations of the parameters themselves, and could only be interpreted so if the starting model of the iteration was, in some sense, error free. This error measure also includes the effects of parameter and residual weighting for stabilizing the non-linear inversion. While the standard deviations seem to reflect mostly the sizes of the parameter changes in a given iteration, they indicate at least the level of confidence that may

BOXCAR Inversion Results

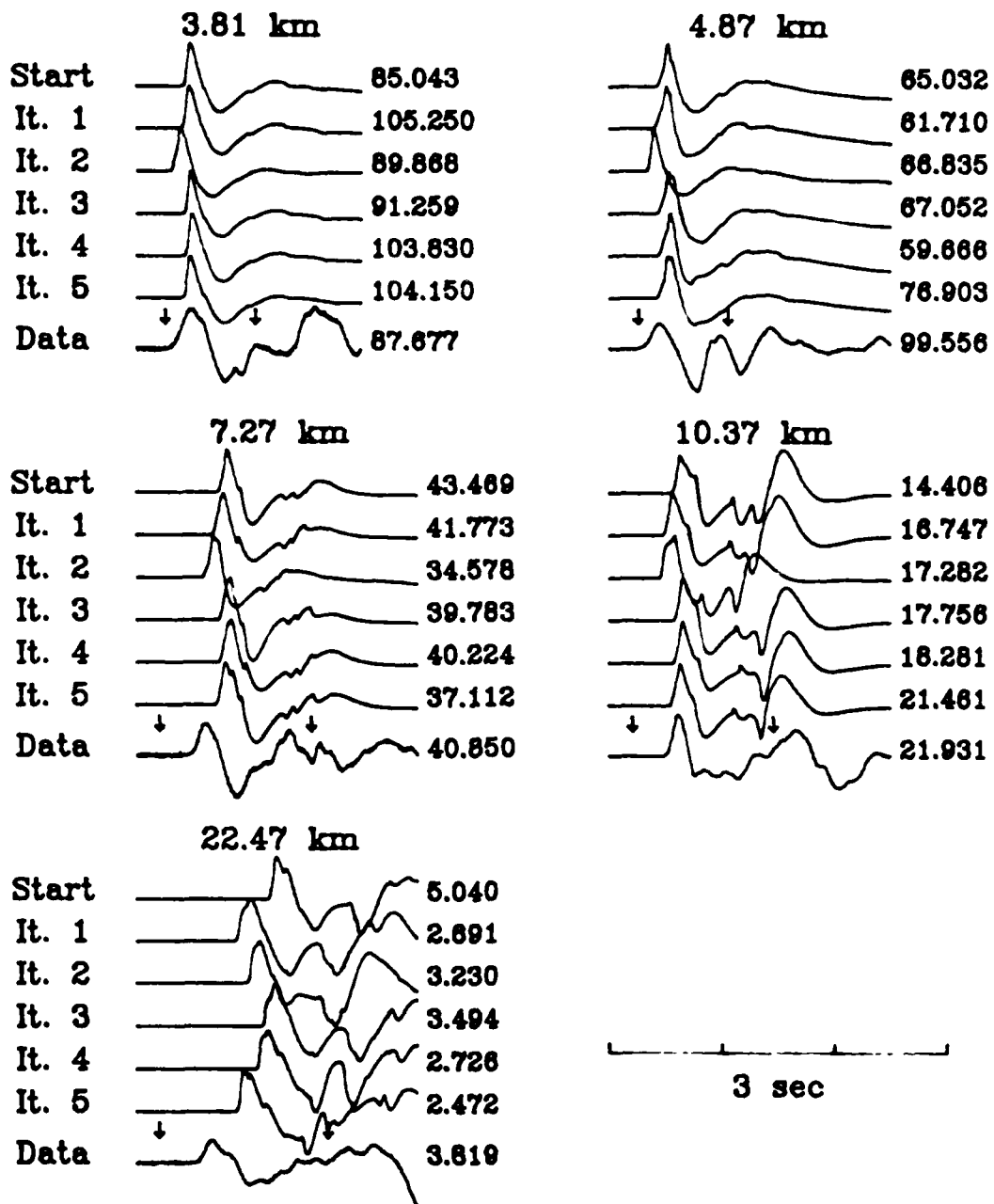


Figure 15. Inversion results for the Pahute Mesa event, BOXCAR. Shown are synthetic seismograms for the starting model and each iteration (above) compared with the observed waveforms (below). The peak trace amplitude is shown to the right and the inversion time window is denoted by arrows. The time scale is shown on the bottom right.

be placed on a particular parameter obtained in the inversion. The parameter resolution matrices for the BOXCAR inversions are plotted in Figure 16. The structure parameters are perfectly resolved through all iterations. Ψ_∞ and k trade off, with k being somewhat better resolved. The data importance vectors (Figure 17) reflect primarily the residual weighting scheme discussed above, but indicate that waveforms at farther stations, travel times to the nearest stations and amplitudes at all stations influence the solution.

The final structure model for BOXCAR is not significantly different than the two-gradient starting model based on the model of Hartzell, et al. (1983). Both Ψ_∞ and k , however, are significantly larger than the starting model values, which were based on the values obtained by Barker, et al. (1985) using the Hartzell, et al. (1983) model. In addition, the RMS fit has been significantly improved over the starting model, even in the presence of noise and unmodeled arrivals. An inversion of the BOXCAR data set, in which the depth of the water table was fixed as a layer interface, and the shallow structure model of Leonard and Johnson (1986) was used as the starting model, resulted in an intermediate layer with vanishing thickness, and relatively poor waveform fits. This indicates that the details of structure above the source are difficult to resolve uniquely from waveforms located outside the spall zone.

BOXCAR Resolution Matrices

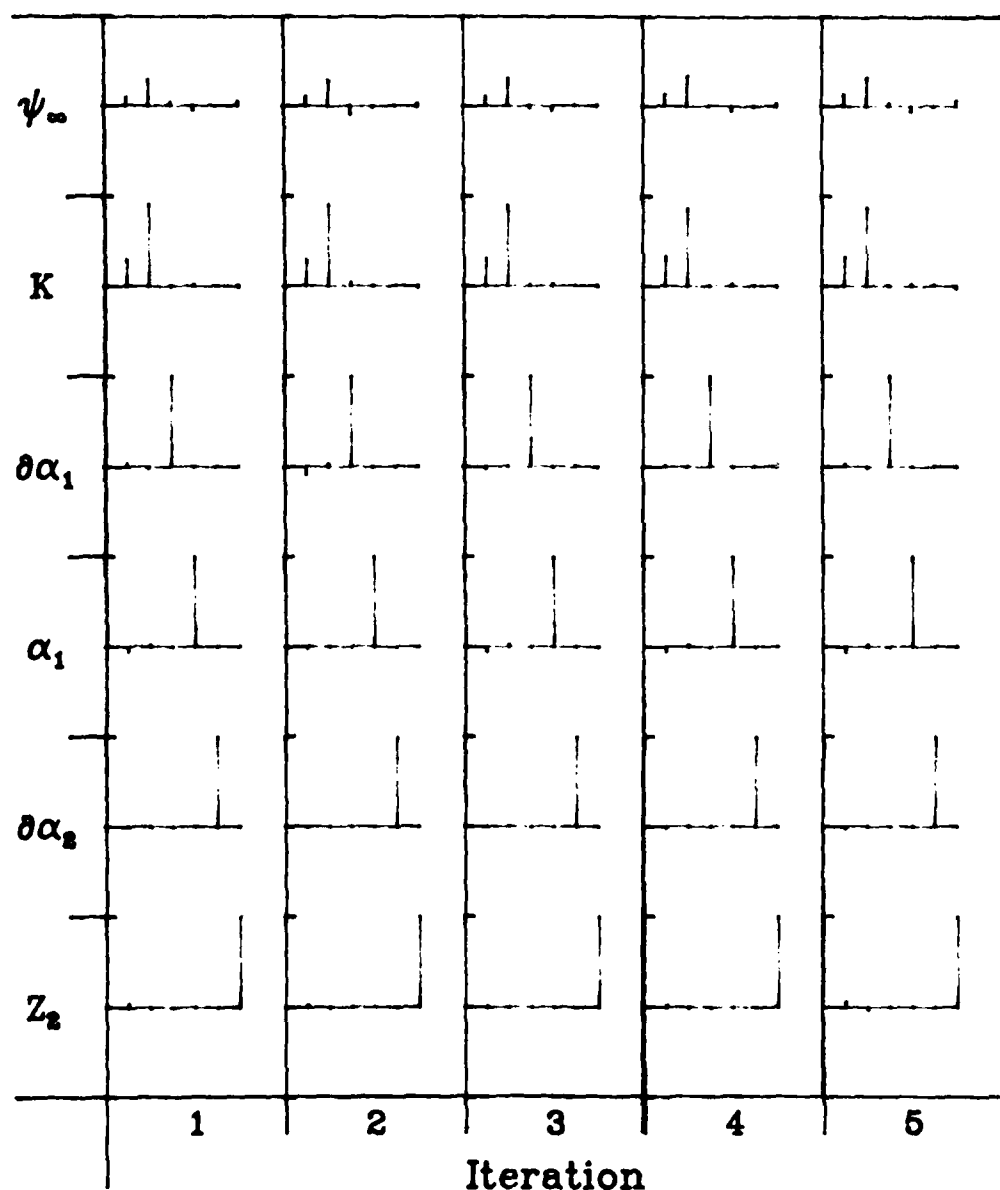


Figure 16. Parameter resolution matrices for each iteration of the BOXCAR inversion. Plotted from top to bottom are the rows of the matrices corresponding to the source parameters, ψ_∞ and k , and the structure parameters, upper gradient, top velocity, lower gradient and interface depth. For perfect resolution, the resolution matrix would be the identity matrix.

BOXCAR Data Importance Vectors

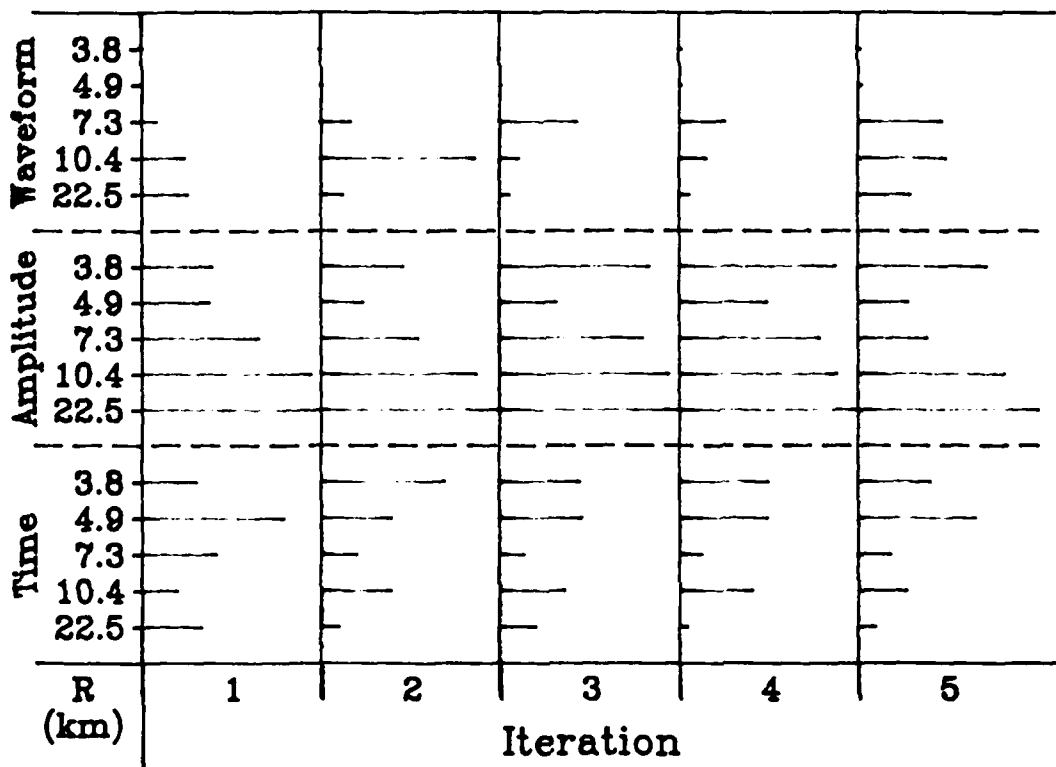


Figure 17. Data importance vectors for each iteration of the BOXCAR inversion. The length of the ticks indicate the relative importance of each residual in determining the solution.

INLET

Since we have little a priori information on a structure model specific to the Pahute Mesa event INLET (11/20/75, 500 kT estimated), the inversion procedure will follow the approach outlined in Test # 4. For the first five iterations, we solve for source and upper gradient parameters. Using these results as a starting model, we invert for source and a two-layered gradient model with a second-order discontinuity. The data consist of vertical velocity waveforms from the three receivers listed in Table 5. In the first five iterations, we hope to fit primarily travel time, so the covariance matrix of the residuals is defined as $\text{diag}(1.0, 1.0, 0.001)$ for waveform, amplitude and travel time residuals at S-5 and S-6, respectively, and $\text{diag}(0.1, 0.1, 0.001)$ for the same residuals at S-7. The parameter weights are defined as $\text{diag}(0.1, 1.0, 0.01, 1.0)$ for Ψ_∞ , k , upper gradient and top velocity, respectively. In iterations 6-15, the covariance matrix of the residuals is $\text{diag}(0.01, 0.1, 0.001)$ for S-5 and S-6 and $\text{diag}(0.1, 0.1, 0.01)$ for S-7. The parameter weights are $\text{diag}(0.1, 0.1, 0.01, 0.01, 1.0, 0.1)$, where the last two correspond to lower gradient and interface depth, respectively.

The results of the inversion are listed in Table 7, the waveforms are plotted in Figure 18, the parameter resolution matrices are shown in Figure 19 and the data importance vectors are plotted in Figure 20. As planned, the first five iterations are controlled by the travel-time residuals (Figure 20) as well as the amplitude residual at S-7. The upper gradient parameters are perfectly resolved (Figure 19), k is fairly well resolved, but Ψ_∞ trades off with k and the upper gradient. The waveforms (Figure 18) change little in the first five iterations, except that later arriving features are beginning to

Table 7 - INLET Inversion Results

Iteration	Ψ_∞ ($\times 10^{10} \text{ cm}^3$)	k (s^{-1})	$\nabla \alpha_1$ (km/s/km)	α_1 (km/s)	$\nabla \alpha_2$ (km/s/km)	z_2 (km)	RMS fit
Start	3.20	8.00	0.83	2.50	-	-	0.2733
1	3.24 (0.15)	4.91 (1.49)	1.21 (0.42)	2.64 (0.08)	-	-	0.4206
2	3.34 (0.08)	8.08 (1.50)	1.42 (0.59)	2.35 (0.24)	-	-	0.1895
3	3.56 (0.44)	9.60 (1.65)	1.41 (0.42)	2.41 (0.15)	-	-	0.1407
4	3.61 (0.56)	9.78 (1.32)	1.42 (0.49)	2.36 (0.14)	-	-	0.1511
5	3.61 (0.52)	9.70 (1.21)	1.43 (0.52)	2.37 (0.16)	[0.30]	[2.50]	0.1675
6	4.75 (1.09)	6.76 (1.55)	1.17 (0.56)	2.61 (0.39)	1.98 (0.71)	3.58 (0.80)	0.1781
7	5.13 (0.69)	7.12 (0.94)	1.30 (0.43)	2.52 (0.33)	2.40 (0.52)	3.47 (0.29)	0.1521
8	5.95 (1.70)	6.20 (1.91)	1.37 (0.51)	2.58 (0.45)	3.07 (0.73)	2.37 (2.13)	0.1269
9	6.25 (0.83)	6.33 (0.86)	1.34 (0.82)	2.60 (0.36)	2.91 (0.33)	3.22 (2.13)	0.1491
10	6.25 (0.39)	6.12 (1.00)	1.51 (0.44)	2.58 (0.27)	3.12 (0.48)	3.06 (0.60)	0.1369
11	6.30 (0.61)	6.21 (1.08)	1.47 (0.77)	2.59 (0.65)	3.13 (0.48)	3.06 (0.03)	0.1392
12	6.57 (0.56)	6.64 (0.95)	1.27 (0.74)	2.58 (0.42)	3.31 (0.16)	3.18 (0.52)	0.1288
13	6.47 (0.52)	6.38 (0.94)	1.42 (0.54)	2.54 (0.42)	3.30 (0.04)	3.14 (0.10)	0.1480
14	6.54 (0.60)	6.23 (1.13)	1.57 (0.74)	2.50 (0.46)	3.27 (0.09)	3.19 (0.23)	0.1605
15	6.80 (0.85)	6.65 (1.39)	1.55 (0.69)	2.48 (0.38)	3.25 (0.13)	3.28 (0.50)	0.1533

-- Numbers in parentheses are the standard deviations of the parameter changes that result in the model parameters for that iteration.

-- Numbers in square brackets are starting values for iterations 6-15, not results of iteration 5.

INLET Inversion Results

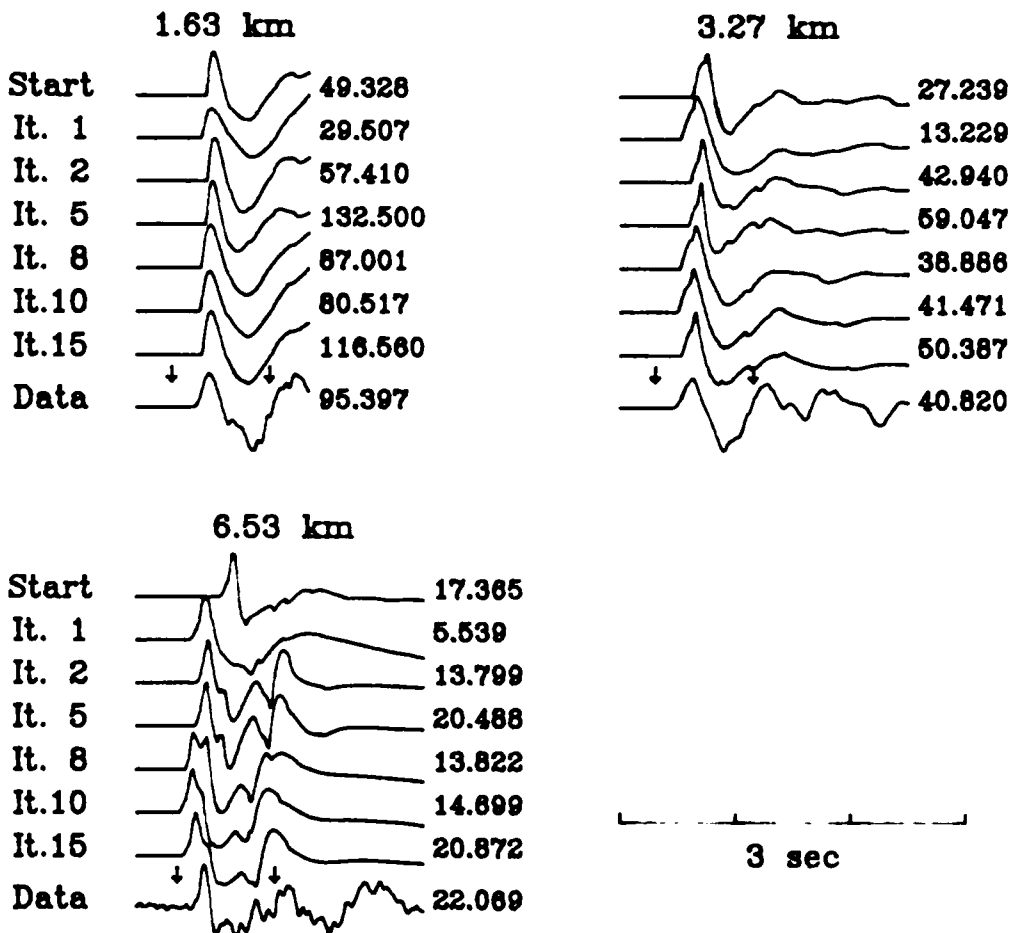


Figure 18. Inversion results for INLET. Shown are synthetic seismograms for the starting model and selected iterations (above) compared with the observed waveforms (below). The format is the same as Figure 15.

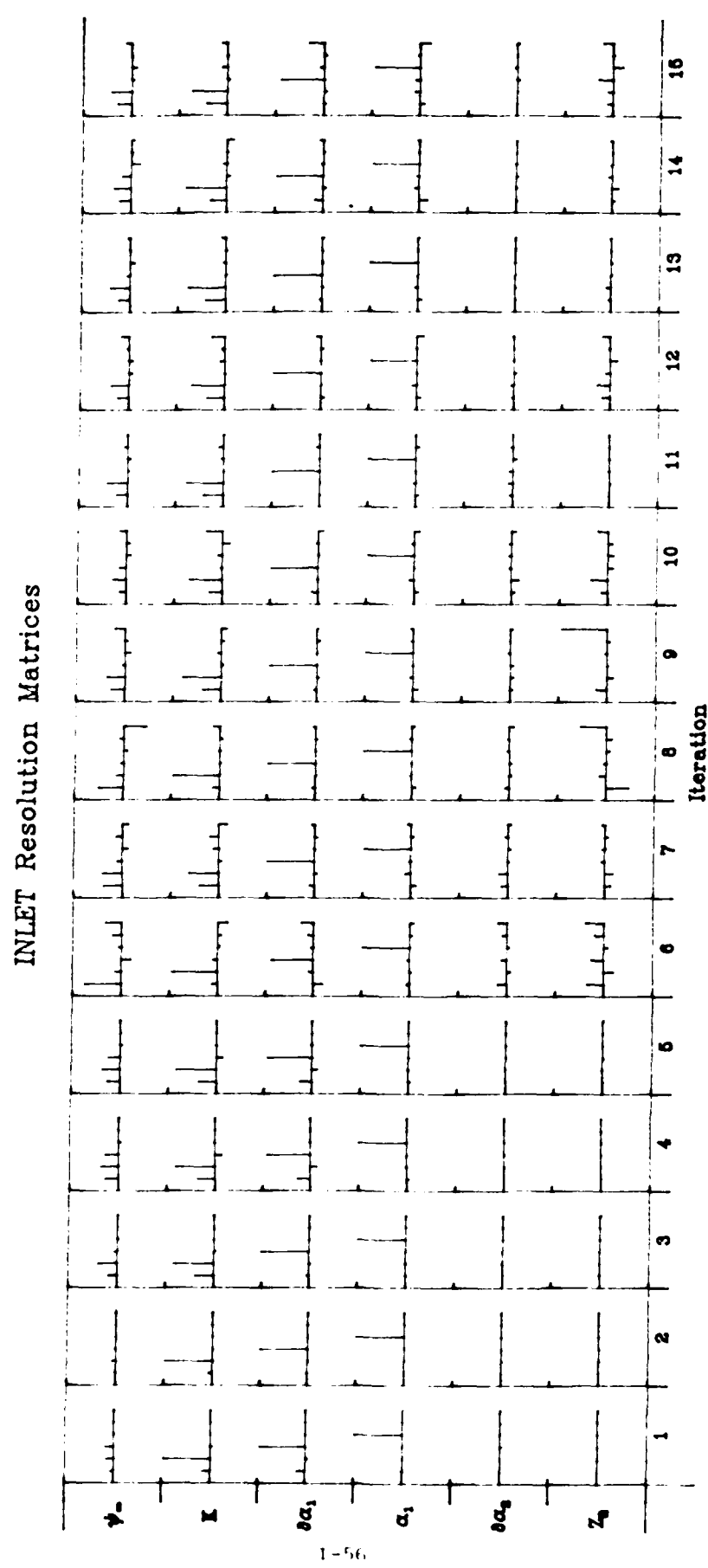
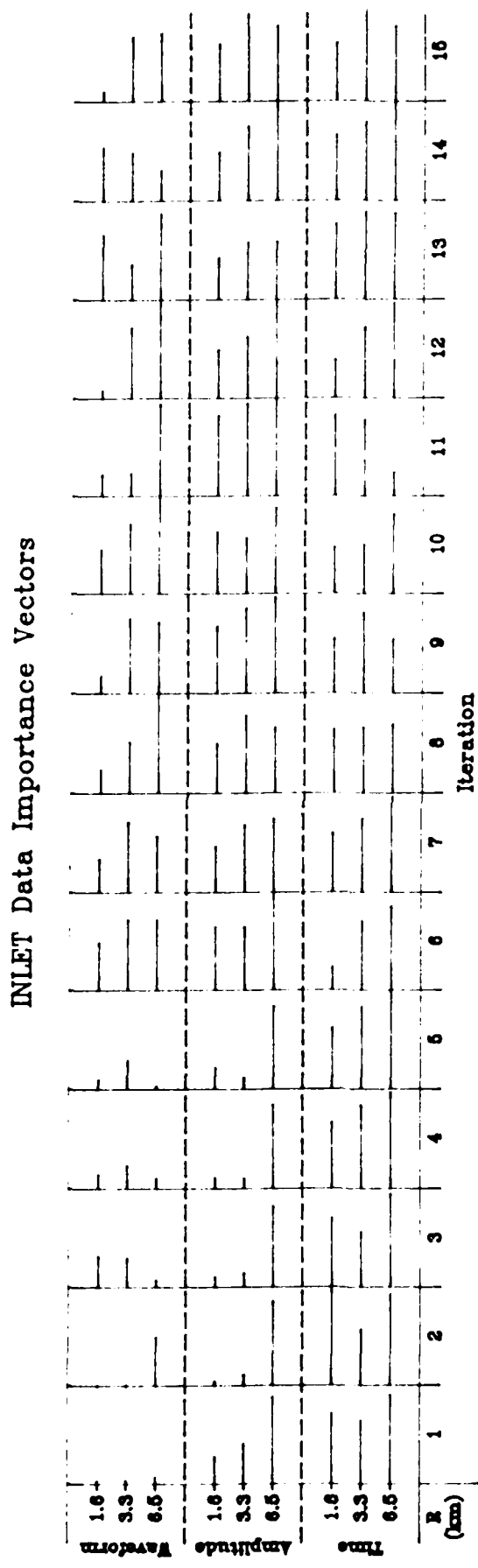


Figure 19. The parameter resolution matrices for each iteration of the inversion of INLET waveforms. Lower gradient parameters were not considered in the first five iterations.



I-57

Figure 20. The data importance vectors for each iteration of the TWET waveform inversion.

arise at S-7. The standard deviations of the parameter changes (Table 7) indicate that Ψ_∞ is not significantly changed. The decrease in top velocity and increase in upper gradient may indicate that near-surface, high-gradient structure that is not included in the current parameterization is affecting the results. At any rate, a significant improvement in RMS fit is achieved in the first five iterations. In iterations 6-15, upper gradient parameters are, once again, well resolved (Figure 19), Ψ_∞ trades off with k , and the lower structure parameters are relatively poorly resolved. All of the residuals contribute essentially equally to the solution (Figure 20), although the importance of the relatively simple waveform at S-5 is somewhat diminished. Features of the synthetic waveforms at S-5 and S-6 do not change significantly in the later iterations, but fit the observations reasonably well within the inversion time window (Figure 18). At S-7, the rise to the first peak is well modeled, although constructive interference of a second arrival broadens the first peak of the synthetic beyond that observed. The interference of several arrivals causes the trough to be smoothed into a broad, slowly rising feature, as observed in the data.

The poor resolution of the lower layer parameters, the erratic convergence when these parameters are added to the inversion, and the final values obtained for these parameters indicate either that the three observed waveforms are incapable of resolving structure beneath about 2.5 km, or that the constraint of a second-order discontinuity is too severe. At any rate, it is unlikely that an increasing gradient below 3 km is uniquely resolved by this data set. The results of iteration 5 indicate that the single gradient model results in source parameter estimates slightly higher than those of Barker, et al. (1985), which were used as starting values. On the other hand,

the two-layer model results in an estimate of Ψ_∞ about double that of Barker, et al. (1985), while the k estimate is somewhat decreased. Future inversions with this data set will free the discontinuity between layers to be first order in order to determine whether the rise time and amplitude of the first peak are affected by more reasonable structures at depth.

MAST

The procedure for the inversion of waveforms from the Pahute Mesa event MAST (6/19/75, 520 kT estimated) is similar to that for INLET. The receivers to be included are listed in Table 5, and the covariance matrix for the first five iterations is defined as $\text{diag}(0.01, 0.01, 0.01)$ for the waveform, amplitude and travel time residuals of the three stations, respectively. The parameter weighting matrix is $\text{diag}(0.1, 1.0, 0.01, 1.0)$ for Ψ_∞ , k , upper gradient and top velocity, respectively. For iterations 6-15, the residual covariance matrix is $\text{diag}(0.01, 0.1, 0.001)$ for S-5 and S-6 and $\text{diag}(0.01, 0.01, 0.01)$ for S-7. The parameter weighting matrix becomes $\text{diag}(0.1, 0.1, 0.01, 0.01, 0.1, 0.1)$, where the last two correspond to lower gradient and interface depth, respectively.

The results of the inversion are listed in Table 8, and the waveforms, parameter resolution matrices and data importance vectors are plotted in Figures 21-23, respectively. As with INLET, the upper structure parameters are well resolved, lower structure parameters are poorly resolved, and Ψ_∞ and k trade off with k slightly better resolved. The interface depth is actually better resolved than with INLET, but the effect is to lower the interface to a point at which the available waveforms are unlikely to resolve the structure

Table 8 - MAST Inversion Results

Iteration	Ψ_∞ ($\times 10^{10} \text{ cm}^3$)	k (s^{-1})	$\nabla \alpha_1$ (km/s/km)	α_1 (km/s)	$\nabla \alpha_2$ (km/s/km)	Z_2 (km)	RMS fit
Start	4.70	7.50	0.83	2.50	-	-	0.2646
1	4.63 (0.04)	6.62 (0.25)	0.77 (0.16)	3.08 (0.08)	-	-	0.2052
2	4.75 (0.05)	8.19 (0.42)	0.77 (0.14)	2.88 (0.14)	-	-	0.1813
3	4.62 (0.06)	7.02 (0.31)	0.90 (0.17)	2.87 (0.10)	-	-	0.1679
4	4.67 (0.04)	7.15 (0.36)	0.98 (0.19)	2.90 (0.11)	-	-	0.1615
5	4.66 (0.06)	7.02 (0.37)	1.12 (0.25)	2.91 (0.13)	[0.20]	[2.00]	0.1603
6	4.69 (0.20)	5.89 (1.19)	1.02 (0.44)	3.07 (0.58)	0.35 (0.34)	2.64 (0.41)	0.2197
7	5.01 (0.57)	6.58 (1.48)	0.99 (0.79)	2.96 (0.85)	0.35 (0.32)	2.75 (0.61)	0.1565
8	5.03 (0.31)	6.60 (0.52)	0.99 (0.19)	2.95 (0.18)	0.35 (0.01)	2.77 (0.59)	0.1347
9	4.95 (0.15)	6.34 (0.45)	1.09 (0.20)	2.95 (0.18)	0.39 (0.05)	2.79 (0.18)	0.1691
10	5.10 (0.24)	6.36 (0.46)	1.12 (0.33)	2.93 (0.16)	0.42 (0.05)	3.21 (0.88)	0.1527
11	5.18 (0.65)	5.81 (1.46)	1.18 (0.30)	2.91 (0.29)	0.55 (0.51)	3.63 (1.76)	0.2067
12	5.33 (0.27)	5.94 (0.44)	1.26 (0.27)	2.80 (0.38)	0.56 (0.01)	3.62 (0.01)	0.1624
13	5.78 (0.60)	5.81 (0.67)	1.36 (0.44)	2.80 (0.28)	0.63 (0.11)	4.44 (1.31)	0.1517
14	6.00 (0.42)	6.02 (0.47)	1.25 (0.53)	2.89 (0.52)	0.63 (0.01)	4.35 (0.23)	0.1213
15	6.41 (0.96)	5.80 (0.43)	1.48 (0.84)	2.70 (0.59)	0.60 (0.06)	4.51 (0.26)	0.1074

-- Numbers in parentheses are the standard deviations of the parameter changes that result in the model parameters for that iteration.

-- Numbers in square brackets are starting values for iterations 6-15, not results of iteration 5.

MAST Inversion Results

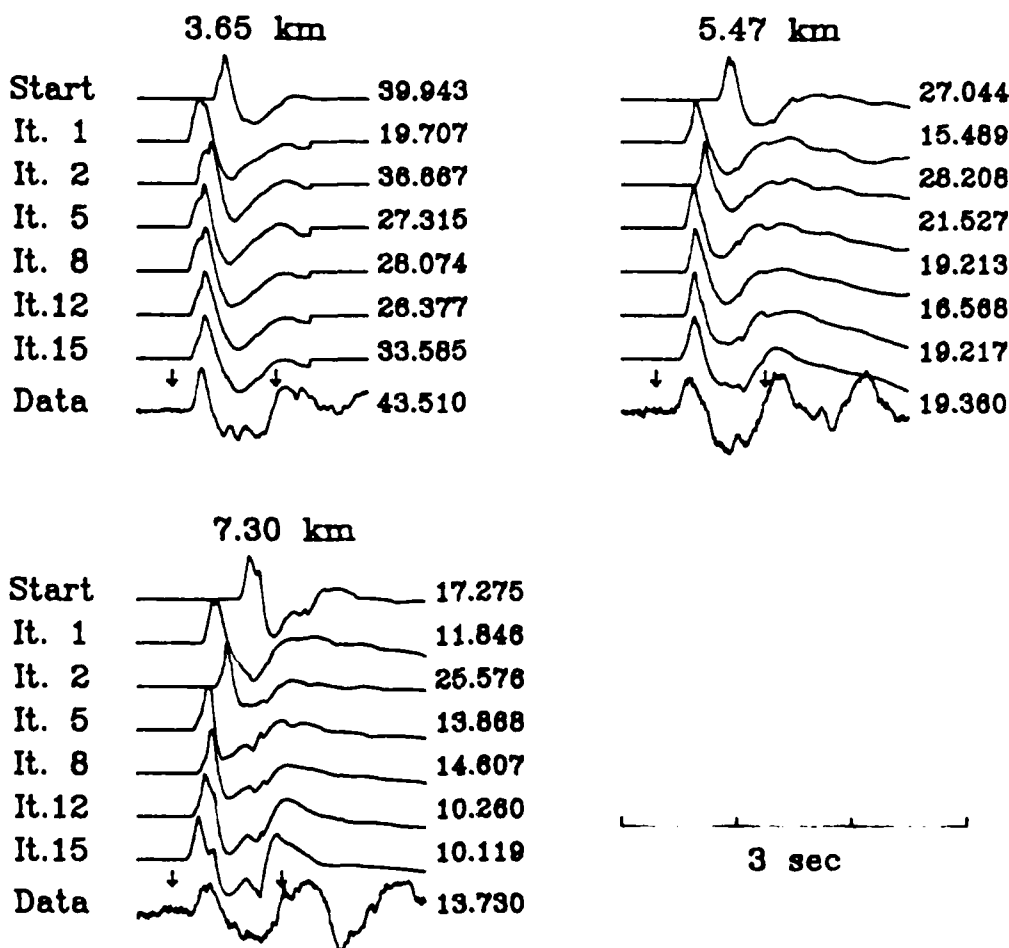
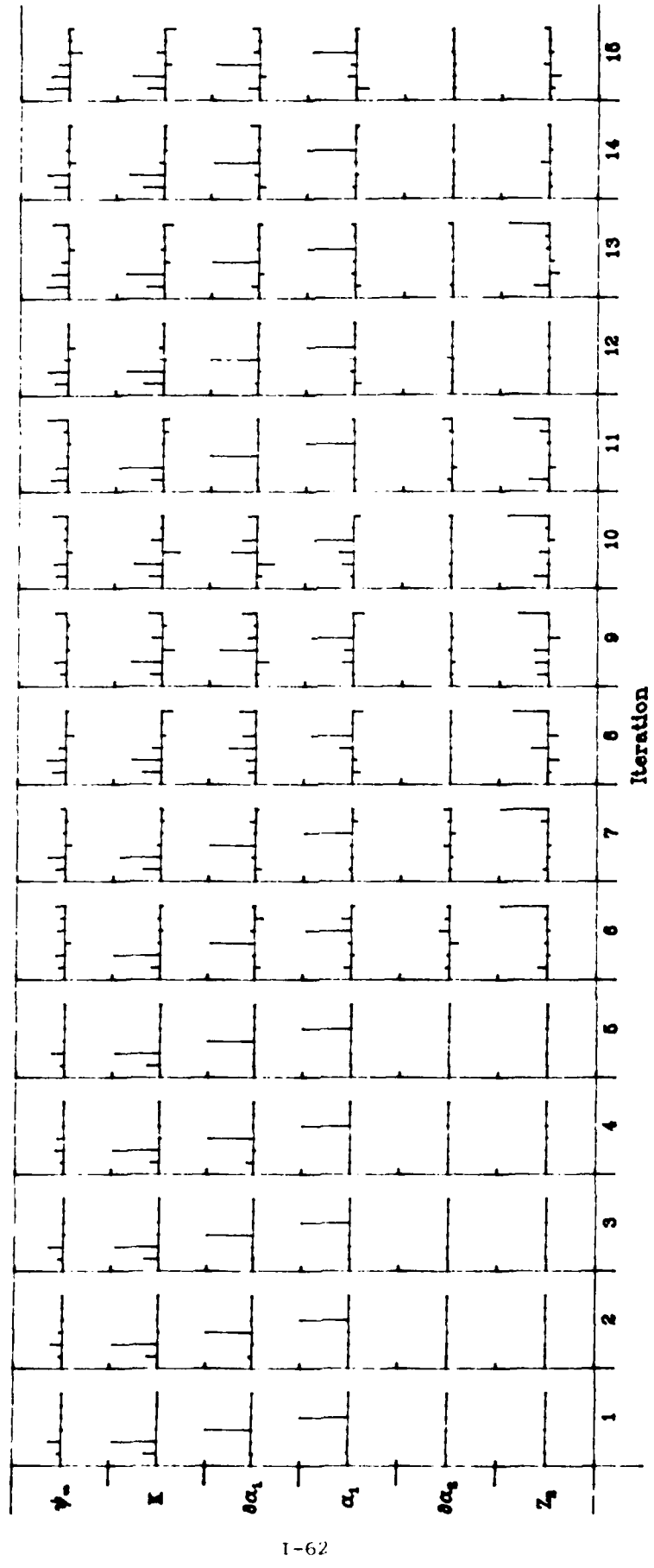


Figure 21. Inversion results for MAST. Shown are synthetic seismograms for the starting model and selected iterations (above) compared with the observed waveforms (below). The format is the same as Figure 15.

MAST Resolution Matrices



1-62

Figure 22. The parameter resolution matrices for each iteration of the inversion of MAST waveforms.
Lower gradient parameters were not considered in the first five iterations.

MAST Data Importance Vectors

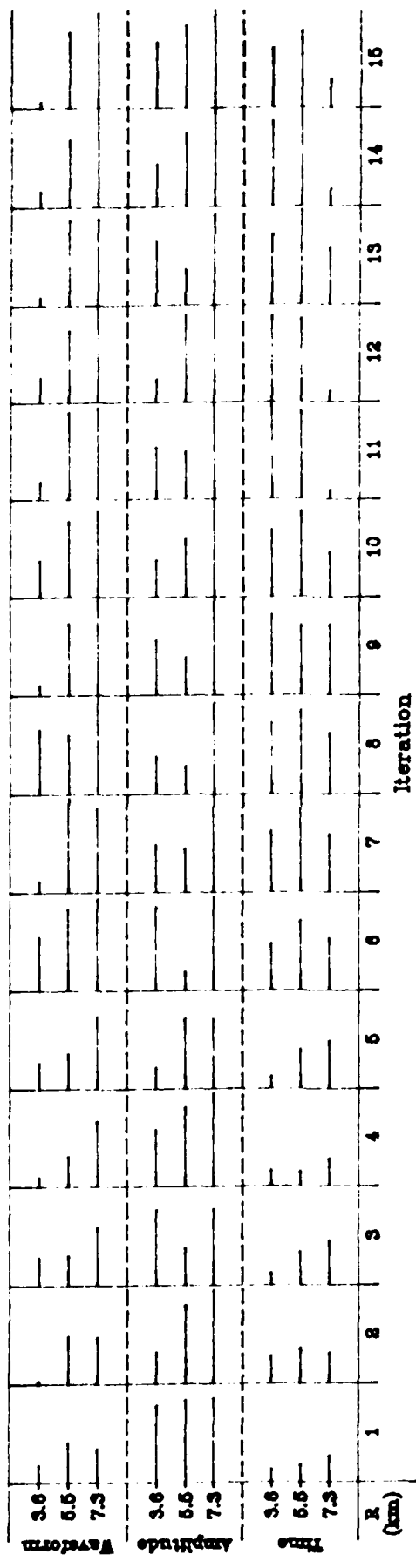


Figure 23. The data importance vectors for each iteration of the MAST waveform inversion.

beneath it (see Table 8). Also unlike INLET, the lower gradient remains smaller than the upper gradient, suggesting no need for a first-order discontinuity at depth. Except for the improvement in RMS fit in the last iteration, a single gradient model would appear as reasonable as the two-layer model. The last iteration yields improved fits to the amplitudes of the first peaks (Figure 21), begins to account for the double arrival in the first peak at S-7, and includes multiple interference features in the first trough at S-6 and S-7. The data importance vectors (Figure 23) suggest that the simple waveform at S-5 is relatively unimportant to the solution. The importance of the other residuals follows the weighting scheme.

If we consider that the single gradient model is sufficient, the results of iteration 5 (Table 8) indicate that there is no significant change in Ψ_∞ from the value obtained by Barker, et al. (1985) (the starting model). The value obtained for k is slightly decreased. Once again, the upper gradient is increased and the top velocity is decreased relative to the Hartzell, et al. (1983) model, although this could be an effect of ignoring near-surface, high-gradient structure. With the inclusion of the lower layer (whether actually resolved or not), the estimate of Ψ_∞ is increased, that of k is decreased, and the value of the upper gradient is further increased. The top velocity is not changed significantly from the starting model.

SCOTCH

For the inversion of the Pahute Mesa event SCOTCH (5/23/67, 155 kT announced), there are only two local observations outside the spall zone (see Table 5). Once again, following the procedure outlined above, we invert first for source and upper structure parameters, setting the parameter weighting matrix to be $\text{diag}(0.1, 1.0, 0.01, 1.0)$ for Ψ_∞ , k , upper gradient and top velocity, respectively. The covariance matrix for both receivers is $\text{diag}(0.01, 0.01, 0.01)$ for waveform, amplitude and travel-time residuals, respectively. For iterations 6-15, we include the parameters of the lower layer, and define the weighting matrix as $\text{diag}(0.1, 1.0, 0.01, 0.01, 1.0, 0.1)$, where the last two correspond to lower gradient and interface depth, respectively. The residual covariance matrix is adjusted to $\text{diag}(0.01, 0.1, 0.001)$ for both receivers.

The inversion results are listed in Table 9 and the waveforms, parameter resolution matrices and data importance vectors are plotted in Figures 24-26. The parameter resolution matrix (Figure 25) indicates that, as before, the top velocity is perfectly resolved throughout the inversion. The upper gradient is well resolved except in iterations 3-5, in which it is hardly resolved at all. As usual, Ψ_∞ and k trade off, this time about equally. The lower structure parameters are somewhat poorly resolved, although in a few iterations, the interface depth is resolved. Since there are only two receivers, each of the residuals is equally important in defining the solution (Figure 26).

Within the first two or three iterations, the upper gradient and top velocity have essentially reached their final values (see Table 9). These parameters are well resolved by the data. By the fifth iteration, a strong pP

Table 9 - SCOTCH Inversion Results

Iteration	Ψ_∞ ($\times 10^{10} \text{ cm}^3$)	k (s^{-1})	$\nabla \alpha_1$ (km/s/km)	α_1 (km/s)	$\nabla \alpha_2$ (km/s/km)	Z_2 (km)	RMS fit
Start	1.30	12.00	0.83	2.50	-	-	0.2624
1	1.45 (0.22)	10.85 (0.84)	1.22 (0.39)	2.35 (0.14)	-	-	0.2412
2	2.22 (0.25)	12.40 (0.28)	1.76 (0.45)	2.01 (0.17)	-	-	0.1849
3	2.22 (0.19)	12.40 (0.26)	1.75 (0.02)	1.83 (0.08)	-	-	0.1592
4	2.23 (0.18)	12.44 (0.28)	1.75 (0.05)	1.84 (0.06)	-	-	0.1601
5	2.24 (0.15)	12.45 (0.25)	1.75 (0.05)	1.81 (0.06)	[0.20]	[2.00]	0.1794
6	1.76 (0.68)	11.46 (0.86)	1.56 (0.23)	2.01 (0.18)	2.21 (0.64)	2.48 (0.49)	0.2707*
7	1.67 (0.42)	11.79 (0.71)	1.89 (0.35)	1.92 (0.37)	3.94 (0.66)	2.03 (0.41)	0.2365
8	1.63 (0.45)	11.46 (1.19)	1.85 (0.52)	1.94 (0.28)	3.91 (0.16)	2.37 (0.27)	0.2581
9	2.47 (0.84)	13.60 (0.97)	1.97 (0.44)	1.81 (0.25)	3.85 (0.14)	2.53 (0.18)	0.3326
10	2.68 (0.69)	11.85 (0.75)	1.84 (0.29)	1.84 (0.34)	6.74 (1.97)	3.22 (0.64)	0.1692
11	2.52 (0.62)	12.63 (0.68)	1.83 (0.47)	1.88 (0.35)	6.68 (0.18)	3.65 (0.99)	0.1953
12	2.28 (0.43)	12.65 (0.95)	2.07 (0.34)	1.78 (0.21)	7.07 (0.25)	3.67 (0.04)	0.1819
13	2.17 (0.54)	10.88 (1.46)	1.86 (0.33)	1.96 (0.36)	7.71 (0.34)	3.64 (0.05)	0.2159
14	1.43 (1.06)	13.10 (0.99)	1.88 (0.37)	1.90 (0.24)	8.50 (0.31)	2.30 (0.90)	0.2759
15	2.78 (0.86)	8.90 (1.24)	1.84 (0.20)	1.90 (0.06)	9.23 (0.19)	3.53 (0.58)	0.2049

-- Numbers in parentheses are the standard deviations of the parameter changes that result in the model parameters for that iteration.

-- Numbers in square brackets are starting values for iterations 6-15, not results of iteration 5.

* The time window of S-4 was lengthened at iteration 6.

SCOTCH Inversion Results

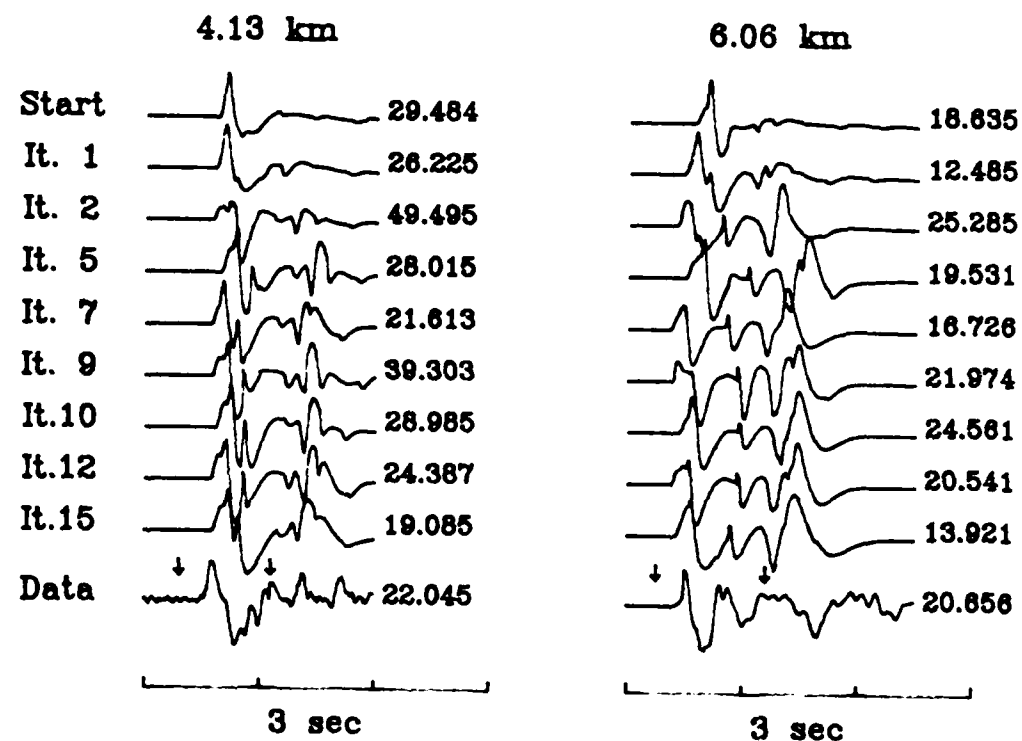


Figure 24. Inversion results for SCOTCH. Shown are synthetic seismograms for the starting model and selected iterations (above) compared with the observed waveforms (below). The format is the same as Figure 15.

SCOTCH Resolution Matrices

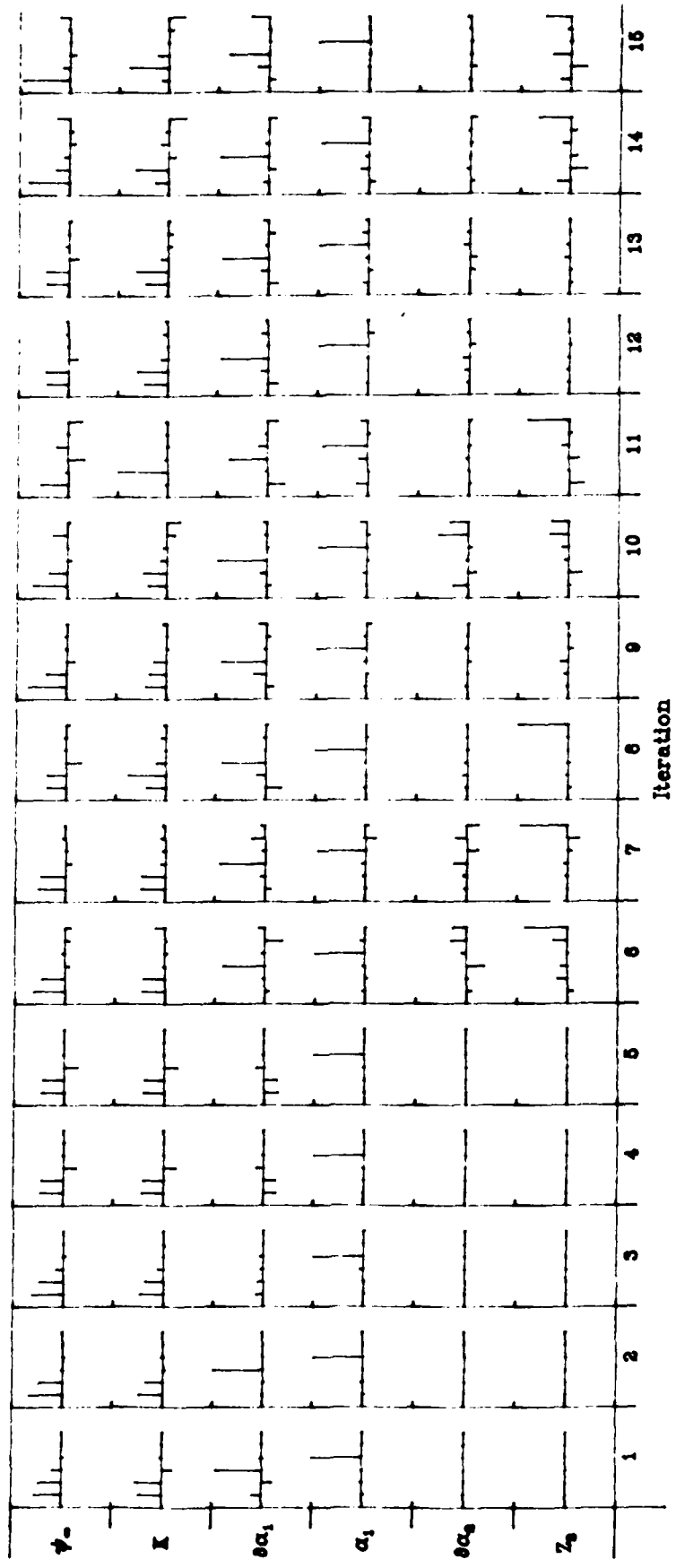


Figure 25. The parameter resolution matrices for each iteration of the inversion of SCOTCH waveforms. Lower gradient parameters were not considered in the first five iterations.

SCOTCH Data Importance Vectors

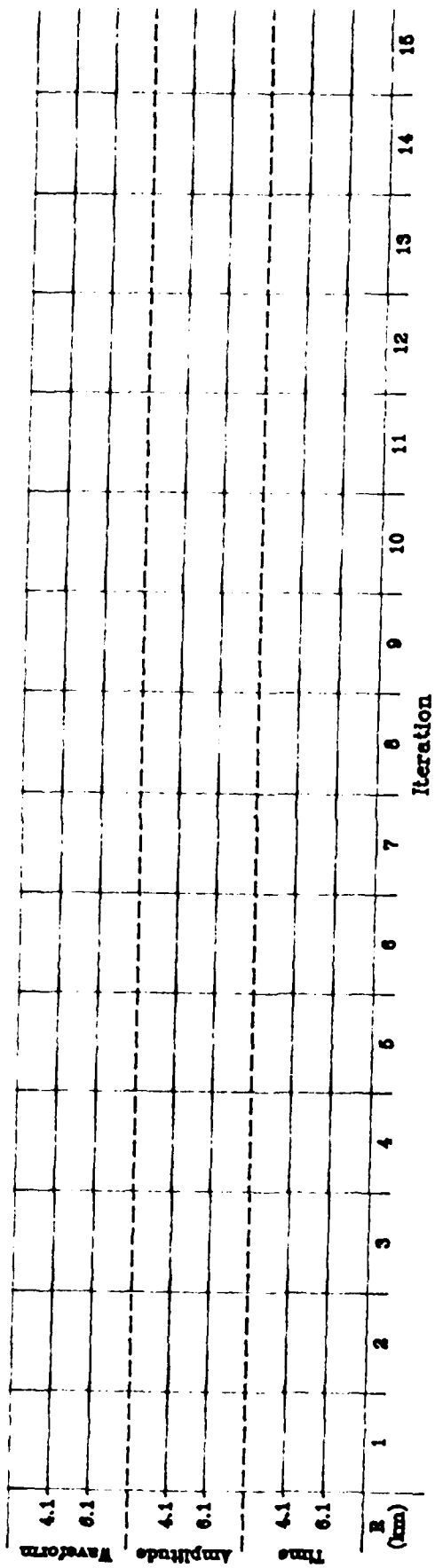


Figure 26. The data importance vectors for each iteration of the SCOTCH waveform inversion. Each residual has equal importance in the determination of the solution.

phase may be identified in the synthetics for station S-3A (Figure 24) which correlates well with an arrival in the observed waveform just outside of the inversions time window. Similarly, the high upper gradient allows the upgoing direct wave at station S-4 to separate in time from the first-arriving diving ray, and is apparent as the second peak in the observed waveform. Because this arrival is well modeled, the inversion time window for station S-4, which originally included only the first peak and trough, was lengthened to that indicated in Figure 24. (This also accounts for the increase in RMS fit at iteration 6 in Table 9). The pP ray at S-4 is quite strong in the synthetics just outside the inversion time window, but is less well correlated with the observed waveform. From the sixth iteration, the depth to the lower layer increases to about 3.5 km, while the lower gradient continuously increases. This is, once again, indicative that the constraint of a second-order discontinuity may be in error, and that a first-order velocity discontinuity beneath the source may be required. Throughout the inversion, Ψ_∞ and k vary notably, reducing confidence in the value obtained at any particular iteration. Although the lower gradient has not yet converged to a final value (and may not) by the fifteenth iteration, the model obtained after this iteration provides a good fit to the first peak amplitudes (Figure 24) and a reasonably improved RMS fit (Table 9). The value of Ψ_∞ obtained for this iteration is more than double the value obtained by Barker, et al. (1985) (the starting model). The corresponding value of k is the smallest of any of the iterations, and is significantly smaller than the value of Barker, et al. (1985).

SUMMARY AND CONCLUSIONS

We have introduced a method for the simultaneous inversion of near-field waveforms for source and structure parameters. For this report, the source was represented by the Helmberger-Hadley (1981) RDP with B held constant. However, any of a number of other effective source functions could be substituted. The structure model is parameterized as a layered stack, in which the free parameters are the velocity at the top of each layer, the velocity gradient within the layer and the depth to the top of the layer. For each observation, the residuals consist of the normalized cross-correlation coefficient between the data and synthetics (a measure of waveform fit), the difference of the normalizations (a measure of absolute amplitude), and the time lag to the peak of the cross-correlation (a measure of absolute travel time). Numerical partial derivatives are computed using asymptotic generalized ray synthetics, and the problem is solved using an iterative generalized inverse.

Test inversions have been performed for simple structure models. The inversion for halfspace velocity is quite robust, but an inversion for a single gradient indicates that the nonlinearity of the problem can cause slow convergence, or even temporary divergence, of the solution. Methods of nonlinear optimization could minimize this problem, but have not, as yet, been implemented. In solving for both surface velocity and gradient, the parameters trade off and the inversion is unstable. However, truncating singular values to damp poorly resolved parameter changes, and preferentially weighting the parameters and residuals, allows the inversion to slowly approach the correct solution. In a final test inversion for the source and a

two-gradient structure model, the inversion is far more sensitive to the parameters of the upper gradient layer than to either the source or lower layer parameters. A procedure was outlined in which we solve in early iterations for estimates of source and upper gradient parameters only, then use these as starting models in further iterations for the total model. Even with this approach, however, the lower gradient parameters could be resolved only when the range of "observed" data was extended.

The inversion was applied to near-field waveforms recorded for four Pahute Mesa explosions to obtain, for each, estimates of the source and of a two-gradient structure model with a second-order discontinuity. The resulting structure models are summarized in Figure 27. For BOXCAR, the structure model was not significantly different from the starting model, which was based on the Pahute Mesa model of Hartzell, et al. (1983). The structure models obtained for INLET, MAST and SCOTCH, however, include a higher gradient in the upper layer, and poor resolution of the lower layer. In fact, the lower gradient for INLET and SCOTCH is actually greater than the upper gradient, suggesting that the constraint that the interface have only a second-order discontinuity may be incorrect. Future inversions of these data sets will free the model to have a first-order velocity discontinuity at depth. Although these results should be considered preliminary, the source parameters obtained for the four events all give estimates of Ψ_∞ higher than those determined by Barker, et al. (1985) using the Hartzell, et al. (1983) structure model. As expected for increased estimates of Ψ_∞ , the estimates of k are decreased somewhat from the Barker, et al. (1985) results for INLET, MAST and SCOTCH. However, the estimate of k for BOXCAR is increased.

Future improvements in the simultaneous inversion procedure might include

Pahute Mesa Structure Models

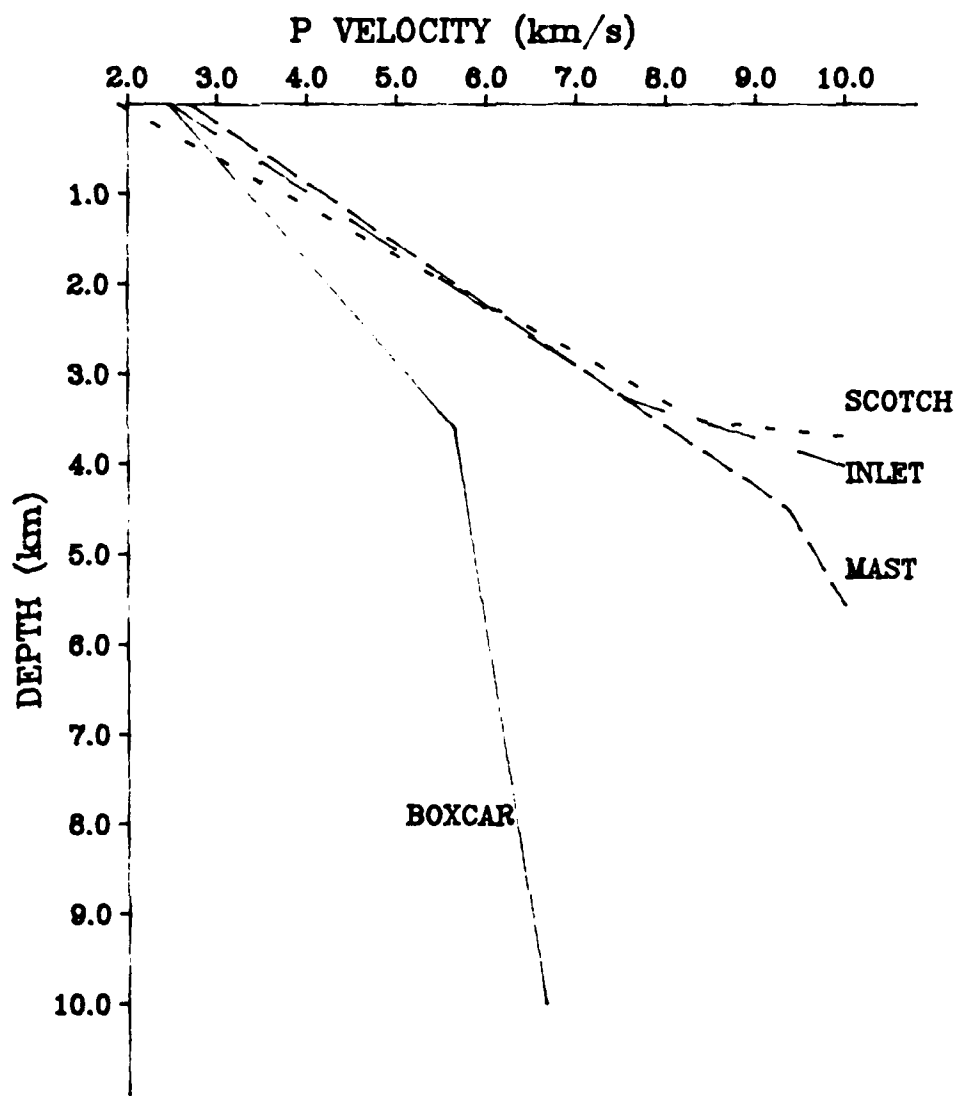


Figure 27. A comparison of velocity structure models resulting from the waveform inversions of the Pahute Mesa events BOXCAR, INLET, MAST and SCOTCH. The model for BOXCAR is very similar to that of Hartzell, et al. (1983). The other models suggest higher velocity gradients in the upper 3-4 km. The deeper portions of these models are poorly resolved and may reflect the constraints placed on the parameters.

the implementation of Shaw and Orcutt's (1985) "jumping" method, as well as nonlinear optimization techniques such as the "conjugate gradient" method. Changes in parameterization include the specification of surface velocity and water table depth, when known, for Pahute Mesa events, as well as allowing first-order velocity discontinuities at depth. Using a quadratic parameterization of the explosion RDP (e.g. Mueller and Murphy, 1971) will require inclusion of depth-dependent attenuation in the structure model. It will be of interest, however, to determine how the choice of source function affects the structure model obtained, and to investigate the relative waveform matches of the two approaches. Applications to data from other sites might include surface and borehole records of Yucca Flats events modeled by Wallace and Barker (1986), as well as near-field data from non-NTS shots such as GASBUGGY, RULISON and RIO BLANCO.

REFERENCES

- Barker, J. S., S. H. Hartzell, L. J. Burdick and D. V. Helmberger (1985). Effective source functions for underground nuclear tests at Pahute Mesa from near-field modeling, Final Technical Report WCCP-R-85-02, Woodward-Clyde Consultants, Pasadena.
- Barker, J. S., L. J. Burdick and T. C. Wallace (1986). Analysis of near-field seismic waveforms from underground nuclear explosions, Scientific Report # 1, AFGL-TR-85-0321, ADA165227, Woodward-Clyde Consultants, Pasadena.
- Brown, M. G. (1982). Inverting for the ocean sound speed structure, Ph.D. thesis, UCSD.
- Burdick, L. J. and G. R. Mellman (1976). Inversion of the body waves from the Borrego Mountain earthquake to the source mechanism, Bull. Seismol. Soc. Am., 66, 1485-1499.
- Burdick, L. J., D. M. Cole, D. V. Helmberger, T. Lay and T. Wallace (1982). Effective source functions from local surface measurements, Final Technical Report WCCP-R-82-01, Woodward-Clyde Consultants, Pasadena.
- Burdick, L. J., T. Wallace and T. Lay (1984). Modeling near-field and teleseismic observations from the Amchitka test site, J. Geophys. Res., 89, 4373-4388.
- Chapman, C. H. and J. A. Orcutt (1985). Least-squares fitting of marine seismic refraction data, Geophys. J. Roy. astr. Soc., 82, 339-374.
- Dziewonski, A. M., T.-A. Chou and J. H. Woodhouse (1981). Determination of earthquake source parameters from waveform data for studies of global and regional seismicity, J. Geophys. Res., 86, 2825-2852.
- Given, J. W. (1984). Inversion of body-wave seismograms for upper mantle structure, Ph.D. thesis, Caltech.
- Hartzell, S. H., L. J. Burdick and T. Lay (1983). Effective source functions for Pahute Mesa nuclear tests, Final Technical Report WCCP-R-83-3, Woodward-Clyde Consultants, Pasadena.
- Haskell, N. A. (1967). Analytic approximation for the elastic radiation from a contained underground explosion, J. Geophys. Res., 72, 2583-2587.
- Helmberger, D. V. (1974). Generalized ray theory for shear dislocations, Bull. Seismol. Soc. Am., 64, 45-64.

- Helmberger, D. V. and D. G. Harkrider (1978). Modeling earthquakes with generalized ray theory, in J. Miklowitz and J. Achenback - eds., Proc. of IUTAM Symposium: Modern Problems in Elastic Wave Propagation, J. Wiley & Sons, New York.
- Helmberger, D. V. and D. M. Hadley (1981). Seismic source functions and attenuation from local and teleseismic observations of the NTS events JORUM and HANDLEY, Bull. Seismol. Soc. Am., 71, 51-67.
- Jackson, D. D. (1979). The use of a priori data to resolve non-uniqueness in linear inversion, Geophys. J. Roy. astr. Soc., 57, 137-157.
- Langston, C. A. (1981). Source inversion of seismic waveforms: the Koyna, India, earthquakes of September 13, 1967, Bull. Seismol. Soc. Am., 71, 1-24.
- Leonard, M. A. and L. R. Johnson (1986). Velocity structure of Silent Canyon Caldera, Nevada Test Site, J. Geophys. Res., submitted.
- McEvilly, T. V. and L. R. Johnson (1986). Regional studies with broadband data, in Papers Presented at 8th Annual DARPA/AFGL Seismic Research Symposium, 44-51.
- Mellman, G. R. (1980). A method for waveform inversion of body-wave seismograms, Ph.D. thesis, Caltech.
- Mueller, R. A. and J. R. Murphy (1971). Seismic characteristics of underground nuclear detonations, Part I Seismic scaling law of underground detonations, Bull. Seismol. Soc. Am., 61, 1675-1692.
- Nabelek, J. L. (1984). Determination of earthquake source parameters from inversion of body waves, Ph.D. thesis, MIT.
- Shaw, P. R. (1983). Waveform inversion of explosion seismology data, Ph.D. thesis, UCSD.
- Shaw, P. R. and J. A. Orcutt (1985). Waveform inversion of seismic refraction data and applications to young Pacific crust, Geophys. J. Roy. astr. Soc., 82, 375-414.
- Stump, B. W. and L. R. Johnson (1977). The determination of source properties by the linear inversion of seismograms, Bull. Seismol. Soc. Am., 67, 1489-1502.
- Stump, B. W. and L. R. Johnson (1984). Near-field source characterization of contained nuclear explosions in tuff, Bull. Seismol. Soc. Am., 74, 1-26.
- von Seggern, D. and R. Blandford (1972). Source time functions and spectra for underground nuclear explosions, Geophys. J. Roy. astr. Soc., 31, 83-97.

Wallace, T. C. (1983). Long period regional body waves, Ph.D. thesis,
Caltech.

Wallace, T. C. (1986). The tectonic release signature at regional distances,
in Papers Presented at 8th Annual DARPA/AFGL Seismic Research Symposium,
150-158.

Wallace, T. C. and J. S. Barker (1986). Modeling of near-field observations
from nuclear explosions in dry tuff and alluvium, Bull. Seismol. Soc.
Am., submitted.

Wiggins, R. A. (1972). The general linear inverse problem: Implications of
surface waves and free oscillations for earth structure, Rev. Geophys.
Space Phys., 10, 251-285.

Part II
AVERAGE Q AND YIELD ESTIMATES FROM THE
PAHUTE MESA TEST SITE

R. W. Burger, T. Lay and L. J. Burdick

ABSTRACT

Attenuation models, with and without frequency dependence, have been developed through analysis of time-domain amplitude measurements and teleseismic spectral shape data from Pahute Mesa nuclear explosions. The time-domain analysis is based on a near-field to far-field amplitude comparison. The near-field amplitude information is incorporated in two parameterized explosion source models (Mueller-Murphy and Helmberger-Hadley) based on analyses of near-field data. The teleseismic amplitude observations are from a large dataset of WWSSN short-period analog recordings. For the narrow-band time-domain data, the various source and attenuation models are indistinguishable. We utilize the spectral shape data in the 0.5 to 4 Hz band as a constraint on the source-attenuation models at higher frequencies, concluding that either source model, when convolved with the appropriate frequency dependent Q model, can be consistent with both the near-field and far-field time-domain amplitudes and the spectral shape data. Given the trade-off between source and attenuation models and the similarity of the different source models in the 0.5 to 4 Hz band, it is difficult to clearly prefer one source model over the other. The Mueller-Murphy model is more consistent with surface wave amplitude measurements, because of larger predicted long-period energy levels. Whether or not frequency dependence is included in the attenuation model, the value of t^* near 1 Hz is about 1.0 sec assuming the Mueller-Murphy source, or 0.8 sec assuming the Helmberger-Hadley source model. This 0.2 sec difference results from greater 1 Hz energy levels for the Mueller-Murphy source model. Adopting an average attenuation model, predicted amplitudes and yields are shown to be within the uncertainty of the data for all the events analyzed.

INTRODUCTION

Understanding the nature and effect of the earth's anelasticity on seismic body waves is an important problem in seismic yield estimation. Reliable estimates of yield based on network-averaged short-period m_b require detailed knowledge of P-wave attenuation in the earth. Furthermore, it is now recognized that the earth's anelasticity has significant lateral variations. Thus it is necessary to estimate the deviation of t^* from the global average in the short-period body wave band at a given test site to predict the m_b -yield relation baseline for that site. Bache et al. (1985, 1986) and Der et al. (1985) have used spectral shapes and decay rates of teleseismic P waves from explosions to estimate the level and frequency dependence of Q. However, spectral methods for estimating Q have several potential sources of error (Cormier, 1982). Most important is that spectral decay methods require a priori knowledge of the source spectrum. Errors in the assumed source spectral falloff rate translate into a bias in the attenuation measurement. This presents a problem in the spectral decay studies of explosion signals given that explosion source models with different spectral falloff characteristics have been proposed at various times (e.g. Haskell, 1967; Mueller and Murphy, 1971; von Seggern and Blandford, 1972; and Helmberger and Hadley, 1981)

A common misconception is that these source models can be effectively characterized by their high frequency spectral falloff rates (f^{-2} , f^{-3} , or f^{-4}). However, we show in this work that this is not necessarily the case. For the wide range of yields investigated in this study (155 to 1300 Kt), the Helmberger and Hadley (1981) source which has an asymptotic spectral decay rate of f^{-3} , has spectral properties in the band of interest (0.5-4 Hz)

similar to the Mueller and Murphy (1971) source, which has an f^{-2} asymptotic decay. We also show that these source models, when convolved with an appropriate attenuation model, are indistinguishable in WWSSN short-period data. It is likely that none of these source models is completely accurate. The spectrum may initially decay at one rate and then, at a higher frequency, begin to decay at a faster rate.

Time-domain modeling of explosion signals provides an alternate method to the spectral shape procedures for estimating attenuation. However, separate analysis of time-domain and spectral decay information may produce incompatible results, given the different intrinsic sensitivity of each procedure (Cormier, 1982). In this investigation, we have measured the attenuation of P waves from explosions at the Pahute Mesa test site utilizing time-domain amplitude data in the 0.5-2 Hz band (WWSSN short-period) and spectral decay information as a constraint on the source-attenuation models at frequencies up to 4 Hz.

To eliminate the trade-off between source and attenuation, several investigators have used source canceling methods to isolate the effects of propagation through the anelastic earth. Jordan and Sipkin (1977) and Sipkin and Jordan (1979, 1980) among others have used multiple ScS waves as a direct measure of the average shear wave Q in the mantle. Since each leg of the ScS arrival should have the same source excitation, differences in the frequency content of successive multiples can be attributed to attenuation. Burdick (1985) used the relative frequency content of ScS and ScP waves to estimate the average mantle Q. These, and other phase pairs such as sP-sS (Burdick, 1978) and P-PP (Shore, 1983), provide an unbiased estimate of attenuation. A recent review on the subject of body-wave attenuation was presented by Cormier (1982).

Phase pairs for which source canceling studies like those described above might be carried out are not commonly observed from explosions. However, nuclear sources have been well recorded in the near-field and near-regional field. This allows an alternate procedure of determining the initial source excitation from the near-field data and estimating Q by matching the observed teleseismic amplitudes. This type of investigation has been made previously by Frasier and Filson (1972), Helmberger and Hadley (1981), and Burdick *et al.* (1984).

Near-field records from explosions at Pahute Mesa have been studied extensively. Yield-scaled source models have been developed from this data using two different approaches. Mueller and Murphy (1971) compared yield scaling exponents as a function of frequency for events of various sizes recorded at a common station. Murphy (1977) later refined their representation into what is referred to in this paper as the Mueller-Murphy source model. Helmberger and Hadley (1981) developed their f^{-3} model by forward modeling of a small set of observations, but they did not present yield scaling relations. Pahute Mesa yield scaling relations for the latter source representation were later developed by Barker *et al.* (1985) along with source models for a wider range of events. These two different types of studies account for the complex process of near-field wave propagation in very different ways, and assume different parametric forms for the source time history (spectrum). We consider both the Mueller-Murphy (1971) and Helmberger-Hadley (1981) source models in our modeling to illustrate the trade-offs between source and attenuation models in the 0.5 to 4 Hz band, and to appraise the various claims in the literature that one model is superior to the other.

It is widely recognized that the effective value of Q for the mantle

varies with frequency within the body wave band (0.2 to 20 sec). However, it is common practice to assume that within the frequency band of any one type of narrow-band data, Q is independent of frequency. The variation of Q with frequency is inferred by comparing the results of several different types of studies (e.g. Burdick, 1985). In this work, we have considered both frequency independent (Futterman, 1962) and frequency dependent models for attenuation filters. The frequency dependent attenuation model that we use is the standard linear solid model described by Minster (1978a, 1978b). Our goal was to find whether either source model or either attenuation model did a superior job of fitting the combined teleseismic spectral and amplitude data sets from Pahute Mesa. Our conclusion is that any of the four source-attenuation model pairs can satisfy short-period WWSSN observations. But, when using spectral shape data in the 0.5 to 4 Hz band as an additional constraint, we find it necessary to include a frequency dependent attenuation model. Furthermore; for the Minster Q models, both source models are consistent with the amplitude and spectral shape data in this band.

MODELING APPROACH

The basic approach taken in this investigation is to attempt to simultaneously match observed teleseismic amplitudes and magnitudes by computing synthetic seismograms using source models which fit near-field data. The parameters that we adjust to fit the data are the free parameters in two standard attenuation models. The reason for matching both the period-corrected amplitude (magnitude) and the uncorrected amplitude is to obtain a reasonable measure of how well the source and attenuation models

predict the average period of the observed P waves. We also ensure that the synthetic waveforms agree with the data.

Observations. The observations that we will attempt to match are of two different types. The first type are teleseismic short-period P-wave amplitude and magnitude observations as measured from WWSSN film chips. A large data base of such measurements from 25 Pahute events was processed in a thorough and uniform fashion by Lay (1985). He measured over 1200 amplitude values and obtained from them average log amplitudes and average magnitudes. The amplitude and magnitude values to be modeled here are given in Table 1. The amplitude that we model is that of the first upswing to first downswing of the explosion waveform. This amplitude is not influenced by the pP arrival for these events (Lay, 1985), but the pP arrival may influence the period measurement. Thus the synthetic magnitudes may be somewhat affected by incorrect pP delay time estimates. The band of WWSSN short-period data is 0.5 to 2 Hz. Therefore the time-domain amplitude data discussed in this paper (and any possible spectral data from these instruments) are sensitive only to the spectral level in this band.

The second type of observations that we wish to match are spectral shape observations in the 0.5-4 Hz band. Unfortunately, body wave spectra which are hand digitized from analog records are not reliable at high frequencies, so we cannot use the spectra of the P waves studied by Lay (1985). Der et al. (1985) analyzed the spectral shapes of Pahute Mesa events using several different broad-band recording systems. They assumed the von Seggern and Blandford (1972) source function and determined a frequency independent value of t^* in the 0.5-4 Hz band of 0.4 to 0.5 sec for Pahute Mesa. We have computed a synthetic spectrum using this information and we here treat it as

Table 1

PAHUTE MESA EVENTS STUDIED *

Event	Date	Log Amp	m_b	Yield (Kt)	K (s^{-1})	Ψ_{∞} ($\times 10^{10} \text{ cm}^3$)
ALMENDRO	6/66/73	2.48±0.09	5.96±0.10		7.5	5.7
BENHAM	12/19/68	2.62±0.09	6.16±0.09	1150		
BOXCAR	4/26/68	2.59±0.09	6.12±0.11	1300	6.5	12.0
GREELEY	12/20/66	2.54±0.10	6.09±0.11	870		
HALFBEAK	6/30/66	2.31±0.09	5.81±0.09	365	9.0	3.8
INLET	11/20/75	2.23±0.11	5.71±0.11		8.0	3.2
MAST	6/19/75	2.31±0.11	5.81±0.12		7.5	4.7
SCOTCH	5/23/67	1.93±0.10	5.39±0.11	155	12.0	1.3

* The amplitudes and magnitudes are from Lay (1985). The Helmberger-Hadley source parameters K and Ψ_{∞} are from Barker et al. (1985).

an observation. We will also consider the results from the spectral studies of Bache et al. (1986). They obtained Pahute Mesa spectra and magnitude data from the UKAEA and NORSAR arrays and modeled it using the Mueller and Murphy (1971) source model. They solved for frequency independent and frequency dependent values of t_o^* , concluding that the data requires a frequency dependent Q operator. The spectral shape data from these two studies are quite consistent with each other, but there is a general difference in the interpretation (Bache et al., 1986). We will constrain the models developed here from the time-domain amplitude data to match the spectral shape data as well.

Attenuation Models. Two of the most commonly used attenuation models in body wave seismology are the frequency independent Futterman (1962) and the frequency dependent standard linear solid (Minster, 1978a, b) models. The Futterman model is parameterized by a single value, t^* , obtained by integrating the slowness divided by Q over the raypath. The standard linear solid attenuation model is parameterized by three values. These are the minimum value of Q, the high frequency characteristic relaxation time, τ_m , and the low frequency relaxation time, τ_M . τ_m controls the increase of Q at short periods and τ_M controls the increase at long periods. Since we will be modeling short-period observations, we simply fix τ_M at 1000 sec for all calculations. The attenuation model is then reparameterized in terms of a long period value of t^* , designated by t_o^* , and τ_m .

A reasonable range for t_o^* can be established from normal mode and long-period multiple ScS data. Anderson and Given (1982) give values of t_o^* based on normal mode data that range from 0.9 to 1.2 sec between distances of 30° and 80° at a period of 100 sec. Sipkin and Jordan (1979) found that good

quality multiple ScS data gives slightly lower values of Q than the mode data. Burdick (1982) found that their observed average value for whole mantle Q translates to a t_o^* of about 1.3 sec. Thus a reasonable range of values to consider is 0.9 to 1.3 sec.

Source Models. The explosion source models which we will use in our study are the Mueller-Murphy tuff source and the Helmberger-Hadley source representations. Murphy (1977) provides the yield scaling relations appropriate for Pahute Mesa. The form of these relations is based on theoretical and observational considerations. They provide an analytic expression for the source as a function of yield, burial depth and material properties. We assume that the material properties are relatively constant at Pahute Mesa, so that as long as yield is known we can derive the source time history and its spectrum. Five events in the Pahute Mesa data set had announced yields; SCOTCH, HALFBEAK, GREELEY, BOXCAR and BENHAM. The announced yields are given in Table 1. In the following, we use the seismic observations from these five events to obtain average Futterman and Minster Q operators. We then predict yields for the remainder of the events assuming that these models are correct.

The Helmberger-Hadley source model is based on forward modeling studies of near-field data from Pahute Mesa events (Hartzell et al., 1983; Barker et al., 1985). The band of their data is 1 to 5 Hz, so that their source models are appropriate to use in our investigation. Yield scaling laws were developed, but are empirical in nature and based on few data points. It is thus most reasonable to use the source models developed for particular events whenever possible and we shall do so in the following. Six events were forward modeled with good success in these studies. They were BOXCAR, SCOTCH,

ALMENDRO, HALFBEAK, INLET and MAST. The Helmberger-Hadley source parameters K (corner frequency) and Ψ_∞ (DC level) are given in Table 1. Again, we use these six events to establish the attenuation operators and then predict the yields of the remaining events.

Three events with announced yields have been forward modeled; BOXCAR, SCOTCH and HALFBEAK. We concentrate primarily on them in the following. A comparison of the Helmberger-Hadley (H-H) and Mueller-Murphy (M-M) source models for these three events is shown in Figure 1. The first point to note is that even though the two formalisms are mathematically different, they have very similar corner frequencies and spectral slopes near 1 Hz. The similarity of these features extends over a wide range of yield, from 155 Kt (SCOTCH) to 1300 Kt (BOXCAR). This similarity suggests that Mueller and Murphy (1971) and Barker et al. (1985) were resolving the same yield scaling information and simply modeling it with different formalisms. It appears that the best agreement between the two source models would be obtained if the Helmberger-Hadley model were given less overshoot. The Mueller-Murphy source models have larger spectral displacement amplitudes than the Helmberger-Hadley source models for all three events. As we show in the following, this means that utilization of the Mueller-Murphy source requires slightly higher values of t^* . It is also important to note that, even though the Helmberger-Hadley source ultimately has a higher spectral falloff rate, it does not become apparent until frequencies exceeding 4 Hz. Thus, this difference between the sources is not significant for modeling data band-limited to frequencies lower than this.

The differences between the two source formalisms are further illustrated in Figure 2. The frequency dependence of the spectral slope is displayed at the top. The two source models have almost identical slopes

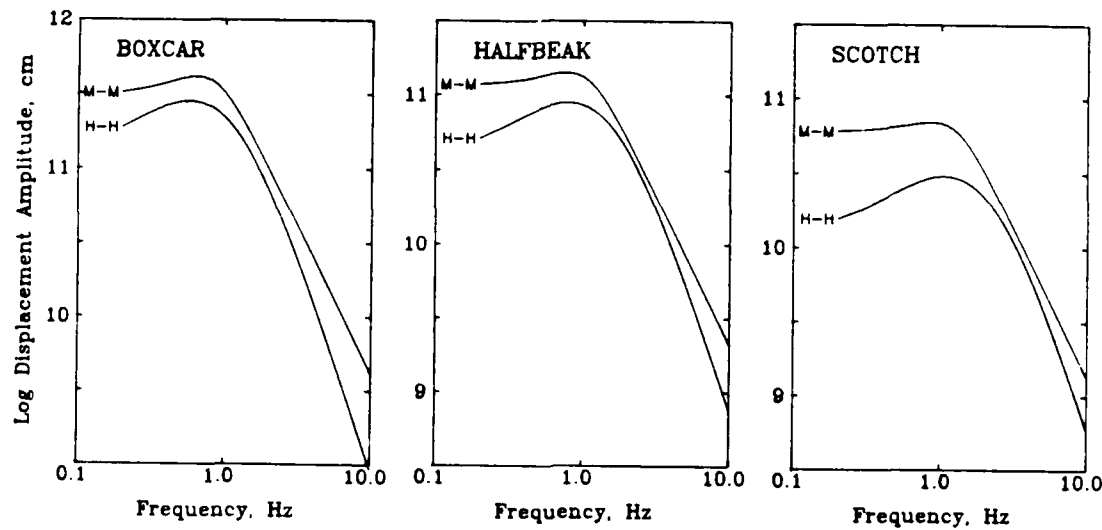
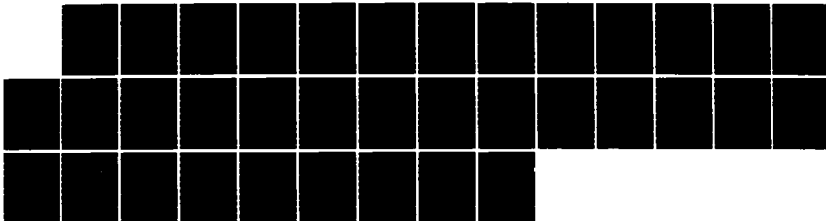
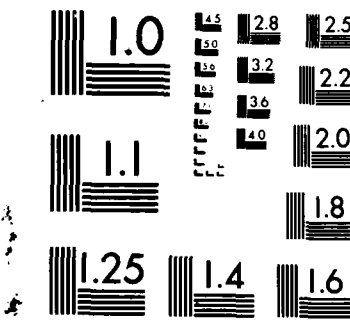


Figure 1. Predicted far-field source displacement spectra for BOXCAR, HALFBEAK, and SCOTCH. The Mueller-Murphy (1971) source models are based on the announced yields. The Helmberger-Hadley (1981) source models are based on the near-field modeling results of Barker et al. (1985).

AD-A174 003 INVERSION FOR SOURCE PARAMETERS OF UNDERGROUND NUCLEAR . 2/2
EXPLOSIONS WITH IM. (U) WOODWARD-CLYDE CONSULTANTS
PASADENA CA J S BARKER ET AL. 15 MAR 86 WCCP-R-86-81
UNCLASSIFIED AFGL-TR-86-0142 F19628-85-C-0036 F/B 8/11 NL





MICROCOPY RESOLUTION TEST CHART
NATIONAL BUREAU OF STANDARDS 1963-A

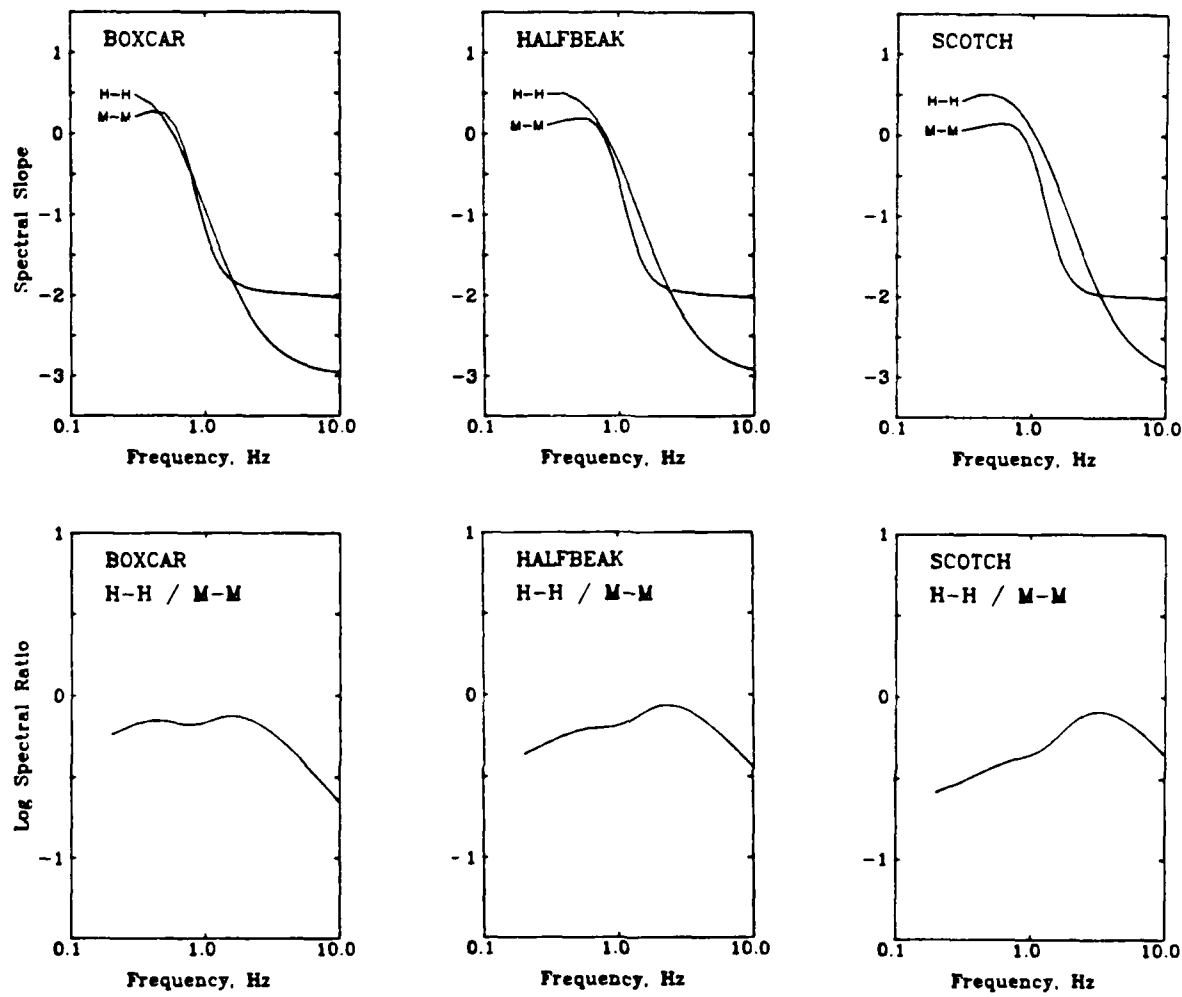


Figure 2. Top: spectral slope for the displacement spectra shown in Figure 1. Bottom: the spectral ratio of the Helmberger-Hadley to Mueller-Murphy source spectra in Figure 1.

between 0.5 and 3 Hz. The spectral slope of the Helmberger-Hadley model does not drop below that of the Mueller-Murphy source until frequencies from 2 to 4 Hz. The slope of the Helmberger-Hadley spectrum does not reach -3 until 10 Hz. This illustrates the danger of attempting to correct spectra for source effects by simply multiplying by f^n . The spectral ratios of the source functions are shown at the bottom of Figure 2. They illustrate again that the Mueller-Murphy model consistently predicts slightly higher amplitudes at all frequencies. The spectral ratios also demonstrate that the ratio of the source models vary with frequency by no more than a factor of 3, even up to 10 Hz. Furthermore, the ratio of the source models for HALFBEAK and BOXCAR varies by less than a factor of 2 between 0.5 and 4 Hz, thus making these two source models difficult to distinguish from one another using observed data in this band.

In the spectral shape and decay analysis, absolute amplitude information is not utilized, so the baseline difference between the two source models has no effect. It is apparent in Figure 2 that given spectral data in the 0.5-4 Hz band, the difference between correcting the observed spectrum for the Mueller-Murphy source model versus the Helmberger-Hadley model will depend somewhat on the yield of the event, being negligible for large events and increasing slightly for small events. Also, for small events, the Helmberger-Hadley source correction will actually lead to lower Q values, just the opposite effect of simply correcting for f^{-3} instead of f^{-2} .

RESULTS

Time-Domain Amplitudes. We begin this modeling study by considering the amplitude and magnitude data of Lay (1985). Since we do not have accurate spectra for the WWSSN data, we model it in the time domain. We compute synthetic seismograms at a distance of 50° using the near-field source models convolved with the appropriate attenuation model and the WWSSN short-period instrument response. The synthetic seismograms include the direct P and pP arrivals. The pP delay times and amplitudes were measured using a complete waveform analysis called intercorrelation (Lay, 1985). Figure 3 illustrates the procedure for determining the attenuation models from the amplitude data for the event HALFBEAK. In the case shown, we found values for t^* in the Futterman operator (top) and τ_m in the Minster operator that match the observed average amplitude. We consider three different values of t_o^* in the Minster model (1.0, 1.15 and 1.3 sec) as illustrated in the bottom three rows of the figure.

The synthetic waveforms for the Helmberger-Hadley source are different enough to allow us to select a preferred value of t_o^* . For comparison, shown at the right of Figure 3 are representative observed waveforms for the event HALFBEAK. For the Helmberger-Hadley source with the Minster Q model, the first synthetic waveform ($t_o^*=1$ sec) resembles the observations most closely. The period of the first upswing is too short and its relative amplitude too high in the lower two synthetic waveforms. Also, the shoulder in the second upswing, which is associated with the pP arrival, is not clear in the data. There are trade-offs here with the pP parameters, but we are assuming that the values measured by Lay (1985) are correct. For the Mueller-Murphy source, it is clear that there is a strong trade-off between the two parameters in the

HALFBEAK log A=2.31 mb=5.81

Synthetic Seismograms

Mueller-Murphy

t_0^* =0.93



mb=5.85

$t_0^*=1.0$
 $\tau_m=0.017$



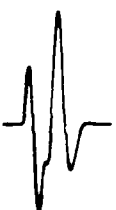
5.83

$t_0^*=1.15$
 $\tau_m=0.045$



5.80

$t_0^*=1.3$
 $\tau_m=0.069$



5.79

Helmberger-Hadley

$t_0^*=0.77$



5.77

$t_0^*=1.0$
 $\tau_m=0.047$



5.77

$t_0^*=1.15$
 $\tau_m=0.070$



5.68

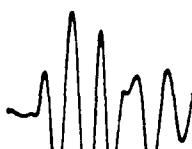
$t_0^*=1.3$
 $\tau_m=0.091$



5.67

Observations

CAR



LPB



OGD



STU



WES



Figure 3. Teleseismic WWSSN short-period synthetic seismograms for HALFBEAK. The source functions are shown in Figure 1. The attenuation models are those that produce synthetic amplitudes which match the observed amplitudes. The synthetic seismograms include a pP arrival (given by Lay, 1985). Also given for each synthetic seismogram is the synthetic magnitude. Shown at the right are representative WWSSN short-period teleseismic observed waveforms for HALFBEAK.

Minster Q operator. There are no substantial differences between the predicted waveforms. Fortunately, a preferred value of t_o^* can be established through consideration of the magnitude combined with the amplitude information.

The analysis of the magnitude data of Lay (1995) is carried out in the same way as that of the amplitude values. We determine values for the parameters in the attenuation models that match m_b , given by

$$(1) \quad m_b = \log(A/T) + P(\Delta)$$

where A is amplitude in millimicrons, T is period, and $P(\Delta)$ is the distance correction given by Veith and Clawson (1972).

Modeling studies like the one illustrated in Figure 3 were carried out on the five events with announced yield using the Mueller-Murphy source and on the six events with near-field models using the Helmberger-Hadley source. The results were averaged and are presented in Table 2. The average Futterman t^* values for the Helmberger-Hadley source are 0.79 and 0.75 sec based on the amplitude and magnitude observations, respectively. The corresponding values for the Mueller-Murphy source are 0.99 and 1.05. The error bounds given in the table represent one standard deviation. The result that the t^* estimates are about 0.2 sec larger for the Mueller-Murphy source compared to the Helmberger-Hadley source model is related to the fact that the Mueller-Murphy source model contains significantly more 1 Hz energy than the Helmberger-Hadley source model for events with similar yield (see Figures 1 and 2). The uncertainties in the average t^* measurements are generally smaller for the Mueller-Murphy than for the Helmberger-Hadley source model. Also, the uncertainties are generally smaller for the amplitude observations

Table 2
AVERAGE ATTENUATION MODELS

Futterman Attenuation Models:

	<u>Murphy Source</u>	<u>Helmberger Source</u>
t^* from Log A	0.99 ± 0.04 (M*F)	0.79 ± 0.06 (H*F)
t^* from m_b	1.05 ± 0.08	0.75 ± 0.08

Minster Attenuation Models:

	<u>Murphy Source</u>	<u>Helmberger Source</u>
$t_o^* = 1.25$ seconds		$t_o^* = 1.00$ seconds
τ_m from Log A	0.051 ± 0.008 (M*M)	0.044 ± 0.011 (H*M)
τ_m from m_b	0.052 ± 0.016	0.060 ± 0.016

than for the magnitude observations.

It is still necessary to select a preferred value of t_o^* appropriate for Mueller-Murphy source model. We found that on average over all the events studied the value of $t_o^*=1.25$ sec made it easiest to simultaneously fit the amplitude and magnitude observations with the Mueller-Murphy source. We therefore selected it as our preferred value. The average τ_m that matched the log amplitude data (0.051) is almost identical to the value that matched the magnitude data (0.052). This indicates that this source-attenuation model predicts both the observed amplitude and period of the teleseismic waveforms. The average values and standard deviations of τ_m are given in Table 2. The τ_m measurements (with $t_o^*=1.0$ sec) assuming the Helmberger-Hadley source model are different for the log amplitude (0.044) and magnitude (0.060) data. The result that the magnitude observations give a larger τ_m than the amplitude data indicates that, for the Minster Q model that predicts the observed amplitudes, the period is too low (i.e. the Helmberger-Hadley waveforms are too high in relative frequency content). We choose $t_o^*=1.0$ sec as the preferred value for the Helmberger-Hadley source model because that value represents a lower bound for t_o^* . Larger values will only result in synthetic waveforms that are higher frequency since a larger t_o^* will require a larger τ_m to match the observed amplitudes.

The Futterman t^* measurements also indicate that the Helmberger-Hadley synthetic waveforms are higher in relative frequency content than the Mueller-Murphy waveforms in the 0.5-2 Hz frequency band. (This result is most clearly shown in Figures 1 and 2 and will be further illustrated in the next section.) If the measured t^* from log amplitudes is larger than that from the magnitudes (as for the Helmberger-Hadley source model), then the synthetic seismograms are too high in relative frequency. For the Mueller-Murphy source

model, the Futterman Q model gives synthetic waveforms which are too long-period. However, the Minster attenuation model, which does not attenuate high frequencies as strongly, matches both the observed amplitude and period.

We believe that the models based on the log amplitude observations are more accurate than those based on the magnitude observations. This is because the amplitude data involves only one measurement while the magnitudes require two, with the signal period being occasionally difficult to measure in the data. Furthermore, the period measurement is somewhat influenced by pP delay time. Errors in the pP delay time may alter the attenuation models that fit the magnitude data.

Synthetic seismograms for the two source models and the average attenuation models (based on the log amplitude observations) for the BOXCAR, HALFBEAK, and SCOTCH events are shown in Figure 4. Also given are the log amplitude and magnitude residuals. These are the difference between the observed and predicted values (a positive residual means that the predicted value is smaller than the observed). These residuals indicate how well the various average attenuation models match the observed amplitudes and magnitudes. The log amplitude residuals are shown in Figure 5 for each attenuation and source model. The events are ordered by estimated yield. No trend of the residuals with yield is apparent. In general, the Mueller-Murphy residuals are slightly smaller than the Helmberger-Hadley residuals.

To illustrate how well the attenuation models based on the log amplitude data predict the magnitudes, the magnitude residuals for those models are given in Figure 6. These tend to be larger than the log amplitude residuals. This is not a surprising result since the average attenuation models are based on the amplitude data and the observed magnitudes are subject to errors in period measurements. Again, no trend in residual with yield is apparent.

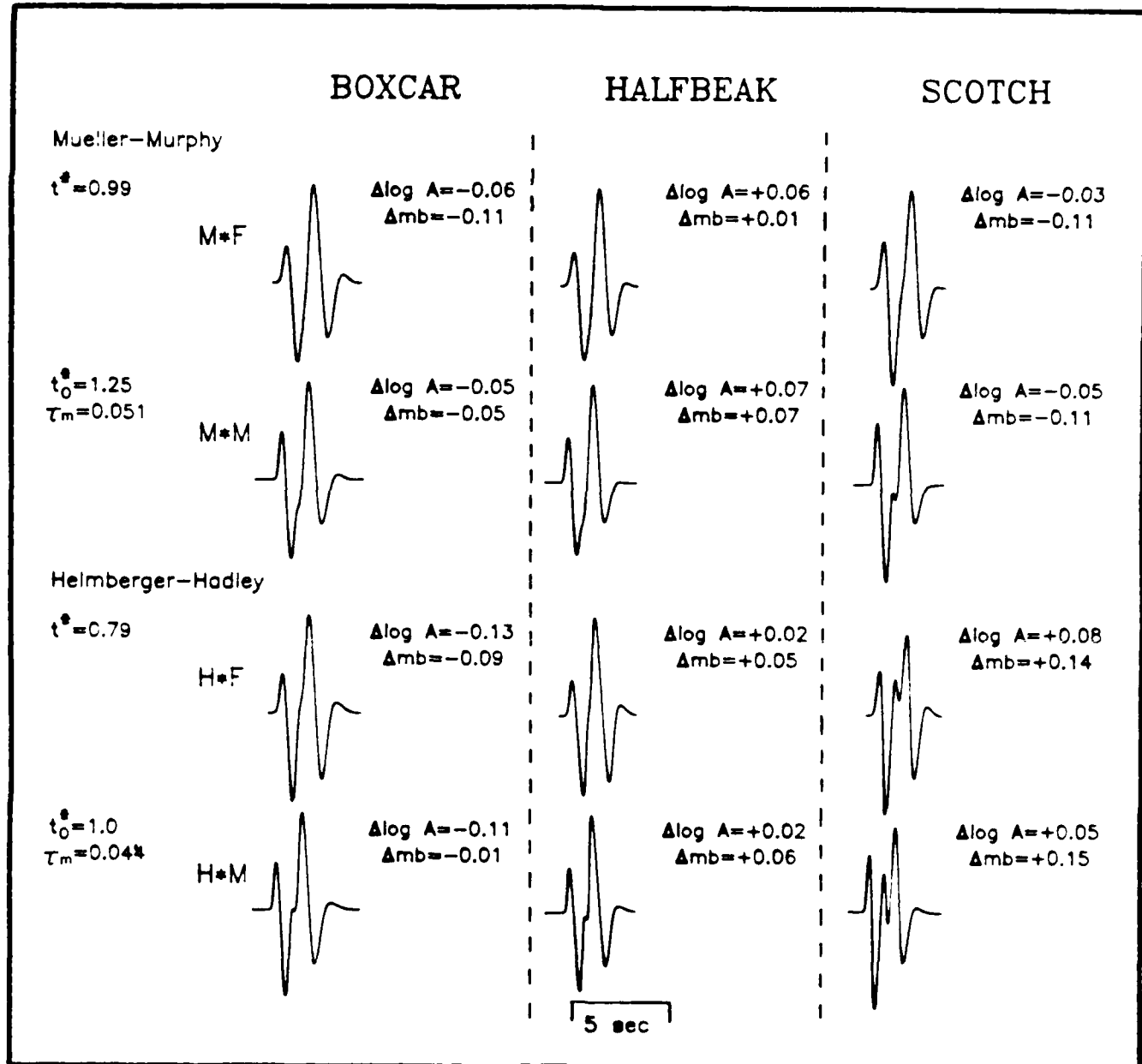


Figure 4. Teleseismic WWSSN short-period synthetic seismograms for BOXCAR, HALFBEAK, and SCOTCH. The source functions are those shown in Figure 1. The attenuation models are the average models that predict the log amplitude observations (given in Table 2). Shown with the synthetic seismograms are the log amplitude and magnitude residuals.

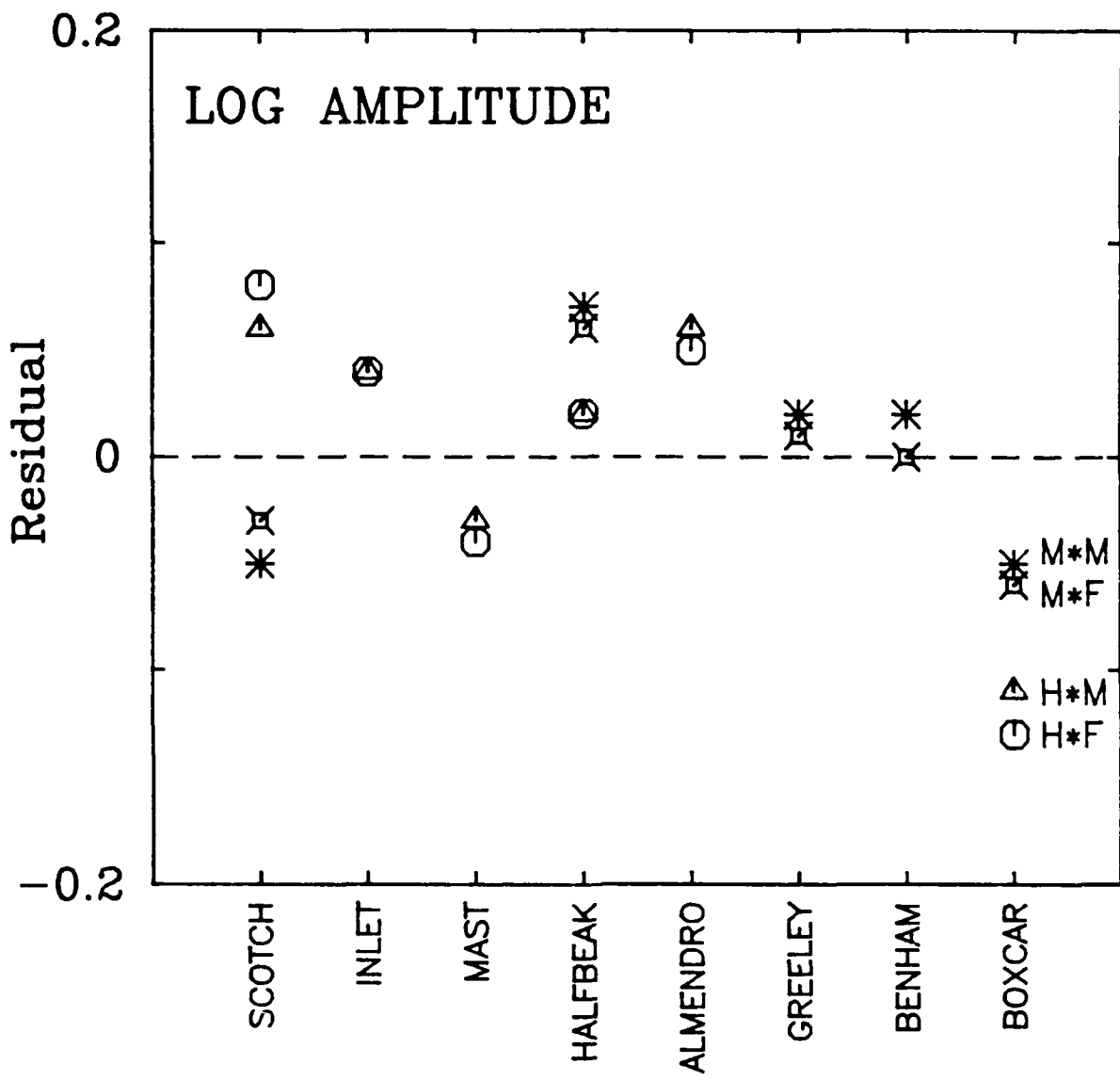


Figure 5. Log amplitude residuals for each of the attenuation-source models. The average attenuation models are from log amplitude observations and are given in Table 2. The source models are based on the announced yields (Mueller-Murphy source) or on near-field modeling (Helmberger-Hadley source).

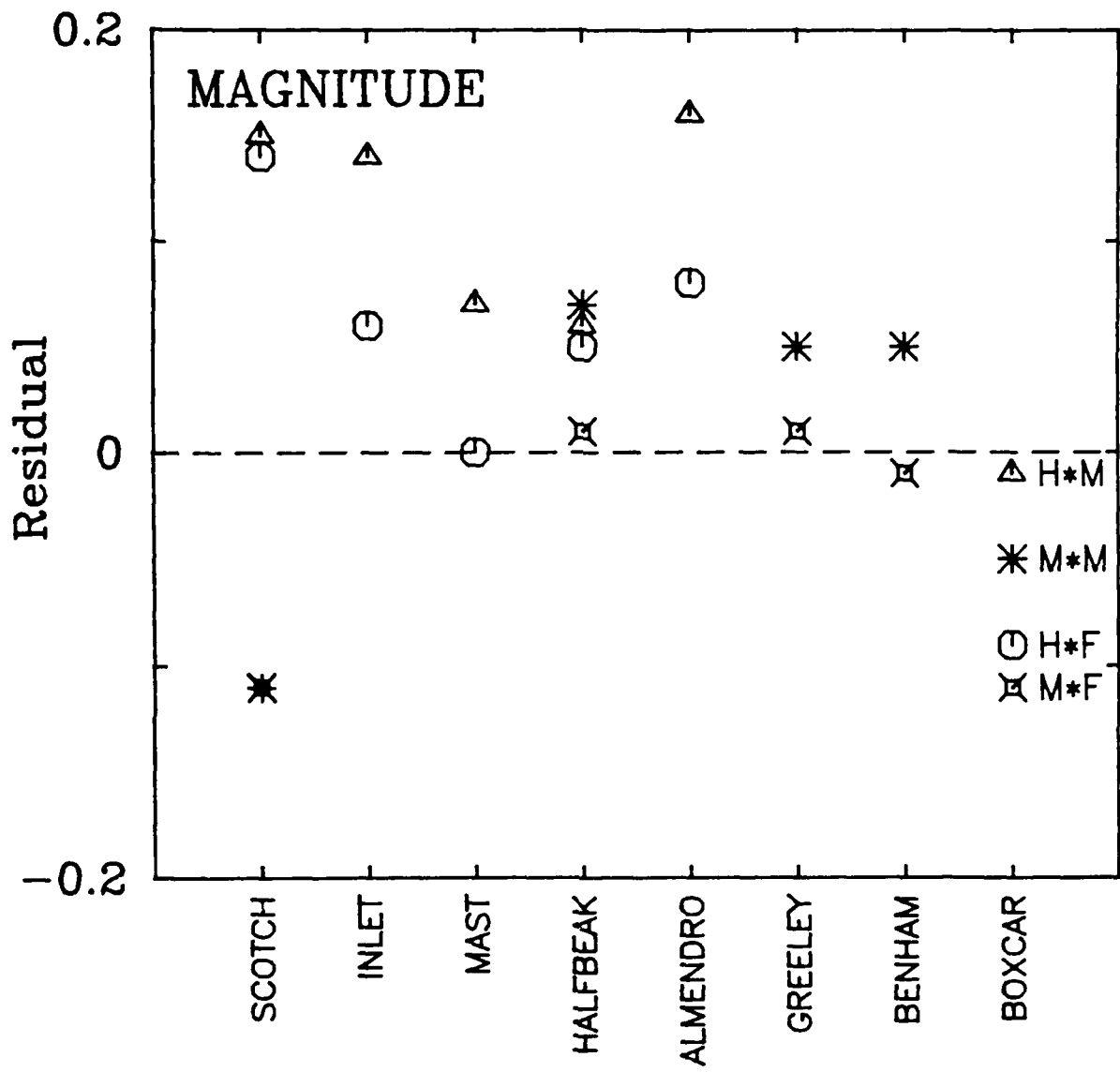


Figure 6. Magnitude residuals for each of the attenuation-source models. The average attenuation models are from log amplitude observations and are given in Table 2.

This type of analysis gives us an indication of the deviation between the observed amplitude measurements and the predicted values based on the true yield and the average attenuation models. The residuals for each source-attenuation model are generally much less than the standard deviations of the observed amplitude measurements given in Table 1. The root mean square of the residuals for the log amplitude residuals are 0.04 (M*F), 0.05 (M*M), 0.07 (H*F), and 0.06 (H*M). In these acronyms for the source-attenuation models, the first letter refers to the source model (H=Helmburger-Hadley, M=Muller-Murphy), the second letter refers to the attenuation model (F=Futterman, M=Minster), and the * refers to a convolution. The RMS residual for the magnitude residuals are 0.07 (M*F), 0.07 (M*M), 0.08 (H*F), and 0.11 (H*M). These are less than the RMS standard deviations of the observed log amplitude measurements (0.10) and magnitude measurements (0.11). Thus the scatter of observed amplitudes and magnitudes about the predictions of our models is less than the scatter in the raw amplitude and magnitude measurements.

The fundamental conclusion of our time-domain amplitude and waveform modeling study is that from WWSSN data either of the two source models and either of the two attenuation models is acceptable. By varying the free parameters in the two attenuation models within reasonable ranges, we can obtain essentially identical predictions of the amplitudes and waveforms. The values of the free parameters which fit the data (Table 2) are significant new results.

Spectral Shape Constraints. The amplitude spectra for the HALFBEAK synthetic seismograms from Figure 4 are shown in Figure 7. The amplitude spectra for the various source-attenuation models are very similar to each

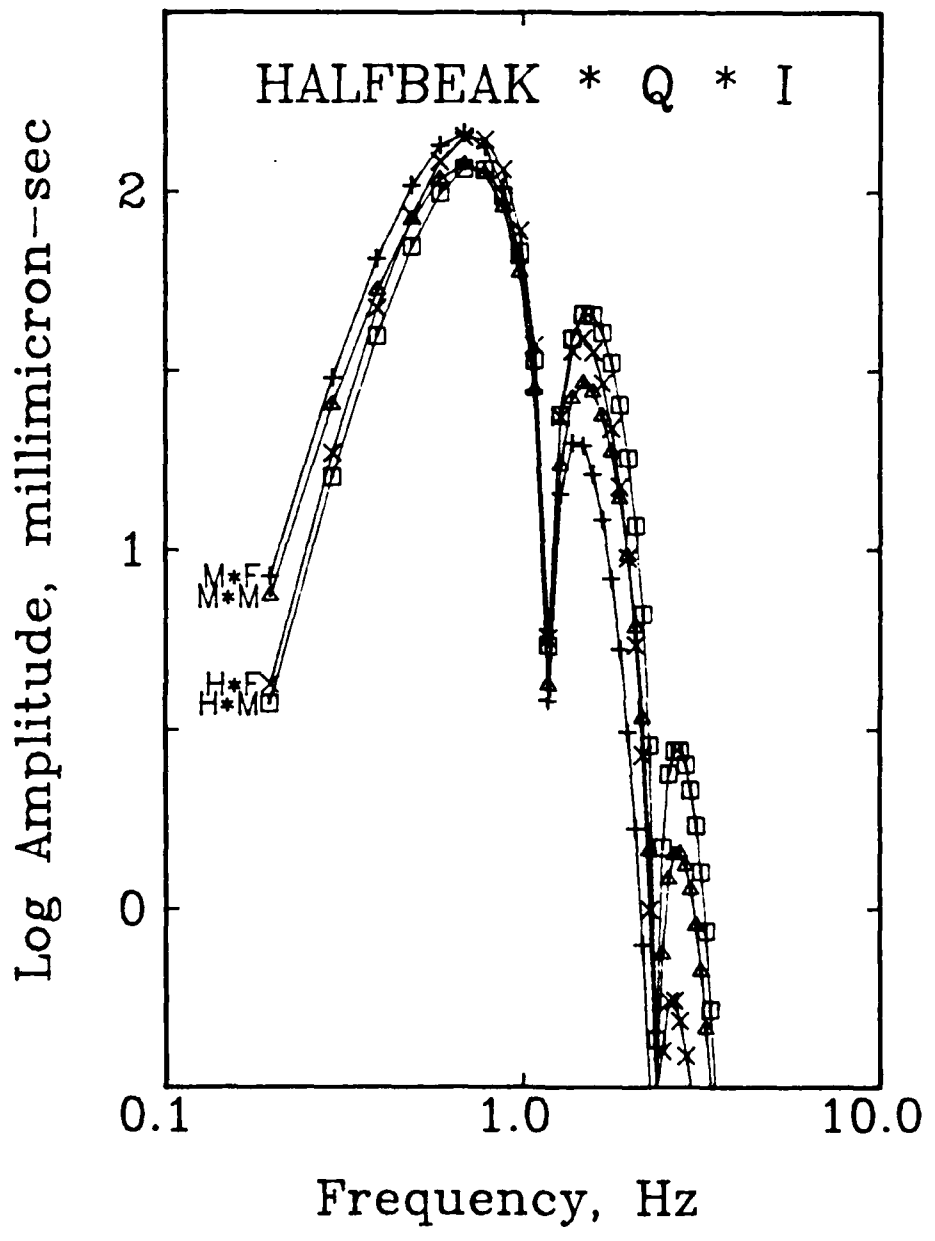


Figure 7. Teleseismic WWSSN short-period displacement spectra for the HALFBEAK synthetic seismograms shown in Figure 4.

other. It would certainly be difficult to distinguish them with band-limited data like that from the WWSSN short-period instrument, even if it were digital. The maximum amplitude of the central peak and its initial falloff rate in the data are apparently well resolved since we obtained almost identical results for all four models. Close inspection of Figure 7 shows that the Helmberger-Hadley synthetic seismograms have a higher relative frequency content than the Mueller-Murphy waveforms in this band. Also, the Minster Q model synthetic seismograms are higher frequency than the Futterman Q model synthetic seismograms. Based on the result that the Minster Q model with $t_o^* = 1.25$ and $\tau_m = 0.051$ for the Mueller-Murphy source model predicts both the amplitude and period of the observed waveforms, we infer that the shape of the observed spectra most closely resemble the corresponding spectrum. However, when considering the amount of scatter in the amplitude observations, the scatter in the attenuation measurements, and the similarity of the various attenuation-source models; we feel that each of the four models is acceptable.

To ultimately select the best attenuation model, we must consider broadband spectral observations (e.g. Der et al., 1985; Bache et al., 1986). Der et al. (1985) computed synthetic spectral templates and compared them to observed body wave spectra of Pahute Mesa events to find the attenuation model that best matched the spectral shape. They assumed the von Seggern-Blandford (1972) granite source model. Although many similar studies (e.g. Der et al., 1982a; Der and Lees, 1985) indicate that a frequency dependent attenuation model is in general necessary, Der et al. (1985) found that the spectral shape in the 0.5-4 Hz band can be just as easily fit with a frequency independent Q model. They obtain apparent t^* values in the 0.4-0.5 sec range. In general, the apparent value of t^* appears to be a stable parameter and differs only

slightly from the absolute value of t^* (Der et al., 1985). However, for the frequency independent Q model, the apparent value of t^* is equivalent to the absolute value of t^* . We therefore assume that a frequency independent t^* of 0.45 sec matches the spectral shape in the 0.5-4 Hz band and apply it as a constraint to our time-domain amplitude models.

Bache et al. (1986) corrected their Pahute Mesa spectral data for the Mueller-Murphy source spectrum and then solved for the attenuation operator directly. They find two frequency dependent attenuation models that match the spectral shape data in the 0.5 to 6 Hz band. One is a Minster Q model (single absorption band) with $t_o^*=1.0$ sec and $\tau_m=0.04$ (designated by QN2). The other is a Minster Q model with $t_o^*=1.2$ sec and $\tau_m=0.06$ convolved with a Futterman Q model with $t^*=0.1$ sec (designated by QN1). In either study, the goal was to find the attenuation model which best explained the spectral falloff over a broad range of frequencies. As we show, the spectral shapes of Pahute Mesa events measured in the two studies are essentially the same. However, the absolute spectral level is quite different.

The left portion of Figure 8 shows the spectral shapes of the source models (for HALFBEAK as an example) convolved with the attenuation models presented in this study. The spectra have been multiplied by frequency squared. The four source-attenuation models described in this paper necessarily have the correct spectral amplitude at around 1 Hz since they are based on matching the time-domain amplitudes on the WWSSN short-period instrument. Shown as dotted curves are models which fit the spectral shape in this band from Der et al. (1985) and Bache et al. (1986). The curve from Der et al. (1985) is a von Seggern-Blandford granite source with a frequency independent t^* of 0.45 sec. The curve from Bache et al. (1986) is a Mueller-Murphy source with the attenuation model QN1. All models are plotted

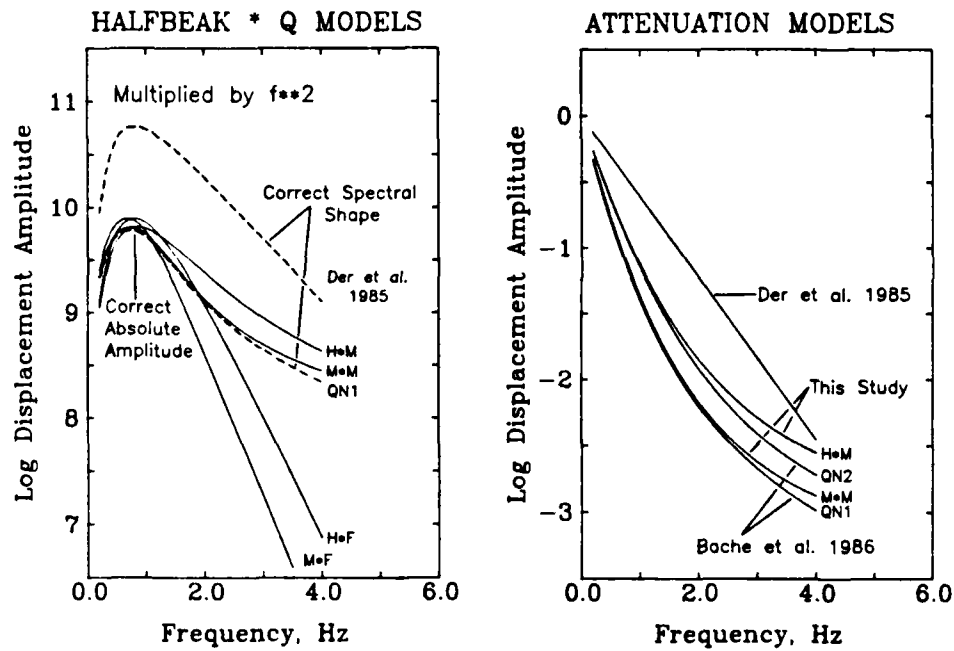


Figure 8. Left side: Comparison of the amplitude spectrum of HALFBEAK source model convolved with the attenuation model of the 4 source-attenuation models presented in this paper with the results of Der et al. (1985) and of Bache et al. (1986). Right side: Comparison of the attenuation model spectrum of the results of this study (only Minster Q models) with the results of Der et al. (1985) and of Bache et al. (1986).

at their true absolute levels. We find that the results of Der et al. (1985) and Bache et al. (1986) have similar spectral shapes, but have different absolute levels. If we use the spectral shape data as a constraint for our source-attenuation models, we find that either source model convolved with the appropriate Minster Q model satisfies the spectral shape as well as the amplitude data. The slope of the source-attenuation models between 1 and 4 Hz as determined from linear regressions are similar for the four models; 0.47 for QN1, 0.56 for Der et al (1985), 0.44 for M*M, and 0.41 for H*M. Each of these fits have regression coefficients exceeding 0.98. The differences in slope is partially due to differences in the source spectral slope of the von Seggern-Blandford, Mueller-Murphy, and Helmberger-Hadley source models.

The right portion of Figure 8 shows the attenuation model spectrum for the results of this study (only the Minster Q models) compared with the results of Der et al. (1985) and of Bache et al. (1986). Each of the five models presented here have similar shapes over the 0.5 to 4 Hz band, thus each model is considered to satisfy the spectral shape data. It is surprising that the attenuation models of this study and of Bache et al. (1986) are so similar considering that the data analyzed was in such different forms. This is somewhat fortuitous since our amplitude observations provide no resolution at higher frequencies. However, the inclusion of the spectral shape data as a constraint to our analysis confirms that our determination of the frequency dependence of Q is correct. Because of the different approaches taken, it is convincing that these attenuation models are appropriate for average Pahute Mesa observations in this band.

YIELD ESTIMATION

If we can assume that the average attenuation models given here are accurate and that the observed log amplitudes are accurate, we can estimate the yield of this set of explosions. The yields for the eight events were estimated from each of the four source-attenuation models from the log amplitude data and are given in Table 3. To estimate the yield using the Helmberger-Hadley source model requires that we define yield scaling relations for values of K and Ψ_∞ . These were based on theoretical and empirical results outlined by Barker et al. (1985). These are

$$(2) K = C_1 Y^{-7/36}, \text{ and}$$

$$(3) \Psi_\infty = C_2 Y^{0.91},$$

where Y is yield and C_1 and C_2 are constants. The constants are obtained by substituting the announced yield and near-field values for BOXCAR into Equations (2) and (3). Hence, C_1 is 26.21 and C_2 is 1.76×10^8 .

The log yield residuals (estimated minus announced) for the five events with announced yields are given in Figure 9. Combining the log amplitude residuals shown in Figure 5 with the log yield residuals in Figure 9, we can estimate the relation between the error in estimated yield and the error in observed amplitude. For the Mueller-Murphy source model with the Minster attenuation model,

$$(4) \Delta \log Y = -1.3 \Delta \log A.$$

Table 3

YIELD ESTIMATES (Kt) FROM THE OBSERVED LOG AMPLITUDES

Event	Announced Yield	M-M Futterman	M-M Minster	H-H Futterman	H-H Minster	Source Model Q Model
ALMENDRO		769	778	655	670	
BENHAM	1150	1158	1218	973	1013	
BOXCAR	1300	1068	1100	891	922	
GREELEY	870	910	929	767	789	
HALFBEAK	365	436	452	403	407	
INLET		352	349	325	324	
MAST		445	449	404	406	
SCOTCH	155	141	134	143	139	

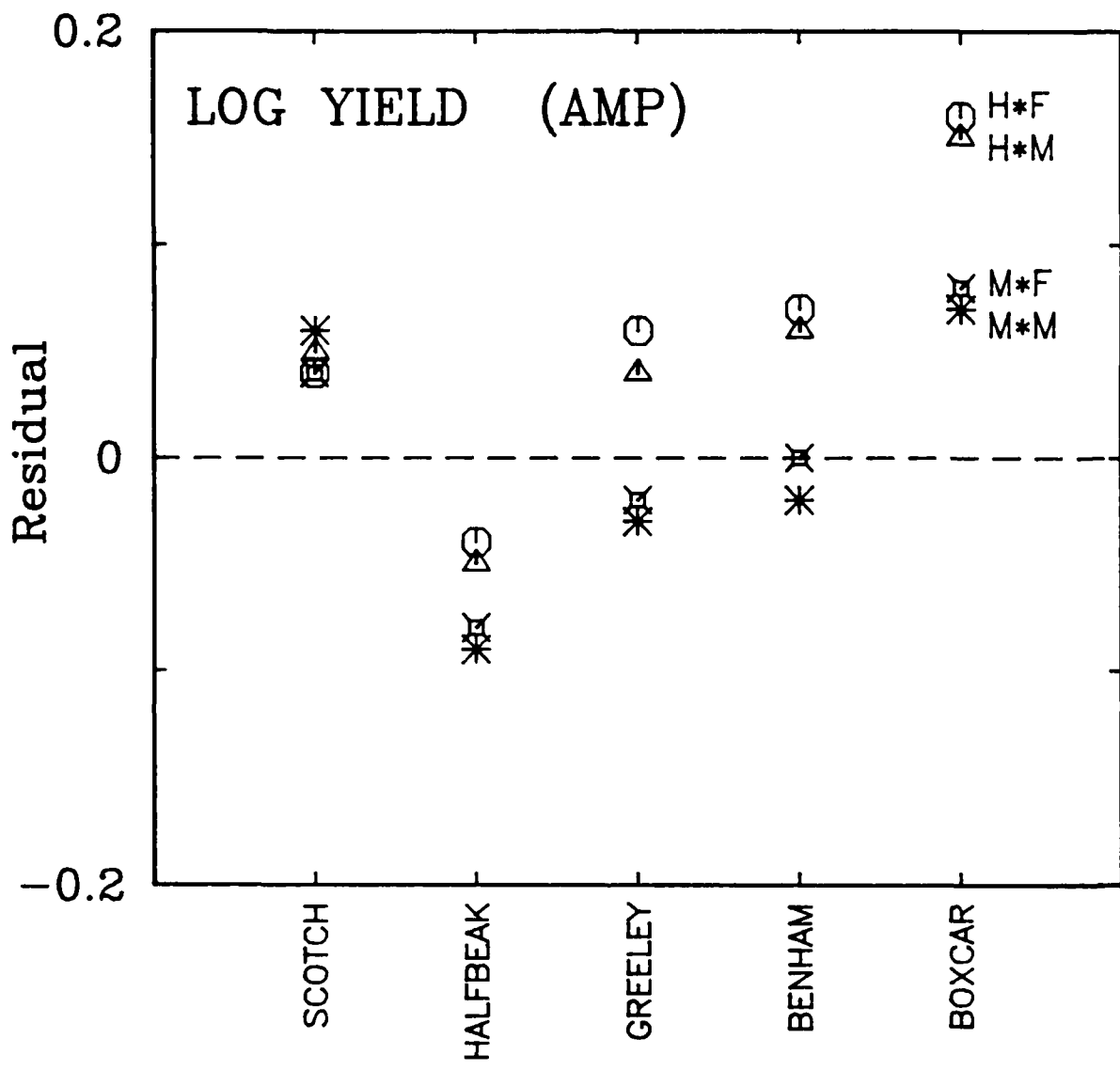


Figure 9. Log yield residuals for the five events with announced yields for each of the source-attenuation models. The log yield residuals are the announced subtracted from the predicted.

With the exception of SCOTCH, the yield residuals tend to become more positive with increasing yield for each of the source-attenuation models. However, these residuals are quite small and may be insignificant considering the amount of scatter in the observations and the attenuation measurements.

Using the estimated yields from Table 3, we computed the predicted source spectra for these events. Figure 10 shows the comparison between the estimated source spectra using the Minster Q model with the Mueller-Murphy source and the predicted source spectra from the announced yield. The difference between the announced and the estimated spectra are shown to be minimal. It would certainly be difficult to distinguish between the predicted and estimated source spectra from observations. For the other source-attenuation models, the differences between the predicted and estimated source spectra are on the same level as those in Figure 10.

DISCUSSION

There has been much recent discussion as to the value of t^* at shorter-periods. The typical value of $t^* = 1.0$ sec at long periods results in extremely large attenuation at higher frequencies for teleseismic observations. Der *et al.* (1982a) state that 4 Hz amplitudes would be reduced by four orders of magnitude relative to 1 Hz amplitudes as the result of this t^* value. The results presented in the left portion of Figure 8 illustrate this effect. However, numerous investigations show that there are substantial amounts of 4-10 Hz energy, far greater than predicted by a t^* of 1 sec. Because of this observation, t^* is thought to be much smaller at higher frequencies.

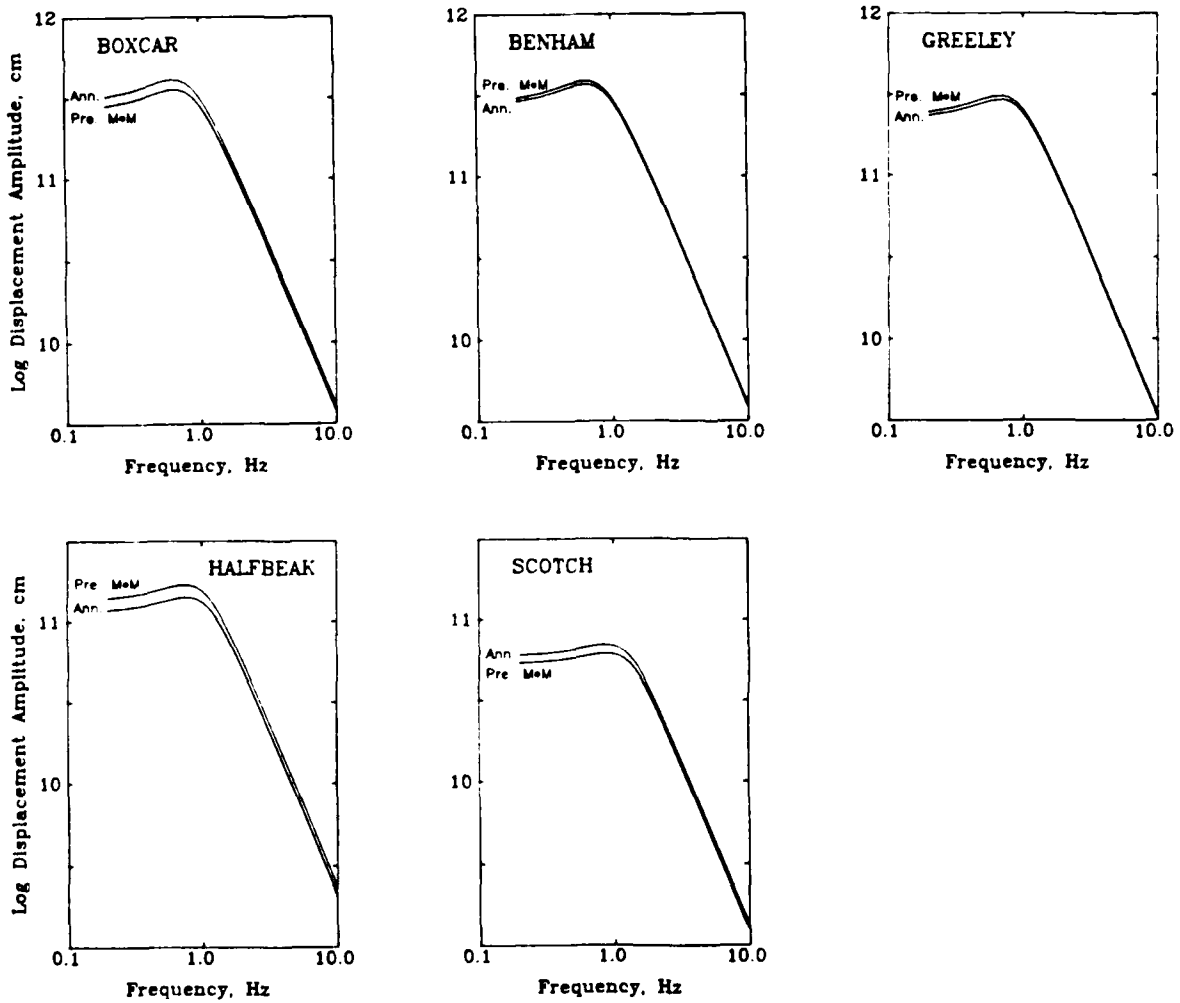


Figure 10. Comparison of the announced yield and predicted yield source displacement spectra for the Mueller-Murphy source model (assuming the Minster Q model results).

Using the preferred source-attenuation models presented in Figure 9, we can compute the value of t^* as a function of frequency. These results are presented in Figure 11. Shown are the values of t^* for the 4 source-attenuation models presented in this study, along with the results of Bache *et al.* (1986) and Der and Lees (1985). The Futterman Q models from this study (M^*F and H^*F) are only considered appropriate near 1 Hz. The attenuation models M^*M , H^*M , $QN1$, and $QN2$ are considered to match both the amplitude and spectral shape data over this band. We see from this that the value of t^* around 1 Hz is between 0.8 and 1.0 sec, depending on the choice of source-attenuation model. Der and Lees (1985) proposed a frequency dependent attenuation model for the western United States that satisfied spectral shape data and time-domain waveform constraints. The events they studied were deep earthquakes, so the data was not subject to upper mantle attenuation on the source side of the raypath. Their preferred model (QP S-T) is shown for comparison in Figure 11. (S-T refers to shield-to-tectonic paths.) Although Der and Lees (1985) argue that previous work (e.g. Der *et al.*, 1982b) demonstrate that the apparent t^* from deep earthquakes is similar to that obtained from shallow events in shield regions, it is reasonable to expect that the QP S-T curve represents a lower bound. If we were to assume some t^* contribution from the source side of the raypath, then the QP S-T curve would become consistent with the other attenuation models.

t^* values in the range of 0.8-1.0 sec near 1 Hz are quite consistent with other estimates of t^* . Burdick *et al.* (1984) obtain a value of 0.9 sec from an analogous near-field to far-field amplitude comparison from Amchitka nuclear explosions. Burdick (1978) conducted a source canceling experiment comparing sP with sS phases and obtained a value of $t^* = 1.3$ sec at about 0.5 Hz for an event in Southern California (presumably similar to NTS). This value

ATTENUATION MODELS

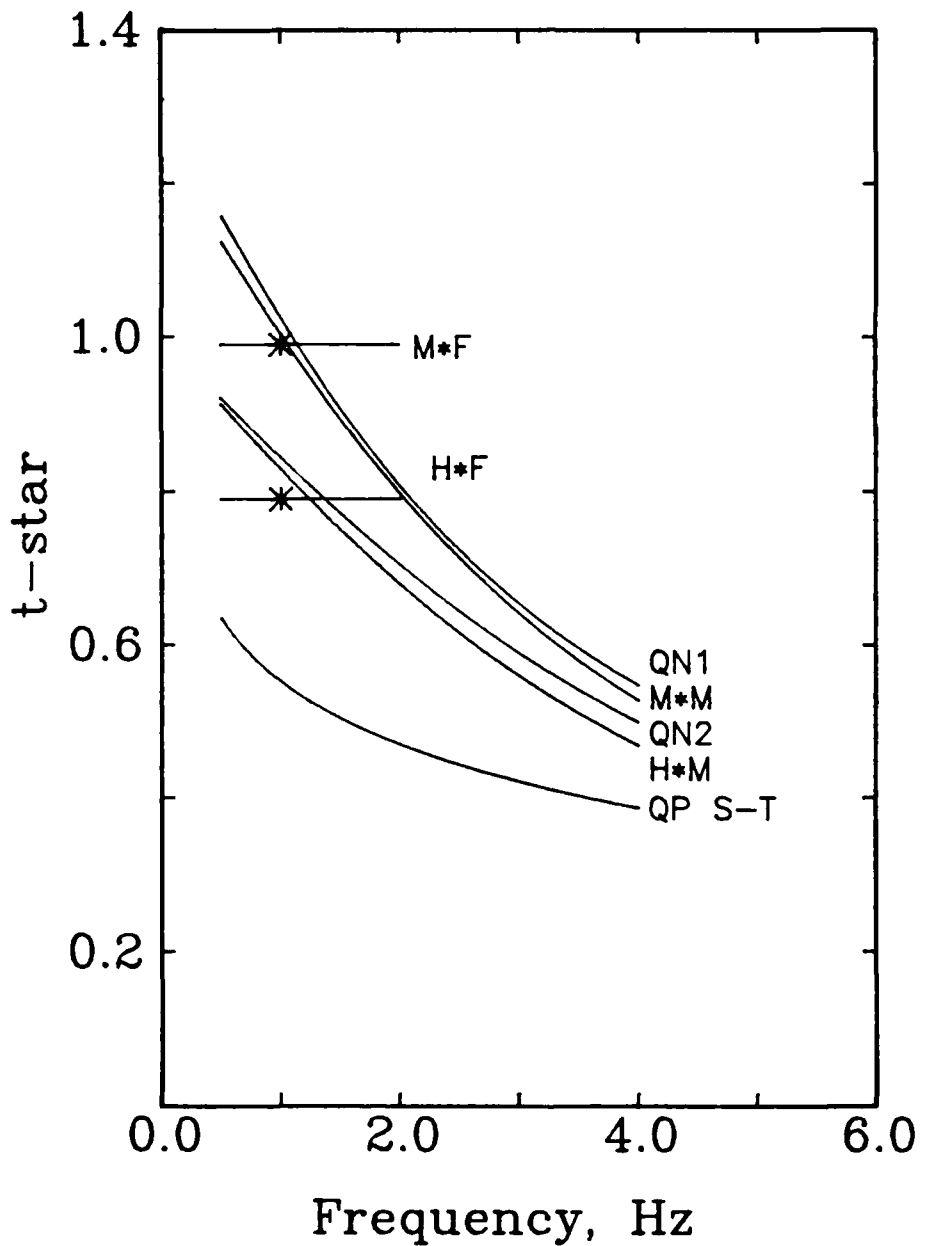


Figure 11. Comparison of the value of t^* as a function of frequency for the four source-attenuation models from this paper and the two attenuation models from Bache et al. (1986). Also shown is the QP S-T attenuation model for the western United States from Der and Lees (1985).

is consistent with the M*M and QN1 models. Burdick (1985) estimated a global average t^* of about 1 sec near 1 Hz from a comparison of ScP and ScS phases. Finally, Burdick and Grand (1985) obtain $t^*=0.99$ sec at around 1 Hz from the comparison of sP and sS waves from Asia.

To illustrate the effect of the absolute value of t^* on the observed amplitudes, we computed synthetic seismograms for the Mueller-Murphy source model with various Q models with similar spectral shapes in the 0.5-4 Hz band. We assumed the M*M source-attenuation model (this paper), along with $t_o^*=0.75$ sec and $\tau_m=0.025$, and a frequency independent $t^*=0.42$ sec (similar to Der et al., 1985). Each of these Q models have the same spectral slope (0.57) in the 0.5-4 Hz band (linear regression coefficients exceed 0.97). The results for the HALFBEAK event are presented in Figure 12. The predicted amplitude using $t^*=0.42$ sec is nearly a factor of 5 larger than observed, while the predicted amplitude for $t_o^*=1.25$ and $\tau_m=0.051$ is similar to the observed value. Furthermore, the synthetic seismogram with $t^*=0.42$ sec is too high in relative frequency content compared to representative observations (shown at the right in Figure 3). This example illustrates that the use of spectral shape data without absolute amplitude information can lead to incorrect Q models. We have previously shown that the use of absolute amplitude information without spectral shape data can also lead to incorrect results. For example, the M*M and M*F models have the same absolute amplitude level near 1 Hz, but the spectral slopes in the 0.5-4 Hz band are very different. It is thus necessary to use both absolute amplitude information and spectral shape or decay information to obtain reliable attenuation models.

A direct application of our results is that we are able to predict the relation between yield and magnitude based upon the appropriate attenuation models for a given site. We do so here assuming the Mueller-Murphy source and

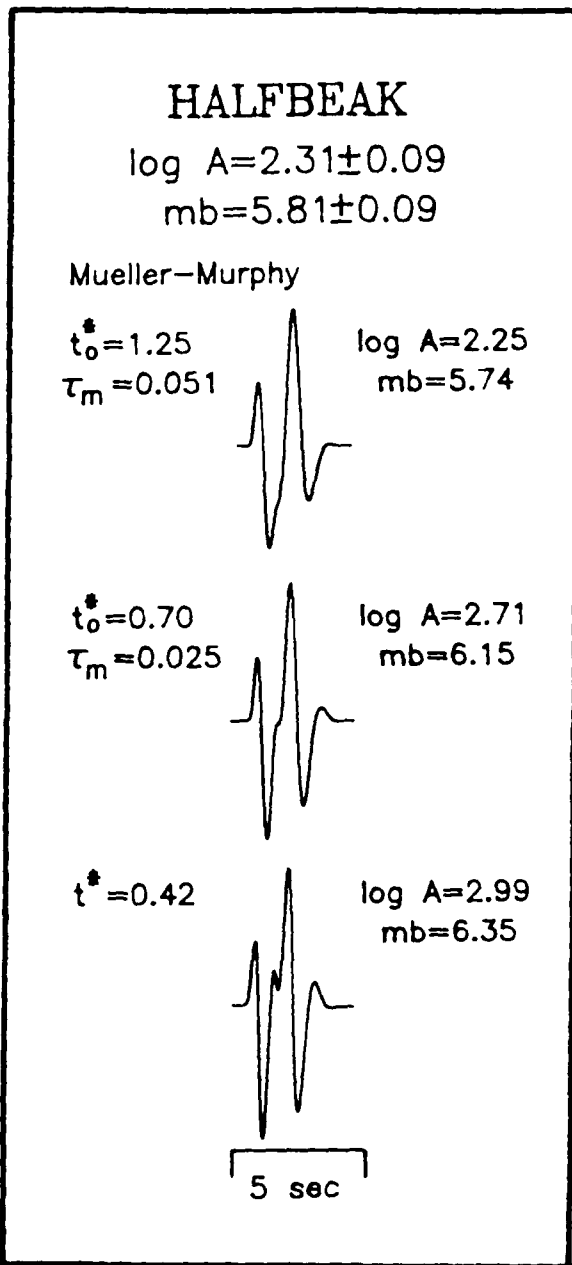


Figure 12. Teleseismic WWSSN short-period synthetic seismograms for HALFBEAK. Shown are the synthetic waveforms for the Mueller-Murphy source model with the Minster attenuation model presented in this paper compared to other attenuation models with similar spectral slopes but with different absolute levels.

the Minster Q model (M*M). Synthetic seismograms were computed as in the above analysis for yields ranging from 50 to 1300 Kt. The pP delay times were determined from the average pP delay - depth relation determined from the results of Lay (1985) and assuming the predicted depth - yield dependence from Mueller and Murphy (1971). The predicted magnitudes are given in Figure 13. The linear relation (with regression coefficient of 1) is given by

$$(5) m_b = 3.695 + 0.8019 \log Y.$$

For the predicted amplitudes, the relation is given by

$$(6) \log A = 0.3862 + 0.7252 \log Y.$$

The difference in slopes in Equations 5 and 6 is due to the period correction included in the magnitude calculation. Equation 5 is almost identical to that obtained by Lay (1985) from a regression of observed magnitudes for the five events with announced yields. The observed magnitudes are also given in Figure 13 and are in good agreement with the predicted m_b -yield relation.

We have not yet addressed the possibility of constraining the source models with longer-period observations. As apparent in Figure 1, very precise constraints on 10 sec spectral levels could serve to discriminate between the source models. However, the long-period levels for the Helmberger-Hadley source could be increased simply by decreasing the overshoot parameter B, which was arbitrarily set to 1 in the near-field modeling. The near-field waveforms are essentially unaffected if the value of B is set to 0.5, which gives Ψ_∞ a factor of 1.7 larger. Smaller values of B will increase Ψ_∞ further, but will begin to affect the spectrum in the near-field band (1-5

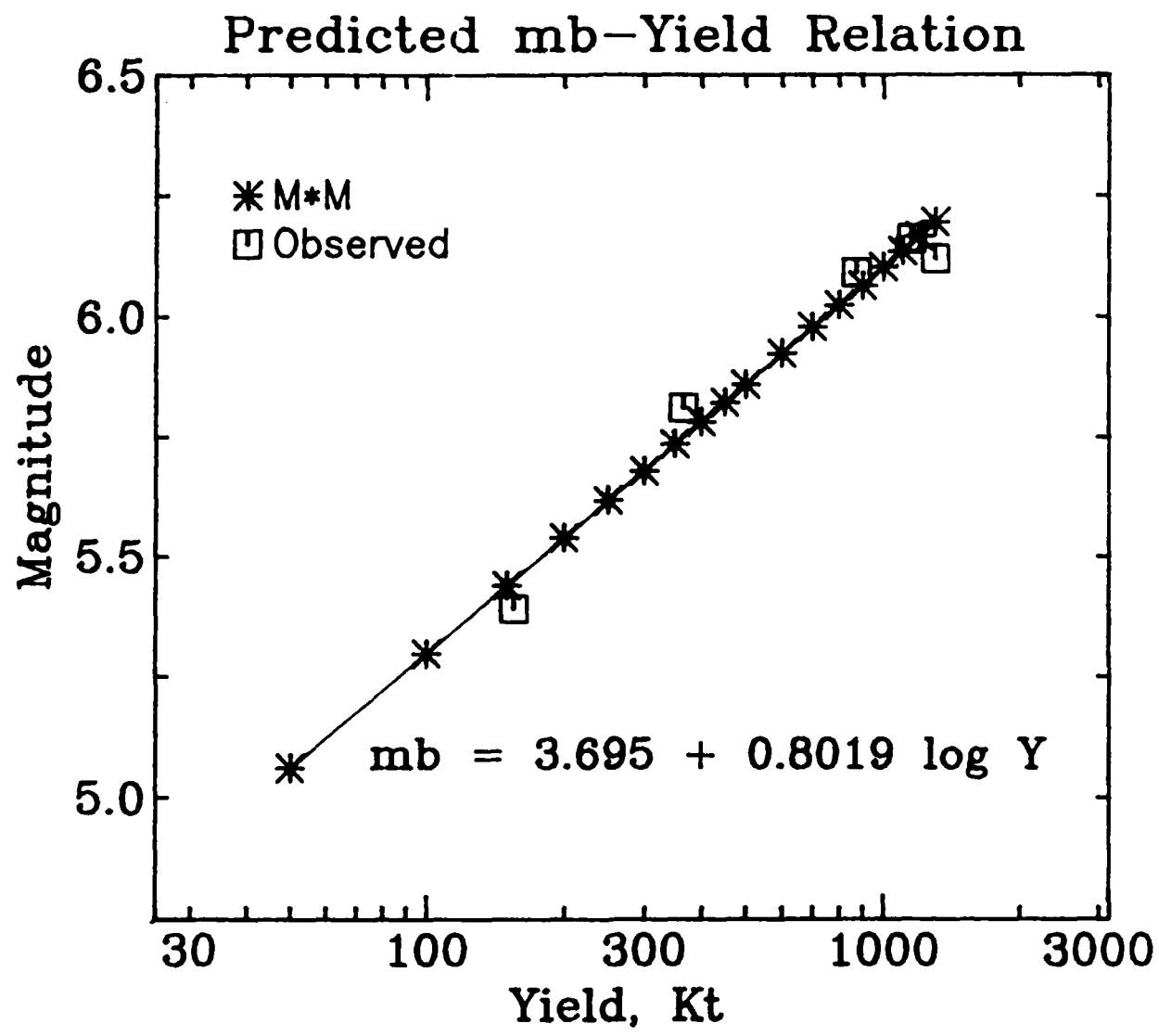


Figure 13. The predicted m_b -yield relation for WWSSN short-period determinations for the Mueller-Murphy source and Minster Q model. Shown are the observed magnitudes for the five events with announced yields.

Hz), and thus change the waveform matches. For now we will limit our discussion to $B > 0.5$, but acknowledge the possibility of even smaller values of B . Setting the value of B at 0.5 will increase the WWSSN short-period (0.5-2 Hz) amplitudes by less than 10%, thus our high frequency attenuation operator modeling will be relatively unchanged by any long-period modifications.

Several studies have obtained estimates of long-period source spectral levels for Pahute Mesa tests from analysis of surface waves (Stevens, 1985; Given and Mellman, 1985). These estimates are compared with the predictions of the Mueller-Murphy source model, as well as the near-field modeling results of Barker et al. (1985) with $B=1.0$ in Table 4. On average, the surface wave results are consistent with the Mueller-Murphy source predictions, but are a factor of 3-4 larger than the Helmberger-Hadley source predictions. Allowing for a factor of 1.7 increase in Ψ_∞ by decreasing B in the near-field models still leaves a factor of about 2 discrepancy between the surface wave estimates and the results of Barker et al. (1985). While this favors the Mueller-Murphy source model, further work is needed to establish the confidence levels on the various estimates before a definitive conclusion can be drawn.

Table 4

ESTIMATED EXPLOSION SOURCE STRENGTH Ψ_∞ ($\times 10^{10}$ cm³)

Event	Given and Mellman, 1985	Stevens, 1986	M-M * Ann. Yield	H-H (B=1) * Barker et al., 1985
ALMENDRO	17.8	19.0	(20.0)	5.7
BENHAM	--	--	26.9	(9.6)
BOXCAR	--	--	29.5	12.0
GREELEY	--	--	21.7	(7.6)
HALFBEAK	--	--	11.2	3.8
INLET	--	--	(10.9)	3.2
MAST	15.5	12.0	(13.2)	4.7
SCOTCH	8.9	9.1	5.9	1.3

* The numbers in parentheses () are estimated from the predicted yields assuming the Minster Q models.

CONCLUSIONS

Attenuation models for short-period P waves from Pahute Mesa nuclear explosions have been developed by time-domain modeling of teleseismic waveforms. Trade-offs between source and attenuation models were explored using two explosion source representations and two attenuation models, one of which includes frequency dependence. For the Mueller-Murphy source model, which has an asymptotic high frequency spectral falloff of f^{-2} , yield scaling is used to determine the source models. This source leads to frequency independent t^* values of about 1.0 sec, or frequency dependent absorption band models with $t_0^*=1.25$ sec and τ_m (high frequency roll off) of about 0.05. The Helmberger-Hadley source, which has a high frequency spectral decay of f^{-3} , is constrained by near-field waveform modeling. This source results in frequency independent models with t^* values of about 0.8 sec, or frequency dependent models with $t_0^*=1.0$ sec and τ_m of about 0.04. Spectral shape information from higher frequency data is well matched by the absorption band attenuation models for either source representation. We find that the use of both spectral shape data and absolute amplitude information is necessary to determine reliable attenuation models. Simple correction of observed spectra by assuming the high-frequency asymptotic spectral decay rates of these source models in the short-period band can lead to erroneous conclusions regarding the attenuation operator. The two source models are sufficiently similar in the 0.5-4 Hz band that it is not possible to select the most appropriate model. Long-period measurements tend to favor the higher long-period spectral amplitudes predicted by the Mueller-Murphy source model. Average attenuation models for each source model can be used to accurately predict the yields for other events.

REFERENCES

- Anderson, D.L., and J.W. Given (1982). Absorption band Q model for the Earth, J. Geophys. Res., 87, 3893-3904.
- Bache, T.C., P.D. Marshall, and L.B. Bache (1985). Q for teleseismic P waves from Central Asia, J. Geophys. Res., 90, 3575-3587.
- Bache, T.C., S.R. Bratt, and L.B. Bache (1986). P-wave attenuation, m_b bias and the threshold test ban treaty, Final Technical Report SAIC-86/1647, Science Applications International Corporation, San Diego, California.
- Barker, J.S., S.H. Hartzell, L.J. Burdick, and D.V. Helmberger (1985). Determination of effective source functions and measurement of seismic yields from underground nuclear explosions at Pahute Mesa by modeling near-field records, Final Technical Report WCCP-R-85-02, Pasadena, California.
- Burdick, L.J. (1978). t^* for S waves with a continental raypath, Bull. Seism. Soc. Am., 68, 1013-1030.
- Burdick, L.J. (1985). Estimation of the frequency dependence of Q from ScP and ScS phases, Geophys. J., 80, 35-55.
- Burdick, L.J., T. Wallace, and T. Lay (1984). Modelling the near field and teleseismic observations from the Amchitka test site, J. Geophys. Res., 89, 4373-4388.
- Burdick, L.J., and S.P. Grand (1985). Estimation of t^* for Asian travel paths using SP and SS phases, The VELA Program : A twenty-five year Review of Basic Research, DARPA, 677-692.
- Cormier, V.F. (1982). The effect of attenuation on seismic body waves, Bull. Seism. Soc. Am., 72, S169-S200.
- Der, Z.A., T.W. McElfresh, and A. O'Donnell (1982a). An investigation of the regional dependence of anelastic attenuation in the mantle under the United States in the 0.5-4 Hz band, Geophys. J., 69, 67-99.
- Der, Z.A., W.D. Rivers, T.W. McElfresh, A. O'Donnell, P.J. Klouda, and M.E. Marshall (1982b). Worldwide variations in the attenuative properties of the upper mantle as determined from spectral studies of short-period body waves, Phys. Earth planet. Int., 30, 12-25.
- Der, Z.A., and A.C. Lees (1985). Methodologies for estimating $t^*(f)$ from short-period body waves and regional variations of $t^*(f)$ in the United States, Geophys. J., 82, 125-140.
- Der, Z.A., T. McElfresh, R. Wagner, and J. Burnett (1985). Spectral characteristics of P waves from Nuclear explosions and yield estimation, Bull. Seism. Soc. Am., 75, 379-390.

Frasier, C.W., and J.J. Filson (1972). A direct measurement of the Earth's short-period attenuation along a teleseismic raypath, J. Geophys. Res., 77, 3782-3787.

Futterman, W.I. (1962). Dispersive body waves, J. Geophys. Res., 67, 5279-5291.

Given, J.W., and G.R. Mellman (1985). Source parameters for nuclear explosions at NTS and Shagan River from observations of Rayleigh and Love waves, Proceedings of the 7th annual DARPA/AFGL seismic research symposium, May 6-8, 1985 at the U.S. Air Force Academy, Colorado Springs, Colorado.

Hartzell, S.H., L.J. Burdick, and T. Lay (1983). Effective source functions for Pahute Mesa nuclear tests, Final Technical Report WCCP-R-83-3, Woodward-Clyde Consultants, Pasadena, California.

Haskell, N.A. (1967). Analytic approximation for the elastic radiation from a contained underground explosion, J. Geophys. Res., 72, 2583-2587.

Helmburger, D.V., and D.M. Hadley (1981). Seismic source functions and attenuation from local and teleseismic observations of the NTS events JORUM and HANDLEY, Bull. Seism. Soc. Am., 71, 51-67.

Jordan, T.H., and S.A. Sipkin (1977). Estimation of the attenuation operator for multiple ScS waves, Geophys. Res. Lett., 4, 167-170.

Lay, T. (1985). Estimating explosion yield by analytical waveform comparison, Geophys. J., 82, 1-30.

Minster, J.B. (1978a). Transient and impulse responses of a one dimensional linearly attenuating medium; part I. Analytical results, Geophys. J., 52, 479-501.

Minster, J.B. (1978b). Transient and impulse responses of a one dimensional linearly attenuating medium; part II. A parametric study, Geophys. J., 52, 503-524.

Mueller, R.A., and J.R. Murphy (1971). Seismic characteristics of underground nuclear detonations. Part I. Seismic spectrum scaling, Bull. Seism. Soc. Am., 61, 16775-1692

Murphy, J.R. (1977). Seismic source functions and magnitude determinations for underground nuclear detonations, Bull. Seism. Soc. Am., 67, 135-158.

Shore, M.J. (1983). Mantle Q_s from body waves - difficulties in determining frequency dependence, EOS, Trans. Am. geophys. Un., 61, 298.

Sipkin, S.A., and T.H. Jordan (1979). Frequency dependence of Q_{ScS} , Bull. Seism. Soc. Am., 69, 1055-1079.

Sipkin, S.A., and T.H. Jordan (1980). Regional variation of Ω_{ScS} , Bull. Seism. Soc. Am., 70, 1071-1102.

Stevens, J.L. (1986). Estimation of scalar moments from explosion-generated surface waves, Bull. Seism. Soc. Am., 76, 123-151.

Veith, K.F., and Clawson, G.E. (1972). Magnitudes from short period P wave data, Bull. Seism. Soc. Am., 62, 581-594.

von Seggern, D., and R. Blandford (1972). Source time functions and spectra for underground nuclear explosions, Geophys. J., 31, 83-97.



2 - 86

